THE UNIVERSITY OF PARMA

DEPARTMENT OF CHEMISTRY, LIFE SCIENCES
AND ENVIRONMENTAL SUSTAINABILITY

PhD in Science and Technology of Materials

XXIX cycle

DYES AND NANOPARTICLES FOR BIOIMAGING: LINEAR PHOTOPHYSICAL AND NONLINEAR OPTICAL STUDY

Course coordinator:

Professor Enrico Dalcanale

Scientific supervisors:

Professor Anna Painelli

Professor Mykhailo V. Bondar

PhD student:

Siarhei Kurhuzenkau

2014-2017

To Ira and Maksim

«… no one ought to ask *why this instead of that*?
Instead, everyone ought to ask *how does it work*?»

R. Sheckley. Dimension of Miracles.

ACKNOWLEDGEMENTS

I appreciate this opportunity to express deepest gratitude to my supervisors – Prof. Anna Painelli (University of Parma) and Prof. Mykhailo V. Bondar (Institute of Physics of National Academy of Sciences of Ukraine). I had a unique chance to learn from their experience and I am grateful for the encouragement, optimism and unending support they gave me in these years.

I wish to acknowledge the contribution of my collaborators. I thank Dr. Nora Ventosa, Prof. Jaume Veciana and Antonio Ardizzone (ICMAB, Barcelona) for the work on quatsomes. Many thanks to Antonio for his restless efforts on synthesis (sei davvero un ragazzo in gamba!) and for inspiring and fruitful discussions. I would like to thank Prof. David Hagan and Prof. Eric W. Van Stryland (UCF, Orlando) for providing access to the state-of-the-art femtosecond laser systems. Many thanks to all members of CREOL NLO group, especially to Paul (Peng) Zhao and to Trenton Ensley for answering my numerous questions and tutoring in the lab. Their help and advice is invaluable. I thank Prof. Kevin Belfield (UCF and NJIT, Newark) and Dr. Sheng Yao (UCF) for providing me with fluorene derivatives, Dr. Adam Woodward (UCF) for performing Z-scan measurements. The work on bioimaging is due to the collaboration with the group of Prof. Kevin Belfield and the group of Dr. Lorenzo Albertazzi (IBEC, Barcelona).

I wish to thank the members of our group at UNIPR: Dr. Cristina Sissa, Prof. Francesca Terenziani, Prof. Alberto Girlando and Dr. Matteo Masino for tutoring and help in the lab. I am grateful to Dr. Cristina Sissa not only for scientific inputs, but also for her help with documents and dealing with various administrative procedures. My relocation to Italy would not be possible

otherwise. I also thank Paola Rossi for assistance with documents and administrative support.

Many thanks to my labmates and friends – Domna Nikolaidou, Somananda Sanyal, Nicola Castagnetti, Francesco Di Maiolo, Francesca Delchiaro and Brunella Bardi for their friendship, inspiration and warm working atmosphere. I also thank Sveta Levchenko and Zhenya Shaydyuk for help during my secondment at the Institute of Physics in Kiev.

I am grateful to all members of *Nano2Fun* project for creating highly productive and stimulating environment and for sharing their knowledge. I acknowledge EU commission for financial support through Nano2Fun project. The research leading to these results received funding from the People Programme (Marie Curie Actions) of the European Union's Seventh Framework Programme FP7/2007–2013 under REA grant agreement №607721 (*Nano2Fun*).

I would like to thank the scientists who opened me the door to the field of optics and spectroscopy – Dr. Alexander A. Maskevich, Prof. Siarhei A. Maskevich, Dr. Vitali I. Stsiapura and Prof. Natalia D. Strekal.

Finally, I thank my family for their unconditional support, understanding and infinite patience.

TABLE OF CONTENTS

LIST OF ABBREVIATIONS

1PA	one-photon absorption
2PA	two-photon absorption
2PF	two-photon fluorescence
2PM	two-photon microscopy
2PP	two-photon photopolymerization
ASE	amplified spontaneous emission
Cryo-TEM	cryogenic transmission electron microscopy
CW	continuous-wave
DC	differential image contrast microscopy
DLS	dynamic light scattering
DMEM	Dulbecco's modified eagle's medium
ESA	excited state absorption
ESM	essential-state model
FON	fluorescent organic nanoparticle
FRET	Förster resonance energy transfer
FWHM	full width at half maximum
GM	Goppert-Mayer, the unit of 2PA cross-section
ONP	organic nanoparticle
PDI	polydispersity index
QS	quatsome(s)
STE(D)	stimulated emission (depletion)
STORM	stochastic optical reconstruction microscopy
TCSPC	time-correlated single photon counting
WLC	white-light continuum

BACKGROUND AND MOTIVATION

In the last decades two photophysical processes attracted significant research interest owing to their application potential, particularly in the fields of bioimaging and micro- and nanomachining.[1]-[3] These are two-photon absorption (2PA) and stimulated emission depletion (STED).

2PA is a process of *simultaneous* absorption of two photons, bringing a molecular system from the ground to an excited state. It was theoretically predicted and described in the work of Maria Göeppert-Mayer in 1931,[4] however the first experimental observation came only 30 years later, with the advent of lasers.[5] In this Thesis we discuss a degenerate 2PA, when both absorbed photons have the same wavelength λ. Two-photon absorption is a quadratic process, meaning that the transition rate R of 2PA depends on the square intensity I of the excitation beam:

$$R \sim \delta(\lambda) I^2$$

where $\delta(\lambda)$ is the molecular 2PA cross-section, usually measured in Göppert-Mayer units (1 GM= 10^{-50} $cm^4 \cdot s \cdot photon^{-1}$). Typical values of δ for small organic dyes are in the range of 10-1000 GM,[6] meaning that 2PA is much weaker process compared to one-photon absorption (1PA), and it requires a highly intense light source to be observed. Typically pulsed Ti:Sapphire lasers are used for this purpose, since they can deliver extremely high power densities due to extremely short pulse duration (~100 fs) while keeping average irradiance low.

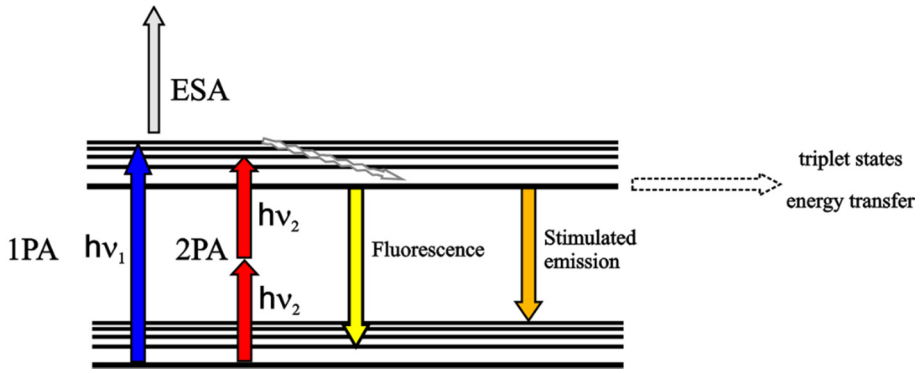

Figure 1. *Jablonski diagram illustrating processes of 1PA, degenerate 2PA, excited state absorption (ESA), fluorescence and stimulated emission.*

The nonlinear nature of 2PA results in the following important properties:

1. The energy of each of photons is far from the transition energy (see Figure 1), meaning that for most 2PA applications red and near-infrared (NIR) laser sources are used. NIR light can penetrate much deeper in the sample, and particularly so for biological samples, and suffers less from scattering losses compared to UV/Vis excitation.
2. The quadratic dependence of 2PA leads to highly localized excitation, occurring typically near the focus of a laser beam. Figure 2 compares 1PA and 2PA. In the case of 1PA the excitation probability linearly depends on the light intensity and the sample is excited along all the path of a laser beam. This leads to the out-of-focus excitation, which is highly undesirable, since it results in high background level and increased photodamage or photoreaction. The volume where two-photon excitation process takes place is instead spatially confined into an elementary unit volume, called *voxel*, being the 3D analogue of the pixel (Figure 2).

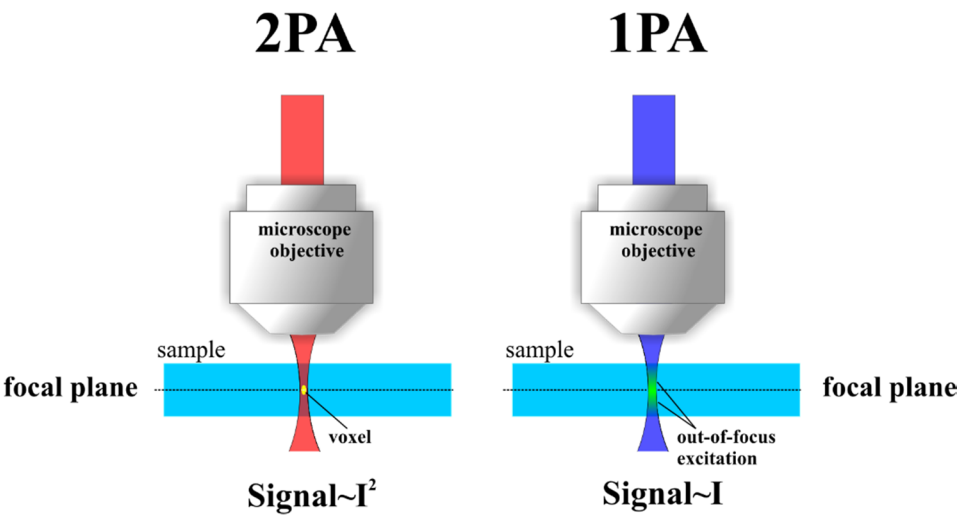

Figure 2. *A scheme comparing one- and two-photon fluorescence excitation.*

Two most important practical applications of 2PA are two-photon polymerization (2PP) and two-photon excitation microscopy (2PM). Owing to the threshold nature of photopolymerization the nonlinear dependence of 2PA allows to control the size of a voxel in 2PP and produce structures with sub-diffraction resolution.[1] As for 2PM, its main advantages are non-invasive nature and deep tissue penetration (up to several millimeters).[2],[3] 2PM is however a diffraction-limited microscopy.

Although the process of stimulated emission has been known for a long time, recently it has gained much attention after the report[7] of S. Hell that proposed the super-resolution microscopy based on fluorescence depletion by stimulated emission. In 2014 S. Hell was awarded a Nobel Prize in chemistry for "the development of super-resolved fluorescence microscopy", together with E. Betzig and W. Moerner. The basic principle of stimulated emission depletion can be illustrated with the Jablonski diagram in Figure 1. When an incident photon interacts with a previously excited fluorophore, it can stimulate the

fluorophore to emit, provided that wavelength of a photon falls in the emission spectrum of the fluorophore. The emitted photon has the same energy and polarization and propagates in the same direction as incident photon. The stimulated emission is therefore not observed with 90 degree detection geometry or in a confocal laser scanning microscope and does not interfere with the detection system. But due to depletion of the excited state, the fluorescence intensity is decreased, and, using depletion beams with a controlled shape, one can reduce the size of the fluorescent spot to a sub-diffraction size.[7] The efficiency of STED process depends on the applied beam intensity and on the molecular stimulated emission (STE) cross-section. In this Thesis we focus attention on fundamental aspects of STED in organic dyes.

The successful application of the fluorescence techniques depends heavily on the properties of applied probe. General requirements for an appropriate probe are:[8]

- High photo- and termostability. In fluorescence experiments probes are often exposed to strong laser beams. The stability of a probe under these conditions is of crucial importance for many practical applications, such as single-molecule detection, laser scanning microscopy, when a sample is repeatedly exposed to intense illuminations or in stochastic optical reconstruction microscopy, requiring large numbers of snapshots of the same cell.
- High brightness (high fluorescence quantum yield and molar extinction coefficient) to enhance the signal-to-noise ratio.
- High Stokes shift, to minimize self-absorption and a cross-talk between excitation and emission
- Appropriate absorption and emission wavelength, to minimize the excitation of the sample autofluorescence and to reduce scattering and absorption in the sample
- Biocompatibility (hydrophilicity and low cytotoxicity)

This list may be complemented with additional requirements of high 2PA cross-section for 2PA applications or high STE cross-sections for STED microscopy. Most materials and probes for imaging applications can be divided into two big groups:[8]

1. molecular chromophores or dyes and fluorescent proteins
2. nano- and microparticles, including organic, inorganic and hybrid nanoparticles, which can be either intrinsically fluorescent (quantum dots, organic dye nanoparticles, carbon-based nanoparticles) or used as carriers of chromophores (e.g silica or polymeric nanoparticles, liposomes)

Despite on continuous progress in the field still there is a strong demand for bright, stable and efficient probes, meeting as much requirements listed above as possible. Organic materials are appealing candidates in this respect, since they offer various strategies for the fine-tuning of various properties, such as the optical response, photostability and solubility, through modification of their structure.[6]

In current work we focus on fundamental studies of linear, nonlinear optical properties and photostability of organic materials, such as dyes and nanoparticles and their application potential as probes for conventional and super-resolution bioimaging.

1 EXPERIMENTAL METHODOLOGY

In this chapter we shortly describe main experimental techniques adopted for the characterization of organic materials that include linear or one-photon absorption (1PA), two-photon absorption (2PA), fluorescence, fluorescence excitation anisotropy, pump-probe and time-resolved stimulated emission depletion (STED) spectroscopies. As for 2PA the two most common techniques, Z-scan and two-photon excited fluorescence (2PF) are outlined. We also describe a method for the quantitative characterization of the photostability of the materials of interest in terms of the molecular photodecomposition quantum yield. Photostability is in fact an important property of organic emitters to be considered for photonics applications.

1.1 Linear absorption and fluorescence

UV/Vis absorption spectroscopy is a basic tool for studying the photophysics of molecular systems. It provides information about transitions, from the ground to optically allowed (bright) excited states $g \rightarrow e$. Specifically, the position of the band gives information on the energy of the transition, while the molecular extinction coefficient ε gives information on the transition dipole moment $\boldsymbol{\mu_{ge}}$ through the equation:

$$\mu_{ge}^2 = \frac{0.09584}{\bar{\nu}_{max}} \int \varepsilon(\bar{\nu}) d\bar{\nu} \qquad (1.1)$$

where the dipole moment is measured in Debye, $\bar{\nu}_{max}$ is the wavenumber (in cm^{-1}) taken in the maximum of the absorption band and ε (in $M^{-1}cm^{-1}$) is the

molar extinction coefficient. The integral in (1.1) is taken over the absorption band formed by a single $g \rightarrow e$ transition. In this work absorption spectra were recorded with Cary 500 (Varian) instrument, located at CREOL, and Lambda 650 (Perkin Elmer) UV/Vis spectrophotometer at UNIPR.

One-photon excited fluorescence and fluorescence excitation spectra were measured with Horiba Jobin Yvon Fluoromax-3 spectrofluorimeter at UNIPR. To minimize self-absorption effects all measurements were run on dilute samples with maximum absorbance $D < 0.1$. All spectra were corrected for the spectral response of the detector, for the wavelength-dependent spectrum of the excitation lamp and for the fluctuations of the intensity of the lamp. Fluorescence decay curves were collected on the same spectrofluorimeter by a time-correlated single photon counting technique (TCSPC) under subnanosecond/nanosecond excitation with 1 MHz repetition rate. Fluorescence lifetimes were estimated by fitting the fluorescence decays curves with mono- or biexponential functions using nonlinear least-squares iterative deconvolution method.[9]

1.1.1 Fluorescence quantum yield measurements

Quantum yield is defined in general as the number of events occurring in a system per absorbed photon. Specifically, the fluorescence quantum yield is defined[9],[10] as the ratio of photons emitted by fluorescence N_{em} to the number of absorbed photons N_{abs}:

$$Q_{FL} = \frac{N_{em}}{N_{abs}} \tag{1.2}$$

The fluorescence quantum yield can also be expressed as a fraction of molecules that de-excite through photon emission:

$$Q_{FL} = \frac{k_r}{k_r + k_{nr}}$$

where k_r and k_{nr} are the radiative and non-radiative decay rate constants and $\tau = \frac{1}{k_r + k_{nr}}$ is the fluorescence lifetime. The fluorescence quantum yield is routinely measured with calibrated fluorimeters, where the response of the detector $I_d(\lambda_f)$ at some wavelength λ_f is proportional to the fluorescence intensity $F_{em}(\lambda_f)$ through a coefficient $\phi(\lambda_{ex}, \lambda_{em})$ that depends on the geometry of the sample, the shape of excitation beam and collection efficiency of signal registration system:

$$I_d(\lambda_f) = \phi(\lambda_{ex}, \lambda_{em}) \cdot F_{em}(\lambda_f) \tag{1.3}$$

The fluorescence quantum yield is most often measured as a relative quantity exploiting a fluorescence standard, whose fluorescence quantum yield Q_{st} is known. Integrating Equation (1.3) for the standard (*st*) as well as for the sample (*x*), and rationing the resultant values we estimate:

$$Q_x = Q_{st} \frac{D_{st}(\lambda_{ex})}{D_x(\lambda_{ex})} \frac{I_x^{int}}{I_{st}^{int}} \frac{c_{st}}{c_x} \tag{1.4}$$

here I^{int} is integral fluorescence intensity, $D_{st/x}(\lambda_{ex})$, is optical density of the standard and of the sample at the excitation wavelength. If excitation and detection conditions are the same, the ratio c_{st}/c_x, that accounts for the different collection efficiencies due to the refraction at the cuvette wall, can be approximated as the ratio of the average refractive indices of the two samples in the fluorescence region, $c_{st}/c_x = (\bar{n}_x/\bar{n}_{st})^2$

While technically simple, the measure of the fluorescence quantum yield requires some attention. Specifically, accurate absorption data are needed, that

require a careful extraction of the background signal while keeping the absorbance low (<0.1). An appropriate standard must be chosen, matching excitation and emission spectra of a sample and with well-defined value of Q_{st} that should be the same order of magnitude as Q_x. The excitation and detection conditions must be optimized for good signal/noise ratio, fluorescence spectra must be carefully corrected for the spectral response of the detection system and for wavelength-dependent intensity of the excitation light source.[11]

The comparative method described above for the measurement of the fluorescence quantum yield is commonly used for samples in solution, giving an error of ~10%. Absolute fluorescence quantum yield measurements are possible using an integrating sphere that collects fluorescence light emitted by a sample in all directions. The absolute measure also applies to powders and films. In this Thesis, fluorescence quantum yields were measured *via* the comparative method, using well-established standards that will be specified for each system.

1.1.2 Fluorescence anisotropy

For solution samples the fluorescence anisotropy r is defined[9] as the difference between the intensity of emitted light components polarized along the same direction and perpendicularly to the polarized excitation beam, normalized by total emitted light intensity (see Figure 1.1):

$$r = \frac{I_{II} - I_{\perp}}{I_{II} + 2I_{\perp}} \tag{1.5}$$

Typically, anisotropy spectra are recorded with commercial spectrofluorimeters, where grating monochromators are used as the dispersing elements. The reflectivity of a grating and the sensitivity of a photomultiplier tube are greatly affected by light polarization. Therefore a correction coefficient is introduced:

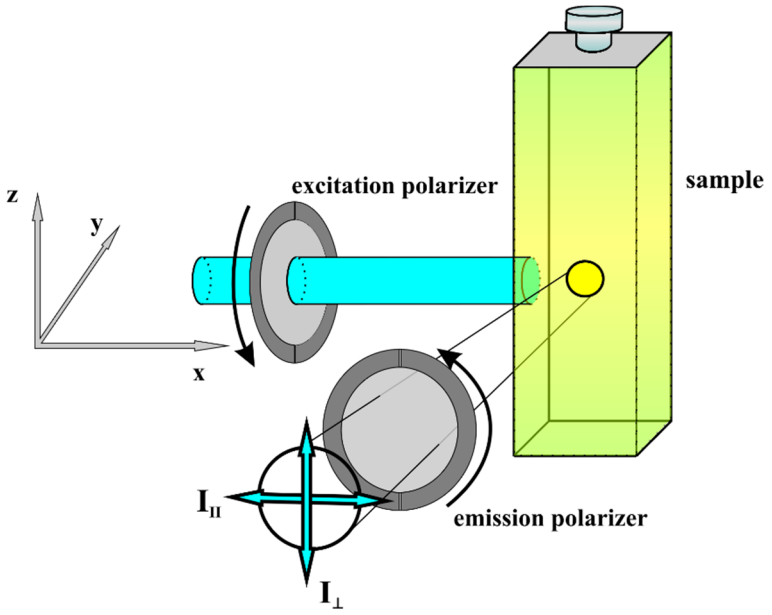

Figure 1.1 *Experimental setup for fluorescence anisotropy measurements.*

$$G = S_V/S_H$$

where S_V and S_H are sensitivities for vertically and horizontally polarized light respectively and this correction coefficient is commonly referred as G-factor that is experimentally measured as the ratio:

$$G = I_{HV}/I_{HH}$$

where the first subscript refers to the polarization of the excitation light, or the orientation of the excitation polarizer, and the second refers to the orientation of the emission polarizer, H is horizontal and V is vertical. With this information the correct expression for the anisotropy ratio is:

$$r = \frac{I_{VV} - GI_{VH}}{I_{VV} + 2GI_{VH}} \tag{1.6}$$

To avoid depolarization due to the rotational motion of the solute molecules, anisotropy measurements are usually done in rigid matrixes, such as polymers (poly (methyl methacrylate), poly (vinyl alcohol)) or undercooled solvents (2-methyltetrahydrofuran, decaline) or in highly viscous solvents, such as glycerol and polytetrahydrofuran, provided that diffusional rotation time is much longer than fluorescence lifetime to ensure that the molecules do not re-arrange prior the emission.

If $\boldsymbol{\mu}_a$ is the transition dipole moment associated with the excitation, the probability that a linearly polarized beam excites the molecule is proportional to $\mu_a^2 \cdot E^2 \cdot \cos^2\theta$, where θ is the angle between electric field **E** and $\boldsymbol{\mu}_a$.[9] And when a sample of randomly oriented fluorophores is illuminated by a linearly polarized light an oriented subpopulation of molecules is excited in a process known as photoselection. The emission probability is governed by the corresponding transition dipole moment, $\boldsymbol{\mu}_{em}$, the emitted photon being polarized along $\boldsymbol{\mu}_{em}$. In absence of depolarization processes, such as rotational motion or energy transfer, the polarization degree r_0 of emitted light (called *fundamental anisotropy)* contains information about the relative orientation of $\boldsymbol{\mu}_a$ and $\boldsymbol{\mu}_{em}$, i.e. about the angle β between them. For single-photon excitation of randomly distributed fluorophores it is described as:[9]

$$r_0 = \frac{3cos^2\beta - 1}{5} \tag{1.7}$$

According to Equation (1.7), r_0 reaches a maximum value of 0.4 for parallel absorption and emission transition dipole moments, it is equals to zero for the so called magic angle β=54.7°, and reaches a minimum $r_0 = -0.2$ value for perpendicular $\boldsymbol{\mu}_a$ and $\boldsymbol{\mu}_{em}$. Excitation anisotropy spectra reveal the spectral positions of electronic transitions and angles between transition dipole moments, otherwise not accessible from 1PA spectra. Weak or forbidden 1PA transitions are not resolved from a linear absorption spectra, but may become clearly visible

in $r(\lambda)$ spectra. Indeed, fluorescence anisotropy spectra proved to be useful in some cases for predicting the spectral positions of 2PA bands, for example in symmetric dyes, where they are not coincident with 1PA bands.

1.2 Two-photon absorption

2PA describes a third-order non-linear phenomenon when a material is excited by the simultaneous absorption of two photons. Since energy is conserved, the excitation energy is the sum of the energy of the two photons. Most often, and always in this work, the absorbed photons come from the same beam, so that the excitation energy is twice the photon energy. In these conditions, the probability of 2PA is proportional to the square of the light intensity through the 2PA cross-section δ.

1.2.1 Z-scan

Z-scan allows simultaneous measurements of both real and imaginary part of the third-order susceptibility $\chi^{(3)}$, thus providing the nonlinear absorption coefficient α_2 and the nonlinear refractive index n_2.[12] In this work we limit our attention to nonlinear absorption and we use open-aperture Z-scan, were the intensity of entire beam is monitored.

The open-aperture Z-scan works as illustrated in Figure 1.2: the sample is moved along the focused laser beam and the transmittance of the sample *T* is measured as a function of its position *z* with the respect to the focal point *z=0*. The original theory was formulated assuming a Gaussian beam, which is generally not readily available from a laser source. Since obtaining a good quality Gaussian laser beam is a tedious task, the method was extended to non-Gaussian beams, such as top-hat beams[13], Gaussian-Bessel beams[14] and near-Gaussian beams.[15] The transmittance changes as the sample approaches the

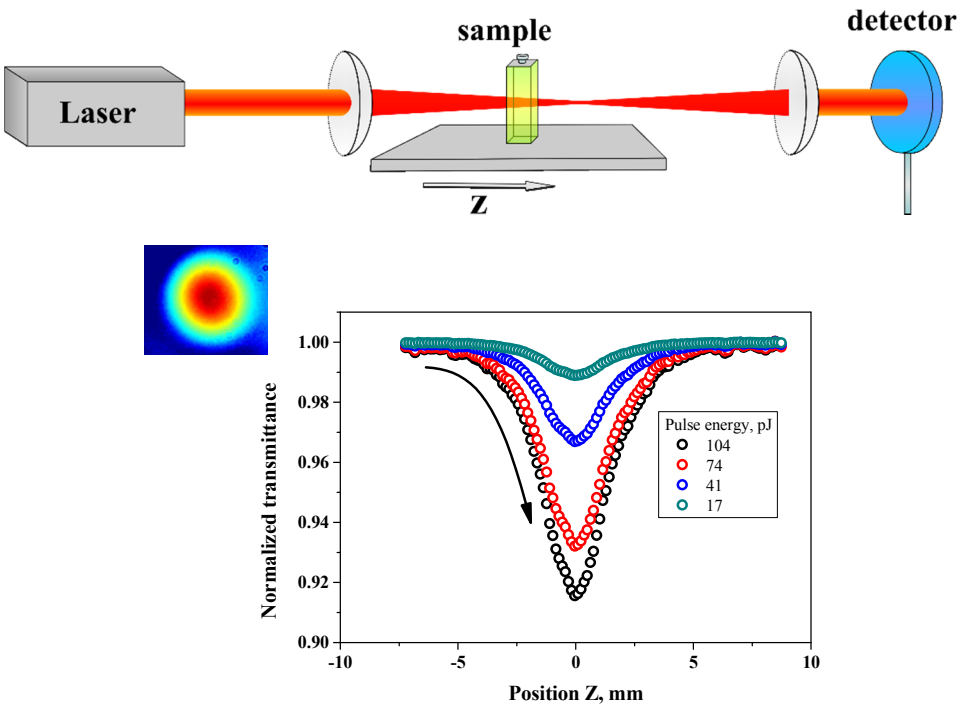

Figure 1.2 *Top – a schematic representation of an open-aperture Z-scan setup. Bottom – an example of experimental Z-scan traces. Inset – a camera image of a Gaussian beam profile.*

focal point, where the irradiance is the highest, giving information about intensity-depended beam absorption. Typical results of open-aperture Z-scan are shown in Figure 1.2.

Generally, the thickness of the sample is chosen to be smaller than the Rayleigh length ω_0^2/λ, where ω_0 is the beam waist, and λ is the wavelength. This case is known as the *thin-sample approximation* and substantially simplifies the problem of electric field propagation through nonlinear media.[12] The shape of $\Delta T(z)$ depends on the intensity of nonlinear absorption but does not provide any evidence of underlying physical process, which can be either 2PA or 1PA followed by excited state absorption (ESA). The two processes might be distinguished based on the different timescales: 2PA is an "instantaneous"

process while ESA has typical time response in the 1-100 ps regime. This allows to discriminate among the two processes based on the temporal evolution of the pump probe signal.[16] However a more reliable discrimination criterion is based on the signal dependence on the pulse width or pulse energy. Nonlinear transmittance due to 2PA is irradiation dependent while in ESA it is fluence-dependent. So, upon changing the pulse width while keeping the energy constant, the minimum value of 2PA-induced ΔT decreases, while ESA-induced ΔT remains constant. In practice it is much easier to vary the pulse energy E_p then the pulse width. Therefore for each wavelength several Z-scan traces for different pulse energies are collected. Naturally, the 2PA cross-section should be independent of the E_p.

Z-scan is an absorption-based method, meaning that it is less sensitive compared to fluorescence-based 2PF, as described below, and requires concentrated solutions (C~mM), where concentration effects can alter the results. Amongst the other factors that limit the sensitivity of single-arm Z-scan are instabilities of the beam parameters such as pulse width, energy fluctuations and the beam pointing instability. This problem is overcome in dual-arm Z-scan technique, where these noises are correlated and cancel out, hence significantly improving the sensitivity. However dual-arm Z-scan setup is much more complicated than the single-arm Z-scan setup and requires perfect balance of two channels, including equal pulse widths, energies and beams intensity distribution.

1.2.2 Two-photon excited fluorescence

Two-photon excited fluorescence method is a highly sensitive, reliable and widely used technique for measuring two-photon absorption cross-section of fluorescent samples, mainly solutions of organic dyes. The intensity of fluorescence I_d, proportional to the number of absorbed photons N_{abs}, in the case

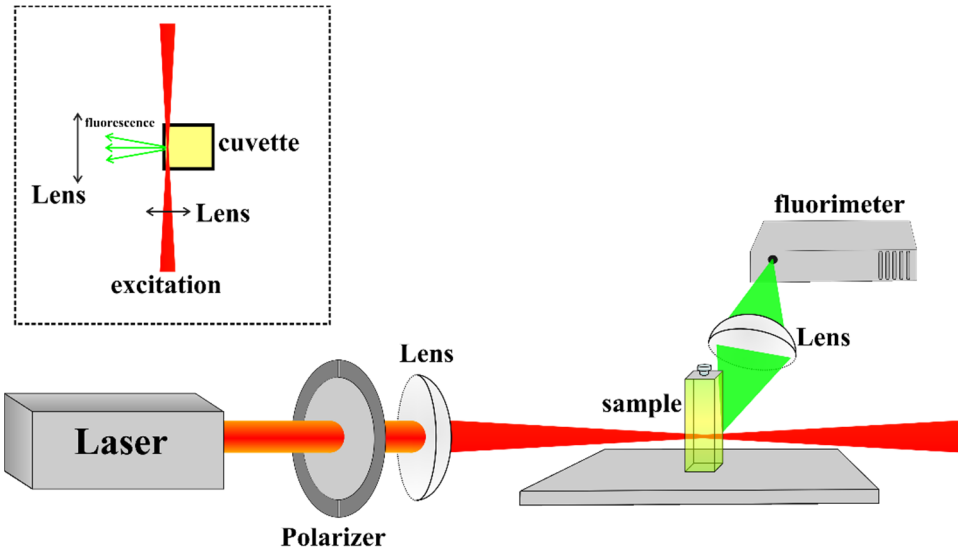

Figure 1.3 *Schematic of experimental setup for 2PF measurements. Inset – top view of the cuvette.*

of 2PA depends on the second power of incident beam intensity I and on the 2PA cross-section δ. In the thick-sample approximation[17] the time-averaged flux of emitted photons that reaches the detector is:

$$\langle F(t)\rangle = \frac{1}{2}\phi Q_{FL}\delta C\frac{g_p}{f\tau}\frac{8\langle P(t)\rangle^2}{\pi\lambda/n} \tag{1.8}$$

where ϕ is the collection efficiency of the detection system, Q_{FL} is the fluorescence quantum yield, C is the concentration, n is the refractive index of the solvent, P and λ are excitation power and wavelength, respectively. The factor $g = \frac{g_p}{f\tau}$ is a measure of the second-order temporal coherence of the excitation beam.

A mode-locked Ti:Sapphire laser generating pulses with Gaussian temporal profile (g_p=0.664, $f = 1\ kHz$ and $\tau \approx 100\ fs$) has $g \approx 10^{10}$, therefore up-converted fluorescence of majority of dyes with action cross-section $Q_{FL}\delta \geq 10\ GM$ can be detected upon excitation with relatively low-energy pulses with energy E_p~100 nJ or average power P~0.1 mW. The experimental setup is schematically shown in Figure 1.3. Because of the low efficiency of 2PA process compared to 1PA, the concentrations of the solutions are much higher than used in typical fluorescence experiments, usually of the in order of 10^{-5}-10^{-4} M. For this range of concentrations reabsorption can significantly distort the spectra, although primary reabsorption effect can be neglected, because the wavelength of exciting photons is far from the 1PA band. To reduce the effect of secondary reabsorption (i.e. of the reabsorption of emitted photons) the excitation beam is focused close to the side wall of the cuvette (see Figure 1.3).

Direct application of Equation (1.8) to estimate δ requires the knowledge of pulse duration τ and an accurate determination of the collection efficiency ϕ of the detection system, what is a tedious task.[17] Most 2PF measurements are therefore performed using standard samples, i.e. samples with known 2PA cross-sections.[18] If we take a ratio of two Equations (1.8), written for standard *st* and unknown sample *x* the dependence of δ on temporal and spatial characteristics of the beam and instrumental collection efficiency cancels out leading to the following expression:

$$\delta_x = \delta_{st} \frac{I_x^{int} C_{st} Q_{st} \langle P(t) \rangle_{st}^2 n_r}{I_{st}^{int} C_x Q_x \langle P(t) \rangle_x^2 n_{st}} \tag{1.9}$$

Here we assume that collection efficiency ϕ equals to $\phi = \phi_{inst} \cdot \phi_{sol}$, where ϕ_{inst} is instrumental contribution, due to the photomultiplier tube and monochromator and $\phi_{sol} \sim n^{-2}$ is due to the fluorescence refraction at the solvent-cuvette interface (see section (1.1). In current work we used rhodamine B in methanol and fluorescein in water (pH=11, adjusted by adding NaOH) as

standards.[18] We rely on the assumption that fluorescence quantum yield upon two-photon excitation equals that for single-photon excitation, being the emitting state the same in both cases.

In practice special care has to be taken while performing measurements with excitation falling in the edge of fluorescence spectrum, since it may cause stimulated emission. Moreover, one has to keep in mind that tightly focused ultrashort pulses may generate white light continuum (WLC) in solvent. To avoid artifacts, the quadratic dependence of integrated fluorescence intensity has to be verified for all excitation wavelengths.

In the lack of reliable standards it is possible to estimate 2PA cross-section if δ of the sample is known for at least one wavelength λ_1, for example based on results of open-aperture Z-scan. Keeping all experimental conditions constant, it is possible to determine 2PA cross-sections for other wavelength λ_2 using the relation derived from Equation (1.8):

$$\frac{\langle F(t)\rangle_1}{\langle F(t)\rangle_2} = \frac{\delta(\lambda_1)}{\delta(\lambda_2)}\frac{\tau_2\lambda_2}{\tau_1\lambda_1} \tag{1.10}$$

Although 2PF is limited to measurements of 2PA, only addressing the imaginary part of $\chi^{(3)}$, and applies mainly for fluorescent molecules in solutions (Q_{FL}>10%), yet it is a very popular and widely used technique.

1.2.3 Two-photon excited anisotropy

Two-photon transition is described with a tensor of the second rank and the probability of a degenerate two-photon transition is proportional[19] to the $\delta \cdot E^4 \cdot \cos^4\theta$, where δ is the molecular two-photon absorption cross-section and θ is angle between electric field **E** and $\boldsymbol{\mu}_a$. Due to the tensor nature of two-photon absorption for the degenerate case two excitation anisotropies can be defined,

one is defined by the same equation that defines the 1PA anisotropy (Equation (1.6)), the other is measured using circularly polarized laser light:

$$r_c^{(2PA)} = \frac{I_{cir,II} - I_{cir,\perp}}{I_{cir,II} + 2I_{cir,\perp}}$$

here $I_{cir,II}$ and $I_{cir,\perp}$ are 2PF intensities upon excitation with a circularly polarized laser beam, measured with emission polarizer oriented vertically and horizontally. In the case of two-photon excitation the photoselection has much sharper angular dependence ($\sim \cos^4 \theta$) than one-photon excitation, resulting in higher fundamental anisotropy values, which for mostly fluorescent probes are: [19],[20]

$$-0.3117 \leq r_0^{(2PA)} \leq 0.597$$

It must be noticed that in some particular cases of significant contribution of out-of-plane components of the two-photon tensor $r_0^{(2PA)}$ can take values from -0.3277 to 0.6123.[20] The theory of two-photon excited anisotropy is discussed in detail in Chapter 2.

Experimental setup for measurements of two-photon excited fluorescence anisotropy is the same as sketched in Figure 1.3, except the additional linear polarizer that is placed in front of the detector. To ensure the absence of depolarization due to the fluorescence reabsorption the shapes of up-converted fluorescence and linearly excited fluorescence from a dilute solution were compared for each sample. Complete overlap of one-photon excited fluorescence of a dilute solution with 2PF band of a concentrated solution used for two-photon excited fluorescence anisotropy measurements assures a negligible effect of secondary reabsorption.

1.3 Pump-probe and STED technique

Time-resolved spectroscopy is a powerful tool to study the ultrafast photophysics of molecular systems after impulsive excitation. In this work we employed transient absorption spectroscopy and pump-probe based STED spectroscopy to study the photophysics of fluorescent dyes.

The pump-probe setup works as follows (see Figure 1.4). The fundamental output of the Ti:Sapphire mode-locked laser was regeneratively amplified resulting in a beam consisting of a train of short pulses (pulse duration $\tau_p \approx 150$ fs, repetition rate 1 kHz and average power 1.0 W). A small portion of the beam was split by a beam-splitter, then went through the delay line M-531.DD (Physik Instrumente), introducing a delay Δt between the pump and the probe beam, and focused onto a quartz cell with MilliQ water or onto a LiF plate to generate WLC for the probe beam. The other part of the beam was frequency-doubled to the 400 nm pump pulses by second harmonics generation in BBO crystal. Two pairs of half-waveplates and linear polarizers were used to set the angle between the polarization direction of the linearly polarized pump and probe beams equal to 54.7º (magic angle).

The pump and probe beams were overlapped at a small angle within the 1 mm flow cuvette with the sample solution, in such mode that the spot size of the pump was several times larger than the probe. This is done to ensure that the probe pulse encounters the homogeneously excited sample. The concentration of the sample was $C \sim 2 \cdot 10^{-4}$ M. After the sample, the spectrum of the probe beam is recorded by the Acton SP500i spectrometer with a CCD detector and transferred to a computer. The differential optical signal was calculated by the expression:

$$\Delta D(\lambda, t_d) = D(\lambda, t_d) - D_0(\lambda) \tag{1.11}$$

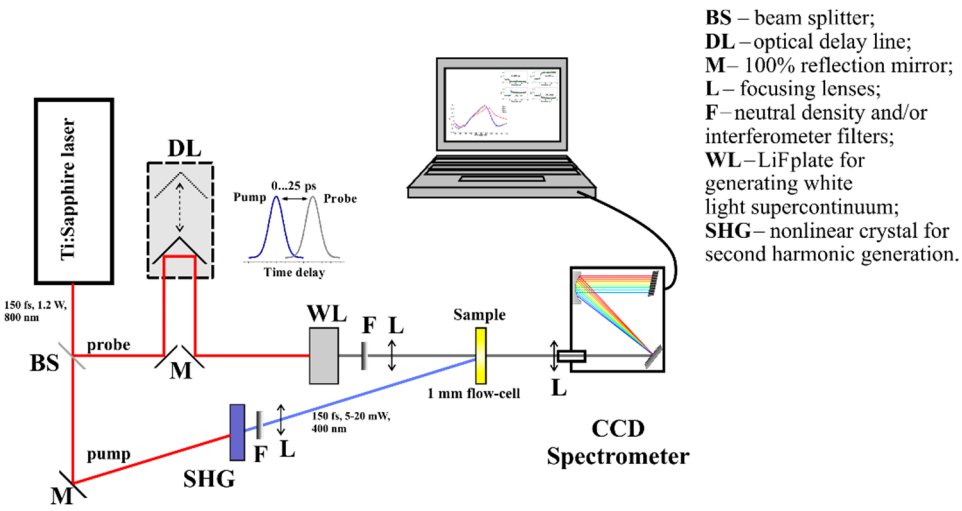

Figure 1.4 *Schematic diagram of the experimental pump-probe setup.*

here $D(\lambda, t_d)$ is the absorbance of the excited sample at time t_d after excitation and $D_0(\lambda)$ is the optical density of the equilibrium sample. Both $D(\lambda, t_d)$ and $D_0(\lambda)$ were corrected for the background signal and for white light fluctuations, measured in a reference channel (not shown for simplicity). By varying the time delay between the pump and the probe pulses, the time-resolved differential absorption spectra is obtained. For relatively simple systems, including organic dyes in absence of photoisomerization or excited-state reactions, the processes that contribute to the differential signal are:

- excited-state absorption, leading to positive ΔD;
- stimulated emission, resulting in negative ΔD;
- ground-state bleaching, resulting in negative ΔD and observed within the main absorption band.

Compared to fluorescence-based time-resolved techniques such as TCSPC method or time-resolved STED spectroscopy (see below), transient absorption spectroscopy relies on absorption and therefore it can reveal the dynamics of non-emissive states.

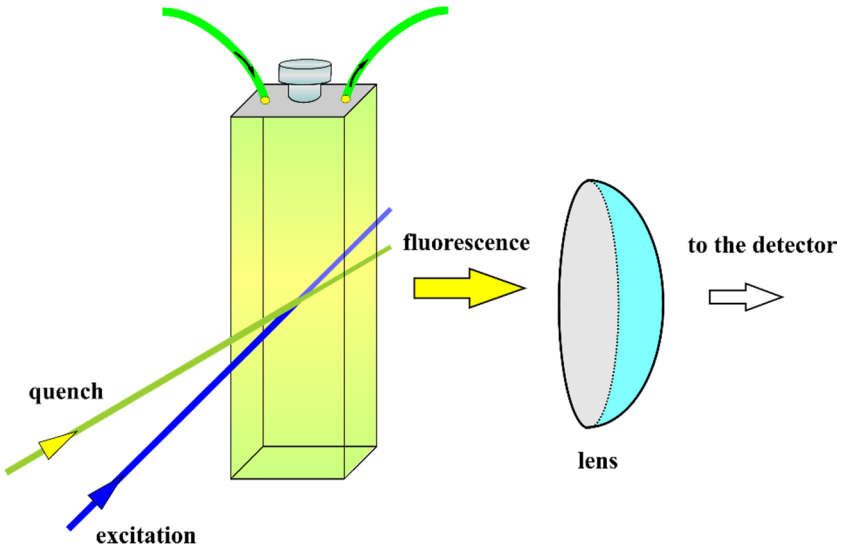

Figure 1.5 *Schematics of STED experiment.*

Molecular stimulated emission (STE) cross-section σ_{10} plays an important role in the resolution of a STED microscope,[7] and therefore accurate estimate of the magnitude and of the spectral dependence of $\sigma_{10}(\lambda)$ is required to select the most appropriate probe for given conditions and to achieve better resolution, as well for guiding the synthesis and development of new fluorescent labels. While much research effort was devoted to develop STED technique, only a few reports focused on measuring and analyzing STE cross-section, mainly from groups of A.J. Bain[21],[22] and K.D. Belfield.[23]-[25]

In this work we used the pump-probe based technique for STE cross-section measurement, firstly described by Lakowicz.[26] Optical setup and beam paths are the same as described above for the pump-probe method, but the pump beam now plays the role of the quenching beam and we need not to double its frequency and then remove the BBO crystal along that optical path. The sample is excited with light, coming from the WLC and filtered with a bandpass filter to provide excitation in the main absorption band, fluorescence signal is detected at

a right angle to the incident beam with HR4000 Ocean Optics detector (Figure 1.5). The second beam pumped the TOPAS-800-fs ultrafast optical parametric amplifier. The output of TOPAS-800-fs (1 kHz, 100 fs) can be tuned in a wide spectral range and served as a quenching beam. For obtaining the most effective depopulation of the excited state, the quenching pulse has to be delayed with respect to the excitation pulse by ~10 ps, so that the excited state population relaxes to the lowest vibrational state of the first electronic excited state. In this case the degree of fluorescence quenching is:[25]

$$1 - \frac{I_F}{I_{F_0}} = \frac{2\lambda_q \sigma_{10}(\lambda_q)}{\pi hc(r_p^2 + r_q^2)} E_q \qquad (1.12)$$

where I_F and I_{F_0} are integral fluorescence intensities observed with and without applying the quenching beam, $\sigma_{10}(\lambda_q)$ is the STE cross-section, r_p is the radius of the pump beam, r_q and E_q are the radius and pulse energy of the quenching beam. The value of fluorescence quenching is directly proportional to the quenching pulse energy, and by varying the pulse energy the STE cross-section can be obtained as a slope of the linear dependence $1 - I_F/I_{F_0} \sim \sigma_{10}(\lambda_q) \cdot E_q$. Temporal evolution of $1 - I_F/I_{F_0}$ as a function of time delay between excitation and quenching pulses can also be obtained by using the delay line and ultrafast excited-state processes can be monitored. However, this information is already contained in pump-probe spectra, and time-resolved STED spectroscopy is limited to the evolution of fluorescent state.

For observing noticeable (5-15%) fluorescence decrease strong (≤20 μJ/pulse) and tightly focused (r_q~0.2-0.5 mm) quenching beam is utilized. Therefore a flow cell was used to minimize various undesirable effects such as local heating and photobleaching (Figure 1.5).

1.4 Amplified spontaneous emission

Superluminescence or amplified spontaneous emission (ASE)[27],[28] is a photophysical process occurring upon pulsed excitation, intense enough to create an inverted population among two states. In this Thesis we will use the term "amplified spontaneous emission" since it reflects the nature of the process. ASE has a clear threshold character, and when the pump intensity overcomes a critical value, the sample emission grows almost exponentially with the pump intensity, until saturation. Typical amplification factors are 10^3-10^5. The amplification is accompanied by a pronounced spectral narrowing, with the full width at half maximum (FWHM) decreasing from 70-110 nm typical of fluorescence bands down to 10-15 nm. In contrast to lasing, ASE emission occurs without any optical feedback, i.e. it results from a single-pass amplification. It begins from a stimulated emission process: in an inverted population medium a spontaneously emitted photon stimulates emission of other photons along the direction of its propagation, resulting in a directed and intense light pulse. Fairly concentrated solution are used for ASE (C~ mM), and the maximum of ASE usually does not coincides with the maximum of the stimulated emission band, since it is a result of an interplay between gain and reabsorption. Although ASE generates intense, directional and spectrally narrow light, it should not be confused with laser radiation.

Figure 1.6 shows a schematic of experimental setup. A cylindrical lens was used to focus the frequency-doubled, vertically polarized, femtosecond pump beam from a Ti:Sapphire laser. Laser source was either Coherent Mira-900 F outputting 100 fs 800 nm beam used to study ASE of fluorene derivative **s1** or Clark-MXR CPA-2110 with 140 fs 775 nm output for pumping fluorene derivative **s2** (see Chapter 2). The sample solution was put in a standard quartz 1.0cm×1.0 cm×4.0 cm cuvette with concentrations of **s1** or **s2** dyes C~1 mM. Since a cylindrical lens creates a stripe-shaped excited volume, the highest

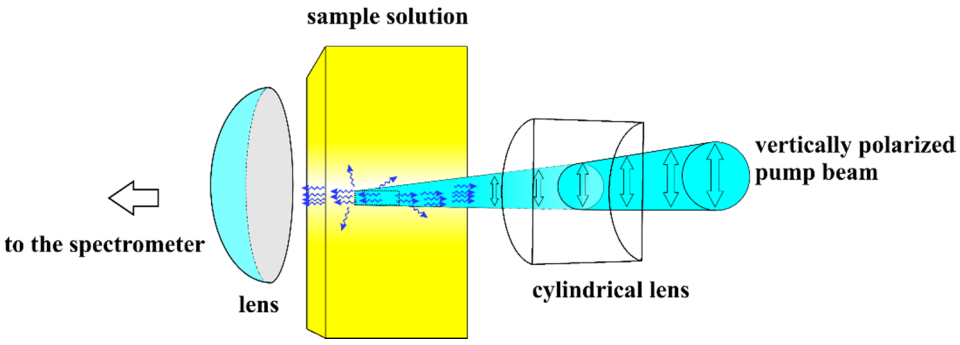

Figure 1.6 *Schematic of ASE measurements*

amplification is observed along the longest axis of the excited volume, therefore emission was collected in a direction perpendicular to the excitation beam with a high aperture lens and detected with a HR4000 Ocean Optics CCD spectrometer.

1.5 Photochemical stability

If we apply the definition of quantum yield (given in section 1.1.1) to the number of photobleached molecules N_{mol} per number of absorbed photons N_{abs} we obtain the *quantum yield of photodecomposition*:[29]

$$Q_{PH} = \frac{N_{mol}}{N_{abs}} \tag{1.13}$$

In microscopy often the inverse value $1/Q_{PH}$ is used, showing the number of excitation cycles a molecule can undergo before photobleaching (survival rate). The ratio of fluorescence quantum yield and quantum yield of photodecomposition Q_{FL}/Q_{PH} gives the number of excitation-emissive cycles.[29] Photochemical stability is one of the most important characteristics of fluorophores for nonlinear optical applications. In conventional one-photon excitation and 2PF confocal microscopy photostable labels provide better

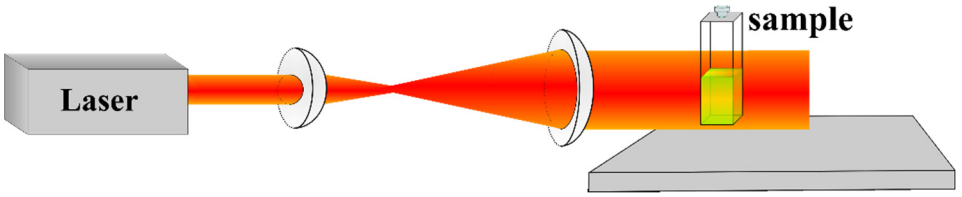

Figure 1.7 *Experimental setup for photostability measurements.*

contrast, since more fluorescence photons can be collected. In STED microscopy highly photostable labels are required allowing higher depletion beam intensities, therefore enhancing the resolution.[7] The quantum yield of photodecomposition is a quantitative characteristic of molecular photostability and allows direct comparison of performance of different labels. Despite of this, relative measurements, which depend on the experimental parameters are still commonly found in the literature.[30]-[32] Several method were developed for measuring the Q_{PH}, for example cell-bleaching and fluorescence correlation spectroscopy, that however are limited to dilute solutions of fluorescent dyes, while molecular diffusion and beam intensity profile must be properly accounted for.[29]

We adopt a comparatively simple and flexible method developed by Belfield et al.[33] In this approach the whole volume of a sample in a cuvette is irradiated with a beam with quasi-uniform intensity distribution. Powerful UV lamps with a bandpass filters, or a laser beam expanded with a telescope (see Figure 1.7) can be used to obtain a spot size large enough to illuminate the whole volume simultaneously. The number of photobleached molecules is then monitored by the decrease in either fluorescence or absorbance. Fluorescence method is applied for dilute samples with absorbance $D < 0.1$ in 10 mm pass, and absorption method is used to study concentrated samples with absorbance $0.5 \leq D \leq 2$. Upper and lower bounds of D in the latter case depend on the sensitivity of a detector. The number of absorbed photons can be estimated

knowing the intensity P of the excitation beam measured in photons·cm^{-2}·s^{-1} and the absorbance of a sample. Quantum yield of photodecomposition using the absorbance-based method[33] is then calculated as:

$$Q_{PH}^{(abs)} = \frac{N_{mol}}{N_{abs}} = \frac{(D(\lambda,0) - D(\lambda,T))N_A}{10^3 \cdot P \cdot \varepsilon(\lambda_{exc}) \int_\lambda \int_0^T (1 - 10^{-D(\lambda,t)}) dt d\lambda} \quad (1.14)$$

And in fluorescence-based approach:

$$Q_{PH}^{(fl)} = \frac{N_{mol}}{N_{abs}} = \frac{1 - F(T)/F_0}{P \cdot \sigma(\lambda_{exc}) \int_0^T (F(t)/F_0) dt} \quad (1.15)$$

here λ_{exc} is the excitation wavelength, 1PA cross-section can be calculated as $\sigma(\lambda) = N_A/ln10 \cdot \varepsilon(\lambda) \approx 3.8 \cdot 10^{-21}\varepsilon(\lambda)$ ($\varepsilon(\lambda)$ in M^{-1}cm^{-1}, $\sigma(\lambda)$ in cm^2). These methods are applicable for studies of Q_{PH} for dyes in solution in a wide concentration range, from μM to mM, as well as can easily be extended for the case on nonlinear excitation.[33]

2 PHOTOPHYSICS OF FLUORENE DERIVATIVES AND ORGANIC NANOPARTICLES

In this chapter we discuss the photophysical properties and the photochemical stability of two fluorene derivatives, an asymmetric derivative 3,3'-(2-(benzo[*d*]thiazol-2-yl)-7-(diethylamino)-9*H*-fluorene-9,9-diyl)dipropanenitrile (**s1**) and a symmetric derivative 2,2'-((1E,1'E)-(9,9-diethyl-*9H*-fluorene-2,7-diyl)bis(ethene-2,1-diyl))bis(1-methyl-1H-pyrrole) (**s2**).
Relevant chemical structures are presented in Figure 2.1. These dyes belong to the family of quadrupolar chromophores and can be described as two equivalent (**s2**) or inequivalent (**s1**) electron donating (D) and/or electron withdrawing (A) groups connected by linear π-conjugated chains. According to this approach the substitution pattern for **s1** dye can be written as $D-A-R$, where D is the electron-donating diethylamino group, A is the fluorene core and R is the benzothiazole unit acting as a weak electron donor.[34] The substitution pattern for **s2** dye is $D-A-D$, where D is the pyrrole group. Both dyes were synthesized in Prof. K. D. Belfield's lab. Synthetic route for **s2** is described in Appendix A, **s1** was obtained according to the procedure reported in Ref.[35]

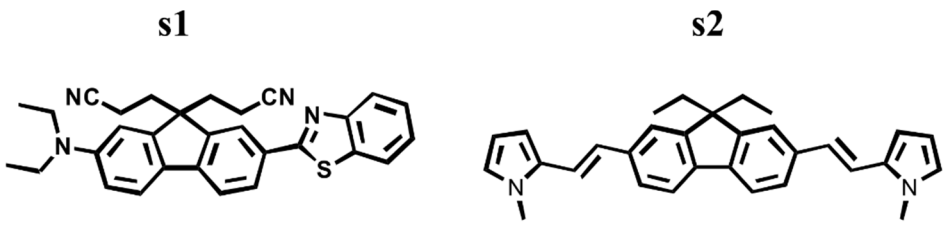

Figure 2.1. *Molecular structures of compound **s1** and **s2**.*

Linear spectral properties including fluorescence quantum yields, fluorescence lifetimes and fluorescence excitation anisotropy were studied in air saturated solvents covering a wide range of polarity – cyclohexane (CHX), toluene (TOL), tetrahydrofuran (THF), dichloromethane (DCM), acetonitrile (ACN) and dimethyl sulfoxide (DMSO). Fundamental one- and two-photon excitation anisotropy spectra were measured in highly viscous polytetrahydrofuran (pTHF, average molar weight M_n=250).

We also studied various nonlinear optical properties of **s1** and **s2.** Degenerate two-photon absorption processes were studied by Z-scan and 2PF techniques and 2PA cross-sections were determined in a wide spectral range. Using ultrafast transient absorption spectroscopy we obtained excited state absorption and stimulated emission spectra. Considerable gain of **s1** and **s2** dyes allowed investigation of amplified stimulated emission in polar solvent. Time-resolved stimulated emission depletion and spectral dependence of stimulated emission (STE) cross-section were determined by pump-probe fluorescence quenching technique. Comprehensive photophysical studies are complemented with photochemical stability measurements and essential-state theoretical modeling.

2.1 Linear photophysical properties of fluorene derivatives

Linear absorption, emission and excitation anisotropy spectra of **s1** and **s2** are presented in Figure 2.2. Table 1 collects relevant photophysical and photochemical properties of **s1** and **s2** dyes. Both compounds show strong and broad one-photon absorption bands in the region 383-407 nm and fluorescence bands in the range 450-550 nm.

Absorption spectra of **s1** and **s2** in non-polar CHX show a weak vibrational shoulder at the long-wavelength edge that smears out in polar

Table 1. Main photophysical and photochemical properties of **s1** and **s2**. Absorption λ_{max}^{abs} and emission λ_{max}^{fl} wavelengths maxima; ε_{max} is the extinction coefficient at λ_{max}^{abs}; Q_{fl} is the fluorescence quantum yield; τ_{fl} - the fluorescence lifetime, τ_{rad} - the radiative lifetime; τ_n^{SB} is the Strickler-Berg radiative lifetime and Q_{ph} is the photodecomposition quantum yield.

	s1						**s2**				
	CHX	TOL	THF	DCM	ACN	DMSO	CHX	TOL	THF	DCM	ACN
λ_{max}^{abs}, nm	383	394	398	399	397	407	397	403	402	402	398
λ_{max}^{fl}, nm	439	463	491	495	534	545	431	442	471	472	474
ε_{max}, 10^3 $M^{-1}\cdot cm^{-1}$	53	46	44	48	46	47	72	75	74	77	78
Q_{fl}, %	96	95	86	95	80	88	62	70	60	50	52
τ_{fl}, ns	1.4	1.6	1.9	2.0	2.4	2.4	1.0	1.0	1.1	1.2	1.3
τ_{rad}, ns	1.5	1.7	2.2	2.1	3.0	2.7	1.6	1.4	1.8	2.4	2.5
τ_n^{SB}, ns	2.2	2.5	3.2	3.0	4.0	3.5	1.4	1.4	1.6	1.5	1.8
Q_{ph}, 10^{-4}	0.5	0.2	0.09	0.4	10	-	40	50	40	50	80

solvents. The absorption solvatochromism for both dyes is modest. For both dyes fluorescence spectra were independent of the excitation wavelengths and excitation spectra perfectly match absorption bands, in agreement with the Kasha's rule.[9] In contrast to absorption, the fluorescence spectra of **s1** show a strong positive solvatochromism. This effect is known for small asymmetrical fluorene derivatives that are weakly polar or non-polar in the ground state, and become significantly polar after photoexcitation. This leads to the solvent rearrangement around the solute in the excited state resulting in large Stokes shifts in polar environments. For the symmetric fluorene derivative **s2** the fluorescence Stokes shifts are smaller than for **s1**, suggesting a symmetry-broken excited state as expected for class I quadrupolar dyes.[36] In nonpolar solvents the fluorescence band of both dyes show a resolved vibronic structure that vanishes in polar solvents.

The Lippert plots for **s1** and **s2** in Figure 2.2 (c, d) show the Stokes shift dependence on Δf, the Lippert parameter measuring the solvent polarity, $\Delta f = \frac{\varepsilon-1}{2\varepsilon+1} - \frac{n^2-1}{2n^2+1}$, where ε and n are the dielectric constant and refractive index of solvent, respectively. The good linearity of the two plots is in line with the Lippert equation,[9] $\Delta\bar{\nu} \sim \Delta f \Delta\mu^2$, that relates the Stokes shift $\Delta\bar{\nu}$ to the squared mesomeric molecular dipole moment Δμ, the difference between the ground and excited state molecular dipole moments. Linear Lippert plots and the solvent-independent values of the transition dipole moments in Table 1 suggest minor variations of chromophore polarity in different solvents and show that the solvatochromism is driven by general solute-solvents interactions defined by the solvent polarity, while specific interaction can be neglected in the studied solvents.

Both dyes exhibit high fluorescence quantum yields, with Q_{fl} reaching 70% in **s1**, and approaching unity for **s1**. The fluorescence follows a mono-exponential decay with lifetimes in ~1-2 ns range, slightly increasing with the solvent polarity.

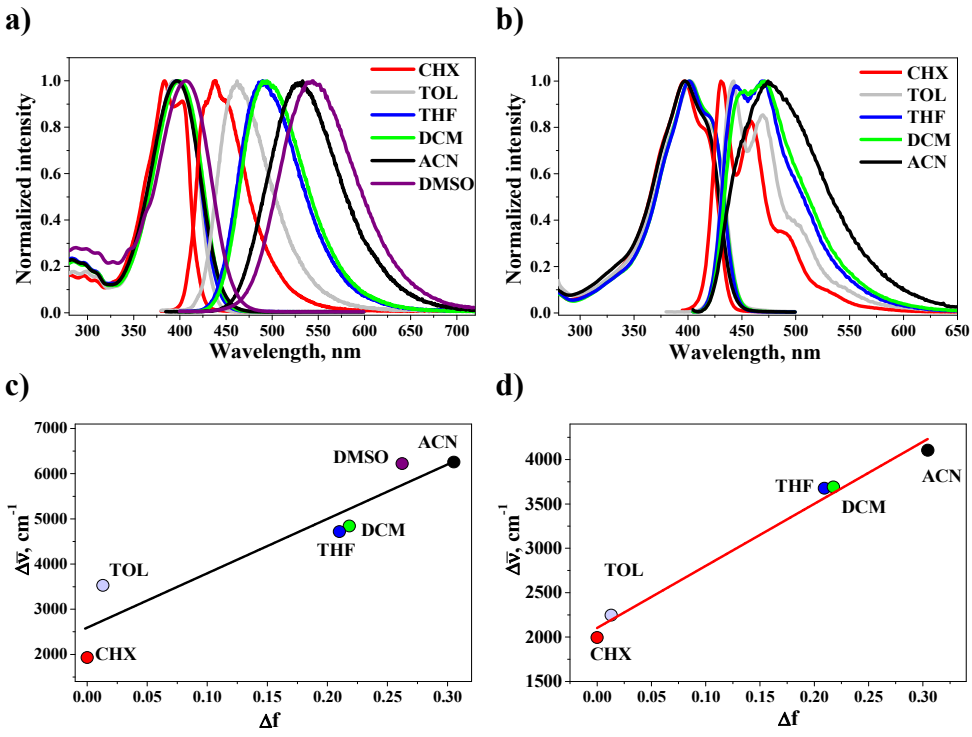

Figure 2.2. *(a, b) Normalized absorbance and fluorescence spectra of **1** (a) and **2** (b) in solvents of different polarity. (c, d) Lippert plots for **s1** (c) and **s2** (d) compounds.*

Radiative fluorescence lifetimes were estimated as $\tau_{rad} = \tau_{fl}/Q_{fl}$ and were compared with values obtained using the Strickler-Berg equation:[37]

$$1/\tau_n^{SB} = 2.88 \cdot 10^{-9} n^2 \, \varepsilon_{max} \int I_{fl}(\bar{\nu}) d\bar{\nu} \times \int {\varepsilon(\bar{\nu})}/{\bar{\nu}} \, d\bar{\nu} \Big/ \int I_{fl}(\bar{\nu}) \bar{\nu}^{-3} d\bar{\nu}$$

where τ_n^{SB} is the natural lifetime in s, n is the refractive index of the solvent at the fluorescence maximum wavelength, ε_{max} is maximum extinction coefficient (in $M^{-1}cm^{-1}$), I_{fl} and $\varepsilon(\bar{\nu})$ are normalized fluorescence and absorption spectra plotted against the wavenumber $\bar{\nu}$ (in cm^{-1}). Results in Table 1 show that the τ_n^{SB}

estimates of the lifetimes deviate from the radiative lifetimes for both **s1** and **s2**. The differences can be ascribed to the limitation of Strickler-Berg approach, which assumes no changes in the configuration in the excited state.[37]

Excitation anisotropy spectra for **s1** and **s2** are shown in Figure 2.3 (a, b). As it was discussed in Chapter 1 the excitation anisotropy contains not only important information about the nature of 1PA band, but also reveals the mutual orientation of transition dipole moments in higher excited states and the emission dipole moment. In non-viscous solvents the fast rotation of the fluorophore before emission results in fluorescence depolarization, so the measured (or limiting) value of anisotropy r is:[9]

$$r = \frac{r_0}{1 + \tau_{fl}/\theta_{\mathrm{rot}}} \tag{2.1}$$

where r_0 is fundamental anisotropy (see Equation (1.7)), and $\theta_{\mathrm{rot}} = \eta V/kT$ is the correlation rotational time, which depends on the solvent viscosity η, temperature T and effective molecular rotational volume of a molecule, *k* is the Boltzmann constant. Equation (2.1) can be re-written as:

$$\frac{1}{r} = \frac{1}{r_0} + \frac{kT}{r_0 V} \cdot \frac{\tau_{fl}}{\eta} \tag{2.2}$$

Therefore, a plot of $1/r$ versus τ_{fl}/η gives access to the molecular rotational correlation time, θ_{rot}. For both compounds plots in Figure 2.3 lead to θ_{rot}~100 ps, at least 10 times smaller than the fluorescence lifetime. The linearity of the plots and the independence of the $r(\lambda)$ shape for both **s1** and **s2** on the solvent demonstrate that the relative orientation of transition dipole moments is not affected by polarity and that the effective molecular rotational volume V is solvent-independent.

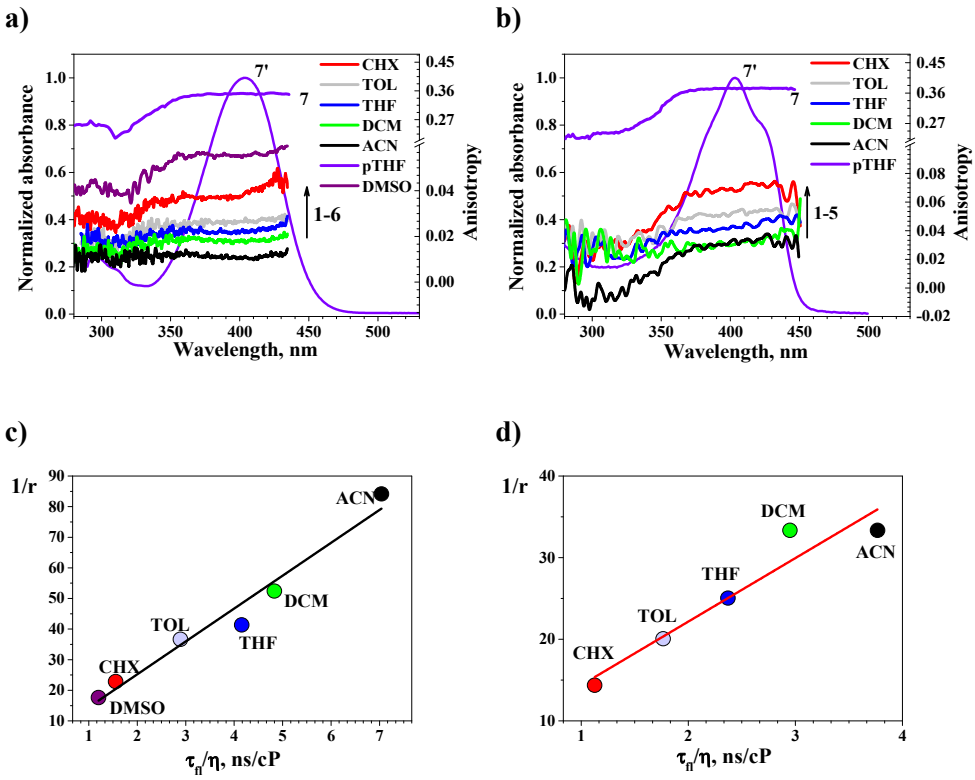

Figure 2.3. *Normalized absorption spectra of **s1** (a) and **s2** (b) in pTHF (7') and excitation anisotropy spectra of **s1** (a) and **s2** (b) in ACN (1), DCM (2), THF (3), TOL (4), CHX (5), DMSO (6) and pTHF (7). (c, d) Inverse anisotropy dependence on fluorescence lifetime over solvent viscosity for **s1** (c) and **s2** (d).*

Fundamental anisotropy spectra of **s1** and **s2** were obtained in highly viscous pTHF, where the high solvent viscosity ensures that $\theta_{rot} \gg \tau_{fl}$. In these conditions fluorescence excitation anisotropy is governed by β, the angle formed by the transition dipole moment related to the absorption and fluorescence processes (see Equation (1.7)). The constant values of excitation anisotropy spectra within the main absorption band of **s1** and **s2** can be associated with a single $S_0 \rightarrow S_1$ electronic transition. The anisotropy value of 0.35-0.37 is close to the maximum value of 0.4 for randomly distributed chromophores in solutions

and indicates almost parallel absorption and emission transition dipoles moment with β ≈16º and ≈13º for **s1** and **s2**, respectively. In the short wavelength region anisotropy decreases and for **s1** a dip at λ~300 nm with r~0.21 is observed, while for **s2** a decrease in $r(\lambda)$ starting at ~370 nm is followed by almost constant values of anisotropy in 280-350 nm spectral region. The decrease in anisotropy is due to an electronic transition (or to a group of transitions) with dipole moments that are not collinear to the emission transition dipole moment. The anisotropy value r~0.23, measured for **s2** is however puzzling. In fact it points to an angle β~32º between transition dipole moments, while the symmetry of the system only supports either collinear or perpendicular dipole moments. This puzzling result will be rationalized by essential state models, in terms of inhomogeneous broadening effects related to polar solvation.

Fundamental anisotropy spectra are useful to predict the position of 2PA bands. For asymmetric **s1** both $S_0 \rightarrow S_1$ and $S_0 \rightarrow S_2$ are allowed in one- and two-photon absorption, even if with different relative intensities. Both transitions are formally allowed in the symmetric **s2** dye, because of its bent structure. But since the bending angle is very small, the $S_0 \rightarrow S_2$ is not seen in 1PA spectra. The spectral position of the dip in the anisotropy spectra of symmetrical **s2** can potentially show the one-photon forbidden but two-photon allowed transition, therefore locating the position of 2PA maximum.

2.2 Photostability

The photochemical stability of **s1** and **s2** compounds was studied using low intensity excitation in the 1PA maximum and estimating photodecomposition quantum yields according to Equation (1.14). Results in Table 1 were obtained in different solvents for dye concentrations C~20-30 μM. Examples of **s1** and **s2** photobleaching behavior under continuous-wave (CW) laser irradiations are presented in Figure 2.4.

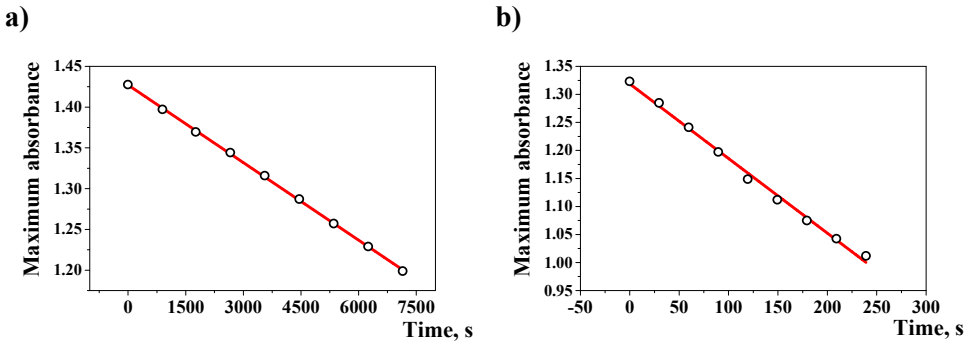

Figure 2.4. *Maximum absorption decay of **s1** (a) and **s2** in toluene under CW irradiation (λ_{irr}≈400 nm, power density 5 mW·cm^{-2}).*

The linear $D(\lambda_{max}, t_{irr})$ dependence on the irradiation time suggests that the absorbance of photoreaction products close to 400 nm is negligible and does not affect the measurements.

s1 dye shows low photodecomposition quantum yields in all solvents, except ACN. Low photostability in polar solvents is typically observed for fluorene derivatives, and in some cases Q_{ph} in ACN or DCM can be 1-2 orders of magnitude higher than in non-polar media.[38]-[40] The solvent dependence of Q_{ph} is determined by various factors, including specific solute-solvents interactions (H-bonding, electron transfer), viscosity dependent oxygen diffusion or solvent-specific oxygen solubility. Detailed discussion can be found, for example in Ref.[29],[39].

The measured Q_{ph} values for **s1** are comparable with those of typical laser dyes. For example, for rhodamine 6G Q_{ph} is in the range $0.5 \cdot 10^{-6}$-$1.5 \cdot 10^{-5}$ depending on the excitation conditions and the solvent.[29] The high fluorescence quantum yield **s1** and its good photostability in low-to-moderate polarity solvents make it an interesting probe for photonics application. Another useful parameter can be the ratio of fluorescence and photodecomposition quantum

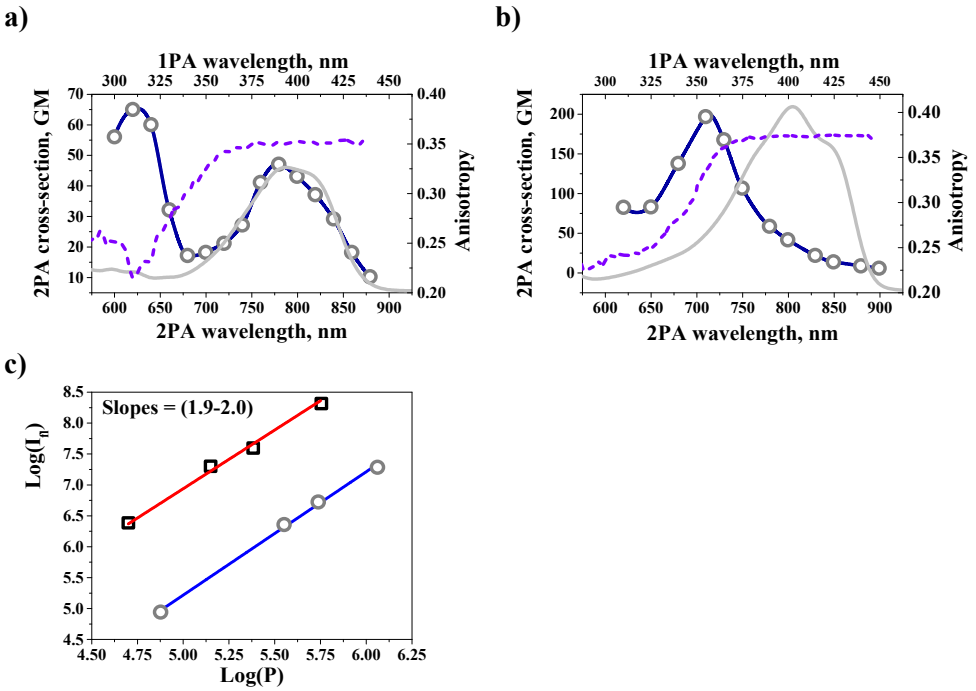

Figure 2.5. *(a, b) 2PA spectra (grey circles), 1PA (grey line) and excitation anisotropy (blue dashed line) of **s1** (a) and **s2** (b) in TOL. Blue line is to guide an eye. c) Logarithmic plots of dependence of emission intensity of s2 (gray circles) and fluorescein (black squares) on the excitation power upon excitation at λ_{exc}=620 nm. Blue and red line is a linear fit.*

yields Q_{fl}/Q_{ph}, giving a number of the excitation-emission cycles a molecule can undergo in average. For example in THF **s1** molecule can survive 10^5 excitation-emission cycles before bleaching. As contrasted with **s1**, compound **s2** exhibits lower photostability however it does not show significant increase in Q_{ph} for polar solvents.

2.3 Two-photon absorption

Degenerate two-photon absorption spectra of fluorene derivatives **s1** and **s2** are shown in Figure 2.5. 2PA spectra of **s1** and **s2** were measured using Z-scan and 2PF techniques respectively. Open-aperture Z-scan traces of **s1** were acquired at different pulse energies for each wavelength to ensure the absence of ESA process (data not shown). The quadratic dependence of fluorescence intensity of **s2** and fluorescein (used as a standard dye) under femtosecond excitation was verified for all wavelengths, confirming the pure two-photon nature of the excitation process. Examples of the logarithmic plots used in this respect are plotted in Figure 2.5.

The 2PA spectrum of **s1** reveals two peaks at 620 and 780 nm with maximum values of 2PA cross-section of 65 and 47 GM respectively. These values are somewhat smaller than expected for small asymmetrical quadrupolar fluorene derivatives, typically showing 2PA cross-sections between 100-300 GM.[41],[42] The long wavelength 2PA band almost perfectly matches the 1PA absorption contour that along with the constant values of anisotropy, confirms that both bands are due to the same $S_0 \rightarrow S_1$ transition.

s2 exhibits only one peak in 2PA spectrum, with maximum of 200 GM at 710 nm. Indeed, for bent symmetric quadrupolar dyes both S_1 and S_2 states should be attainable by 2PA process, however the bending angle in **s2** is too small to effectively break the selection rule holding for symmetrical dyes where 1PA and 2PA address different excited states.

2.4 Ultrafast transient absorption and gain

Subpicosecond transient absorption measurements of **s1** and **s2** were studied in nonpolar (toluene) and polar (acetonitrile) aprotic solvents in a broad spectral range. The variation of the optical density ΔD, was measured as a

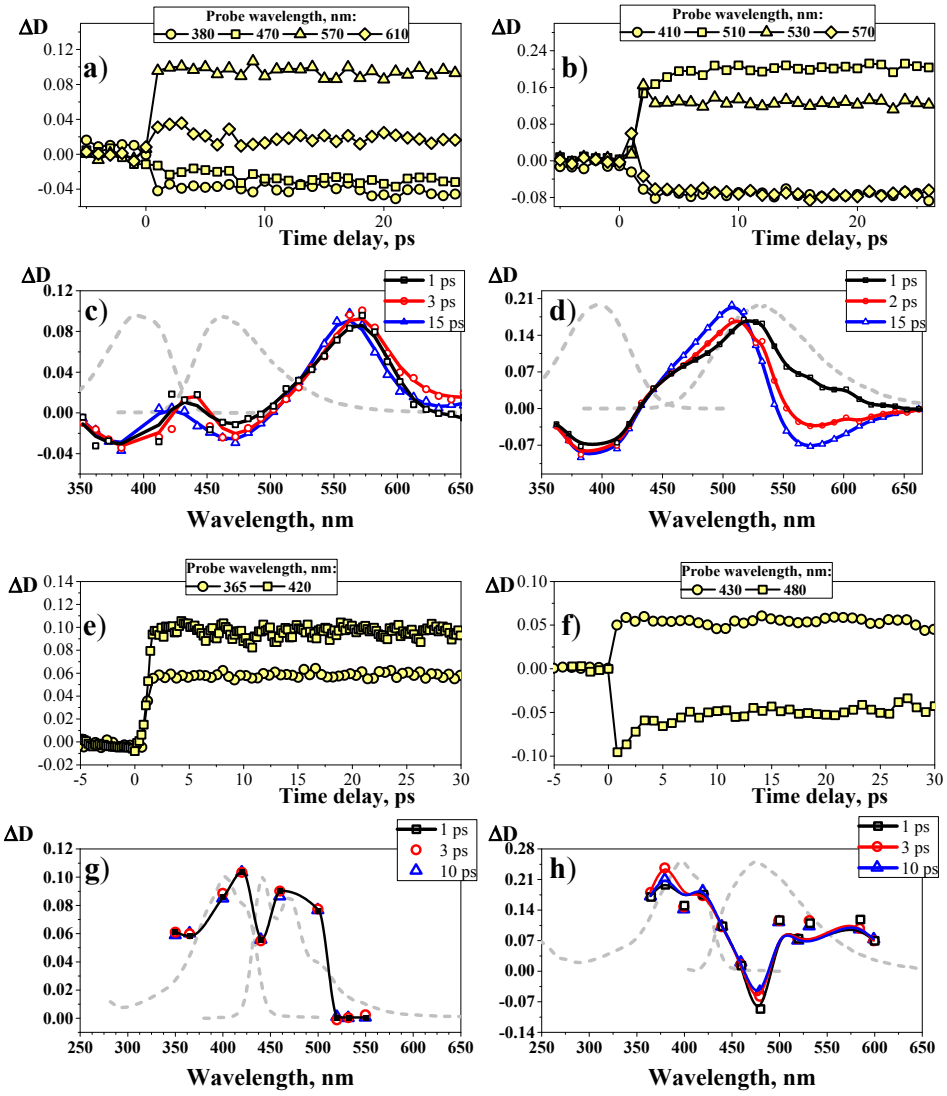

Figure 2.6. *Transient absorption of **s1** (a, b, c, d) and **s2** (e, f, g, h). Temporal dependence of $\Delta D(t_d)$ (a, b, e, f) and spectral dependence of $\Delta D(\lambda_{probe})$ (c, d, g, h) for dyes in toluene (a, c, e, g) and acetonitrile (b, d, f, h). Steady-state 1PA and fluorescence spectra of **s1** and **s2** are shown with dashed gray lines in (c, d, g, h).*

function of the delay time t_d between probe and pump pulses and of the probe wavelength, λ_{probe}. Results are shown in Figure 2.6

Transient absorption spectra of **s1** in nonpolar solvent reveal bleaching (saturable absorption) near 400 nm, due to the depopulation of the ground state, a strong positive band at 570 nm, attributed to ESA, and a weak, partly masked by ESA, gain signal within the fluorescence band. The gain and ESA signals arise within the instrument response time, remain constant during the measurements and then slowly decay to zero according with the fluorescence lifetime. This suggests that all ultrafast dynamics subsequent the electronic excitation including vibrational and solvent relaxation processes end within the first 300-500 fs after photoexcitation. The lack of any sizeable evolution of the transient absorption points to marginal rearrangement of the non-polar solvent around the excited solute.

Results are different in polar solvent, as shown in Figure 2.6 (d). While the temporal dynamics of ground state bleaching is similar as in toluene, more features appear in the fluorescence region of **s1** in acetonitrile. ESA peak at 530 nm exhibits a blueshift to ~515 nm in the first 3 ps after photoexcitation, accompanied by spectral narrowing. This dynamics can also be observed in the $\Delta D(t_d)$ traces shown in Figure 2.6 (b) that fit well to monoexponential function with the lifetime ~2 ps. The spectral evolution of ESA can be attributed to the solvent relaxation process. As it follows from the steady-state fluorescence data, large Stokes shift of **s1** in polar solvents is indicative of large dipole moment increase in the excited state. Therefore the picosecond reorientation of polar solvent molecules following the photoexcitation of **s1** results in the excited state energy stabilization and gives rise to the blue shift of the ESA band. After relaxation, a strong gain ($\Delta D < 0$) appears at 570 nm and remains constant within the experimental time window.

Transient spectra of symmetric **s2** dye in toluene show positive ΔD over the entire investigated spectral region, suggesting a presence of strong ESA absorption that overwhelms the ground state bleaching (see Figure 2.6 (e)).

Kinetic traces $\Delta D(t_d)$ do not show any evidence of slow solvent dynamics or other relaxation process, apart from the nanosecond decay, suggesting much as for **s1** the lack of any solvent dynamics following the solute photoexcitation. In polar ACN, a stimulated emission signal appears within the fluorescence band and a fast (~2-3 ps) relaxation process is observed in the $\Delta D(t_d)$ transient absorption signal at 480 nm (see Figure 2.6 (f)). As with **s1,** this decay is associated with the solvent reorientation around excited chromophore. In line with the observed fluorescence solvatochromism, **s2** has a broken symmetry (polar) relaxed excited state.

2.5 Steady-state and time-resolved stimulated emission depletion

The strong stimulated emission signals observed in the pump-probe spectra make **s1** and **s2** promising candidates for studying light amplification (ASE and lasing) phenomena in polar solvents. Also stimulated optical transitions were studied for **s1** and **s2** in ACN. Spectral dependence of STE cross-section are shown superimposed with fluorescence spectra for **s1** and **s2** in ACN in Figure 2.7 (a, b). The values of STE cross-sections σ_{10} were obtained using pump-probe-based method in the 480-565 nm spectral range with fixed delay ~10 ps$\ll \tau_{fl}$ between pump and quench pulses.

Typical dependence $1 - I_q/I_F \sim E_q$ where I_F and I_{F_0} are integral fluorescence intensities observed with and without the application of the quenching beam with energy E_q are shown in Figure 2.7. They were found to be linear for all wavelengths, meaning that possible ESA processes do not contribute to the losses in the fluorescence intensity I_F, therefore the values of σ_{10} can be estimated from the corresponding slopes (see Equation (1.12)). Spectral dependence of $\sigma_{10}(\lambda_q)$ is very close to the shape of steady-state fluorescence contour for both compounds. The maximum value of STE cross-section of **s1** was $\sigma_{10}^{max} \approx 1.2 \cdot 10^{-16}$ cm^2 and for **s2** $\approx 1.3 \cdot 10^{-16}$ cm^2 which is significantly smaller than corresponding one-photon absorption cross section

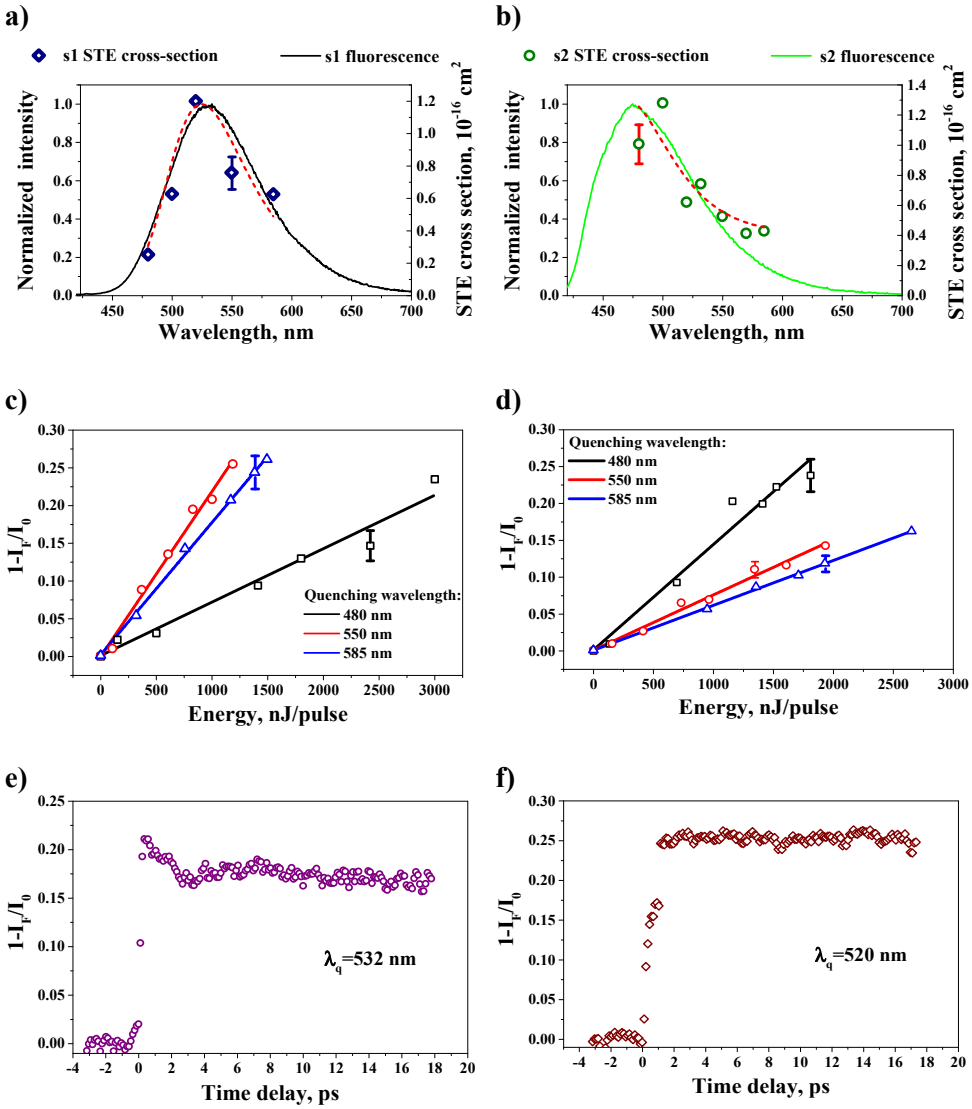

Figure 2.7. *Steady-state and time-resolved stimulated emission depletion of* ***s1*** *(a, c, e) and* ***s2*** *(b, d, f) in ACN. Top panels (a, b) show stimulated emission cross-section spectral dependencies overlapped with fluorescence bands. Middle panels (c, d) show quenching degree* $1 - I_q/I_F = f(E_q)$ *dependencies on the quenching pulse energy* E_q*. Bottom panels (e, f) show time-resolved traces of* $1 - I_q/I_F$ *quenching wavelength 532 nm (e) and 520 nm (f).*

$\sigma_{01}^{max} \approx 1.7 \cdot 10^{-16}$ cm^2 and $\approx 3 \cdot 10^{-16}$ cm^2, respectively. This may be due to the variation of the shape of excited state potential state energy due to the polar solvent relaxation processes. Estimated values of STE cross-sections agree with typical vales for organic dyes, which are in the of 10^{-17}-10^{-16} cm^2 range.[21]-[25]

Time dependencies of $1 - I_q/I_F = f(t)$ for quenching wavelengths λ_q=532 nm and λ_q=520 nm are presented in Figure 2.7 (e, f). The time evolution of quenching degree $1 - I_q/I_F$ of **s1** at λ_q=532 nm reflects the same fast solvent relaxation process observed in pump-probe measurements followed by the slow decay according to the fluorescence lifetime. The quenching degree of **s2** also agrees with results of pump-probe measurements. The signal rises within the instrumental response time and is followed by slow nanosecond decay.

The studies of STE cross-section are important due to the growing popularity of STED microscopy and related techniques. Measurement of STE cross-section of commonly used fluorescent dyes are required to develop structure-properties relations and to understand environmental effects on the value and spectral behavior of $\sigma_{10}(\lambda)$. This information together with probe brightness and photostability can be used for developing new dyes for photonic applications.

2.6 Light amplification properties

Transient absorption spectra of **s1** and **s2** in polar ACN showe negative signals ($\Delta D<0$) within the fluorescence band pointing to the signal amplification due to the stimulated emission. To exploit this property we studied the emission spectra of **s1** and **s2** under strong femtosecond pumping in order to check the possibility of obtaining amplified spontaneous emission. Although the **s1** and **s2** photostability are lower in ACN than in other solvents, we have not observed any decay in emission intensity under the most intense pumping in the measurement time, suggesting negligible dye bleaching within the experimental time frame.

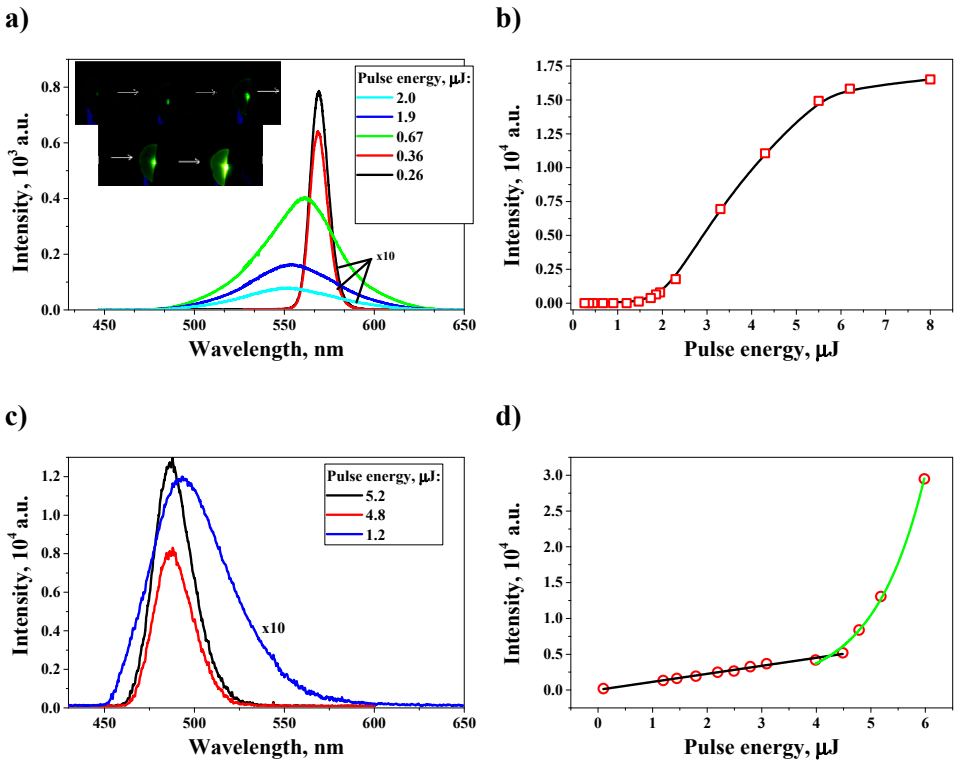

Figure 2.8. *Spontaneous emission and ASE (a, c) and maximum emission intensity and emission FWHM dependencies on the pulse energy (b, d) of* ***s1*** *(a, b) and* ***s2*** *(c, d) in ACN. Inset in a) shows photographs of emission of* ***s1*** *focused on a sheet of paper under pumping with increasing pulse energy.*

The emission spectra of the dyes under excitation by ultrashort pulses of different energy are displayed in Figure 2.8 that also shows the integrated emission intensity (right panels). Measurements are done in highly concentrated solutions (~mM). For this reason the fluorescence contour observed for low energy pumping is partly reabsorbed and therefore appears red-shifted compared to the emission spectra measured in dilute solutions. With the increase of pumping pulse energy the emission spectrum narrows reaching a FWHM down to ~10 nm for **s1** and ~20 nm for **s2**. The dependence of the intensity measured on the maximum on the pulse energy exhibits linear growth following by a fast

exponential rise (Figure 2.8 (b, d)). As it can be seen from Figure 2.8 the amplification threshold is ~1.5 and ~3 μJ/pulse for **s1** and **s2,** respectively. **s2** dye showes less effective ASE to **s1**. The light amplification is determined by the gain, which depends on STE cross-section and reabsorption, which is much higher in **s2** due to the smaller Stokes shift. This may result in less effective ASE in **s2**. The observed spectral narrowing, fast nonlinear growth of intensity with increasing pumping power and threshold character are indicative of ASE.

The light amplification due to ASE can also be observed by an eye: after the optical pumping reaches a threshold, a very bright and directed emission perpendicular to the direction of pumping beam appears (see inset in Figure 2.8). Observed minimum FWHM and ASE threshold energies are comparable with those of laser dyes in a nondispersive resonator.[43]-[47]

The maximum intensity dependence on the pumping pulse energy for **s1** reaches saturation starting from ~6 μJ/pulse. The saturation of detected intensity is occurring due to thermooptical effect caused by tightly focused strong laser beam. This increases the divergence of ASE that, as a result, can not be efficiently collected and misses the detector. The saturation of ASE of **s2** dye was not observed under maximum available pumping power (pulse repetition rate 1 kHz, E_p =6 μJ/pulse)

2.7 Two-photon excited anisotropy

The anisotropy of fluorescence excited upon two-photon absorption r_{2PA} offers important information on the relative orientation of transition dipole moments, also among excited states, and can shed light on the nature of excited states. Photoselection results in a broader dynamic range of r_{2PA}, with respect to the linear anisotropy, and two-photon anisotropy is used in polarization-resolved two-photon microscopy (see, for example, Ref.[48],[49]).

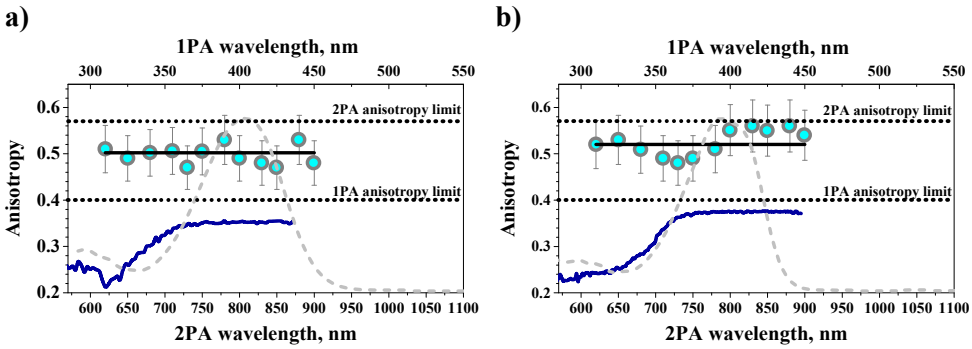

Figure 2.9. *Normalized 1PA (grey dashed line), one-photon excited (blue line) and two-photon excited (circles) fluorescence anisotropy of **s1** (a) and **s2** (b). Black dotted lines show 1PA anisotropy and 2PA anisotropy limits for linear molecules.*

The experimental r_{2PA} spectra for **s1** and **s2** in pTHF are presented in Figure 2.9. They were measured in the 620-900 nm range covering at least two electronic transitions. In spite of that, for both compounds the r_{2PA} spectra are featureless and close the the maximum theoretical value for two-photon fluorescence anisotropy r_{2PA} =0.57. This puzzling result is similar to what was observed in numerous studies of quadrupolar dyes (see Ref.[50],[51] and references therein), but contrasts sharply with the standard theory of two-photon anisotropy, that, at least for the symmetric **s2** dye would predict distinctively different r_{2PA} values in the $S_0 \rightarrow S_1$ and $S_0 \rightarrow S_2$ regions. This puzzling result will be addressed in the next sections, where we will discuss essential-state models for **s1** and **s2**.

2.8 Essential state models for symmetric and asymmetric quadrupolar dyes. Theoretical basis

Previous sections collect an extensive set of experimental data for two fluorene derivatives. Here we present a theoretical model for the optical

properties of the two dyes using the essential-state models (ESM). The parameters of the model were estimated using linear absorption and fluorescence and then the model was used to calculate one- and two-photon excited fluorescence anisotropy spectra and two-photon absorption spectra. The model provides a valuable insight into the problem of the two-photon excited fluorescence anisotropy of symmetrical quadrupolar dyes. Theoretical calculations reveal the role of symmetry lowering as due to polar solvation in the r_{2PA} spectra.

Essential-state models represent a powerful class of semi-empirical models for organic dyes. They are rooted in the work of Mulliken,[52] where the optical spectra of donor-acceptor ($D-A$) complexes were described using two states and a new class of intense absorption spectra due to the charge transfer from D to A was predicted. The model was first applied to describe π-conjugated dyes with a D and an A groups ($D-A$ or push-pull dyes) also accounting for electron-vibration coupling[53] and later extended to account for polar solvation as well.[54] In the years ESM developed to a detailed description of linear and non-linear spectral properties of different families of dyes (squaraines, fluorenes, cyanines) as well as of aggregates.[54]-[58] Here we shortly describe the principles of ESM applied for quadrupolar dyes ($D-A-D$ or $A-D-A$) and then we build the model to describe optical spectra of fluorene derivatives **s1** and **s2**.

The basis electronic states in ESM correspond to the main resonating structures of the system at hand. For quadrupolar dyes, three basis (diabatic) states are needed, a neutral state, $|N\rangle = DAD$, and two zwitterionic states, $|Z_L\rangle = D^+A^-D$ and $|Z_R\rangle = DA^-D^+$. In symmetric quadrupolar molecules the zwitterionic states Z_L and Z_R states are degenerate and located at energy 2η from the neutral state (see Figure 2.10). The mixing between the state N and either of zwitterionic states is described by the off-diagonal mixing element $-\tau$ in Hamiltonian, while mixing between Z_L and Z_R is neglected, $\langle Z_R|H|Z_L\rangle = 0$.

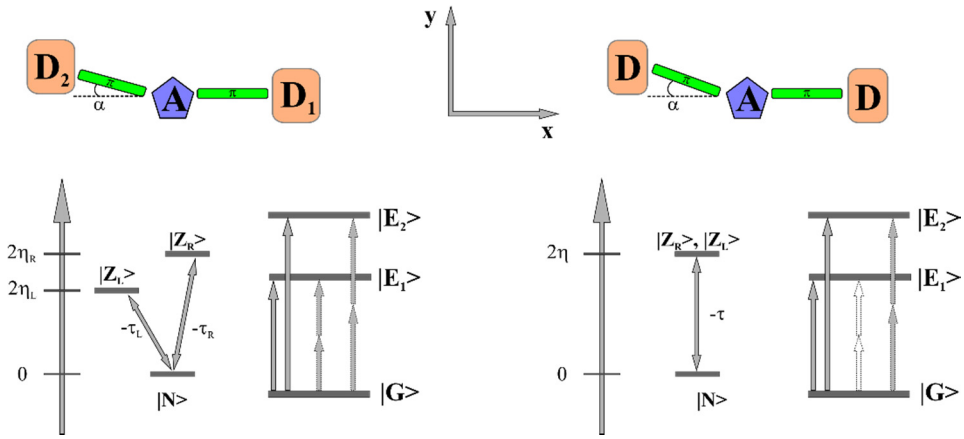

Figure 2.10. *Top: the schematic structure of an asymmetric (left) and a symmetric (right) quadrupolar dye. Bottom: a schematics of the three-state model for the same structures.*

On this basis the Hamiltonian reads:

$$H_{el} = \begin{pmatrix} 0 & -\tau & -\tau \\ -\tau & 2\eta & 0 \\ -\tau & 0 & 2\eta \end{pmatrix} \tag{2.3}$$

Accounting for symmetry, we introduced the symmetric $|Z_+\rangle = 1/\sqrt{2}\,(Z_L + Z_R)$ and antisymmetric $|Z_-\rangle = 1/\sqrt{2}\,(Z_L - Z_R)$ states. Only the symmetric Z_- state is mixed to N, so that the three adiabatic states that diagonalize the electronic Hamiltonian are:

$$|G\rangle = \sqrt{1-\rho}|N\rangle + \sqrt{\rho}|Z_+\rangle$$
$$|E_1\rangle = |Z_-\rangle$$
$$|E_2\rangle = \sqrt{\rho}|N\rangle + \sqrt{1-\rho}|Z_+\rangle$$

here ρ measures the weight of Z_+ in the ground state and therefore defines the charge distribution of the symmetric quadrupolar molecule in the ground state: $D^{+0.5\rho}A^{-\rho}D^{+0.5\rho}$.

To address spectral properties we must define the dipole moment operator. Following Mulliken[52] we neglect all matrix element of the dipole moment operator on the diabatic basis but μ_0, measuring the amplitude of the dipole moment in the two zwitterionic states, Z_L and Z_R. The two dipole moments of course point along the two $D-A$ arms of the molecule so that two components of the relevant dipole moment operator are defined in the $|N\rangle, |Z_L\rangle, |Z_R\rangle$ basis:

$$\hat{\mu}_x = \mu_0 \begin{pmatrix} 0 & 0 & 0 \\ 0 & 1 & 0 \\ 0 & 0 & -cos\alpha \end{pmatrix}$$

$$\hat{\mu}_y = \mu_0 \begin{pmatrix} 0 & 0 & 0 \\ 0 & 0 & 0 \\ 0 & 0 & sin\alpha \end{pmatrix}$$

The transition energies and transition dipole moments can be expressed through ρ and τ as follows:

$$\begin{aligned} h\omega_{GE_1} &= \sqrt{2}\tau\sqrt{(1-\rho)/\rho} \\ h\omega_{GE_2} &= \sqrt{2}\tau\sqrt{1/\big(\rho(1-\rho)\big)} \end{aligned} \qquad (2.4)$$

In asymmetric chromophores the zwitterionic states $|Z_L\rangle = D_1^+A^-D_2$ and $|Z_L\rangle = D_1A^-D_2^+$ are not degenerate and have different energies η_L and η_R respectively (see Figure 2.10). Therefore two mixing elements $-\tau_L = \langle Z_L|H|N\rangle$ and $-\tau_R = \langle Z_R|H|N\rangle$ enter the Hamiltonian, which acquires the following form:

$$H_{el} = \begin{pmatrix} 0 & -\tau_L & -\tau_R \\ -\tau_L & 2\eta_L & 0 \\ -\tau_R & 0 & 2\eta_R \end{pmatrix} \quad (2.5)$$

here the absence of symmetry allows for the mixing of symmetric and antisymmetric states.

To properly address all features of optical spectra it is important to account for the coupling of electronic degrees of freedom to molecular vibrations. For quadrupolar molecules two effective coordinates q_1 and q_2 are introduced on each of molecular arm $D_1 - A$ and $D_2 - A$. The two modes are equivalent in symmetric dyes and have the same frequency ω, while they can have different frequencies $\omega_{L/R}$ in asymmetric dyes. The vibrational Hamiltonian is:

$$H_{vibr} = -\sqrt{2\varepsilon_L}\,\omega_L \hat{q}_L \hat{\rho}_L - \sqrt{2\varepsilon_R}\omega_R \hat{q}_R \hat{\rho}_R + 1/2\,(\omega_L^2\,\hat{q}_L^2 + \omega_R^2 \hat{q}_R^2 + \hat{p}_L^2 + \hat{p}_R^2)$$

where $\hat{q}_{L/R}$ and $\hat{p}_{L/R}$ are the position and momentum operators of the harmonic oscillator, while $\varepsilon_{L/R}$ are the vibrational relaxation energies corresponding to different molecular arms. We solve the total Hamiltonian $H_{el} + H_{vibr}$ by writing the relevant matrix on the non-adiabatic basis generated as the direct product of the electronic basis times the eigenstates of the two harmonic oscillators related to $\hat{q}_L$ and $\hat{q}_R$. Of course, we truncate the vibrational basis to a maximum number M of states for each oscillator, so that the basis has dimension $3M^2$, making sure to use large enough M as to reach convergence. The diagonalization of the Hamiltonian matrix gives numerically exact vibronic eigenstates that enter the calculation of optical spectra, using sum over states expressions.[53],[54] An additional parameter γ enter the calculation that measures the linewidth associated with each vibronic line.

Polar solvation also affects spectral properties and is introduced in the model in the framework of the reaction field model.[54] In this approach that does not include any specific interactions with solvent such as hydrogen bonding, electron\proton transfer, etc, the chromophore is considered as a point dipole in a cavity inside the solvent, modeled as a continuous polarizable medium. The molecule with ground state dipole moment μ_G induces a reaction electric field F_R, proportional to the dipole moment:[10]

$$F_R = r\mu_G$$

The reaction field has two contributions: a first contribution from the fast motion of solvent electrons (electronic polarization) and a second contribution, only present in polar solvents, due to the slow rotation of the solvent molecules (orientational polarization) around the solute. The electronic polarization contribution is considered instantaneous and depends on the refractive index of the solvent, therefore in the model it is accounted by a renormalization of the corresponding matrix elements, which now acquire dependence on the solvent refractive index.[54] The contribution to polarizability due to the orientational polarization is much slower than relevant degrees of freedom of the solute and can therefore be treated in the adiabatic approximation. The relevant Hamiltonian reads:[54]

$$H_{solv} = -F_{or}\hat{\mu} + \frac{F_{or}^2}{2r_{or}}$$

The solvation relaxation energy $\varepsilon_{or} = r_0\mu_0^2/2$ is the energy gained by a molecule upon relaxation along the solvation coordinate. It enters the model as a parameter to reproduce the solvent polarity, taking values close to zero in non-polar solvent (hexane, cyclohexane) and increasing in polar solvents.

Because of the $-F_{or}\hat{\mu}$ term in the above equation, the electronic Hamiltonian acquires a dependence of the reaction field, or more precisely for bend quadrupolar dyes, on its two x and y components F_x and F_y. In the adiabatic approximation, the electronic Hamiltonian is then diagonalized on a grid of F_x and F_y values, and relevant optical spectra are calculated on each point of the grid. The total spectra are finally obtained summing up the spectra calculated on each point of the grid, weighted by the relevant Boltzmann distribution.[36],[55] Of course, when dealing with absorption spectra, the Boltzmann distribution is calculated based on the energy of the ground state, while, when interested in the fluorescence spectra, the Boltzmann distribution is calculated based on the energy of the fluorescent state. Along these lines, the model accounts not just for solvatochromism, but also for the subtle effects of polar solvation on band shape and specifically for inhomogeneous broadening effects. Finally, in the calculation of anisotropy spectra both distribution must be considered.

2.9 Modeling linear and nonlinear optical spectra

The set of molecular parameters used for essential states modeling of optical properties of **s1** and **s2** dyes is presented in Table 2. We notice that, while two different values for the vibrational frequency ω_L and ω_R could be in principle introduced for the asymmetric dye, we assume the same frequency ω for both. Table 2 collects all molecular parameters entering the calculation of optical spectra, including absorbance, emission, 2PA and linear and two-photon induced fluorescence anisotropy. These parameters are kept fixed, irrespective of the solvent, and the spectral evolution with solvent polarity is fully accounted for adjusting the single parameter ε_{or}, measuring the solvent relaxation energy. We emphasize that bandshapes are not adjusted by hand but are reproduced due to the inhomogeneous broadening and vibrational coupling effects that are included

Table 2. ESM parameters for **s1** and **s2.**

Dye	η_L, eV	η_R, eV	t_L, eV	t_R, eV	ε_L, eV	ε_R, eV	ω, eV	μ_L, D	μ_R, D	α, degrees	Γ, eV
s1	1.2	1.7	1.1	0.8	0.45	0.55	0.17	20	14	10	0.08
s2	1.42		0.8		0.48		0.18	29		20	0.08

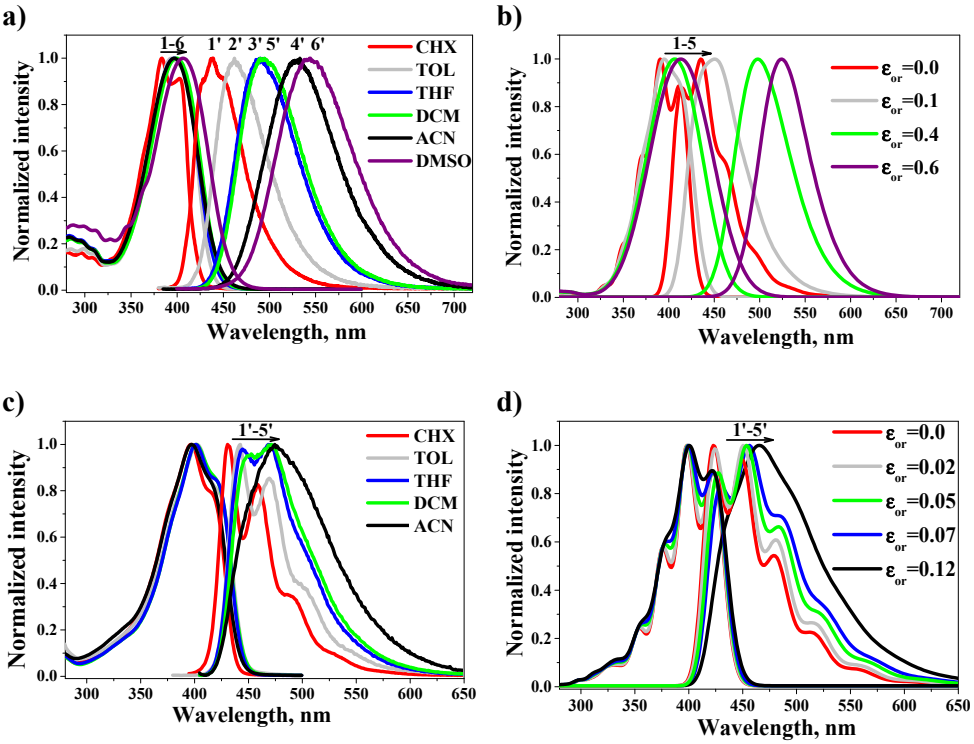

Figure 2.11 *Experimental (a, c) and calculated (b, d) one-photon absorption and emission spectra of* ***s1*** *(a, b) and* ***s2*** *(c, d). The solvent relaxation energy in the legend is set to mimic, in the increasing order of polarity, the corresponding solvents.*

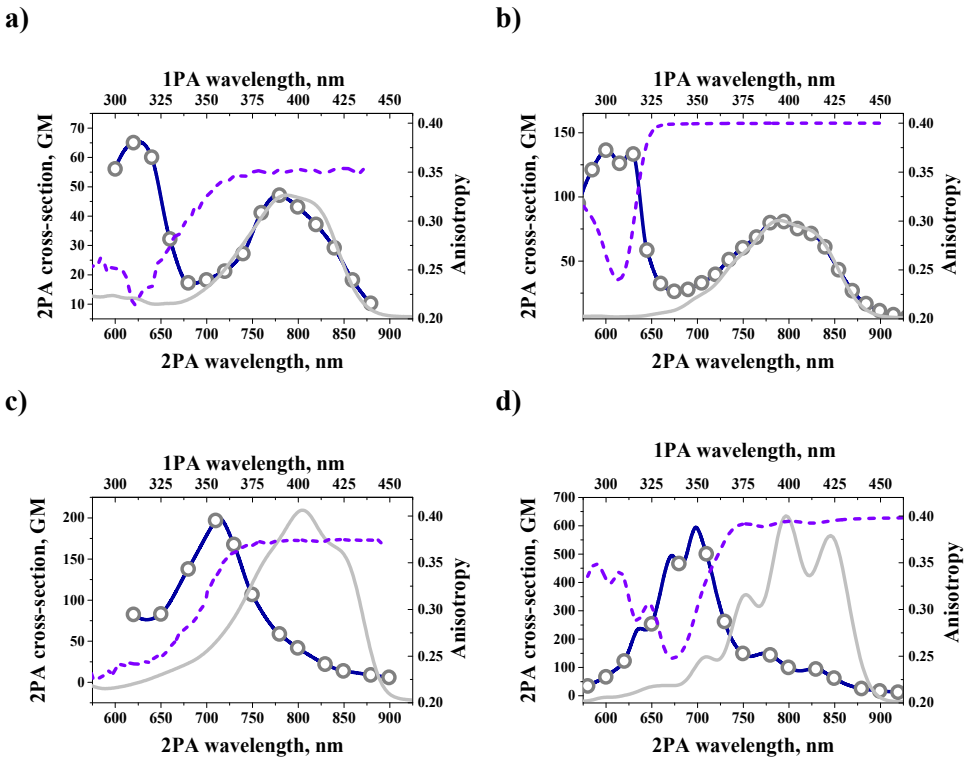

Figure 2.12 *Experimental (a, c) and calculated (b, d) 1PA (solid grey lines), 2PA (violet line plus circles) and one-photon excited fluorescence anisotropy (dashed blue lines) spectra of* ***s1*** *(a, b) and* ***s2*** *(c, d). 1PA and 2PA spectra measured in TOL, anisotropy spectra recorded in pTHF.*

in the ESM. The angle α (see Figure 2.10) in **s1** and **s2** was set to a small value to account for the molecular bending and to simulate one-photon anisotropy, however the small variation of α had no effect on other optical spectra.

Calculated absorption and emission spectra are compared with corresponding experimental spectra in Figure 2.11. The agreement is very good. ESM accurately reproduces the bandshapes and positions of absorption and fluorescence in the solvents of different polarity, with well-resolved vibronic structure observed in non-polar solvents that blurs in polar solvents.

Figure 2.12 addresses 2PA and one-photon excited fluorescence anisotropy spectra: again the comparison with experiment is very good. Fluorescence anisotropy is calculated as discussed in Ref.[56],[57] Specifically, to reproduce experimental results in pTHF, we assume a liquid solvent, i.e. we assume that after excitation the solute has not time to reorient before emitting a photon, but the solvent readjusts relaxing in response to the charge distribution in the photoexcited solute. Calculated spectra agree very well with the experimental data. A quite impressive result, particularly for **s2** while symmetric structure would suggest an anisotropy dip with r=-0.2 in the location of the $G \rightarrow E_2$ transition, while in that region the anisotropy attains positive 0.23-0.25 values. We can safely ascribe this result to the inhomogeneous broadening effects due to polar solvation and, partly, to the role of electron-vibration coupling. As for 2PA spectra we notice that the bending angle in **s2** is not large enough to effectively break the selection rule for symmetric dyes stating that $G \rightarrow E_1$ is one-photon active but silent in 2PA, while the opposite holds true for $G \rightarrow E_2$ transition. The ESM nicely reproduces the shape of 2PA spectra of **s1** and **s2**, also the intensity ratio of 0.6 calculated between peaks in the 2PA spectra of **s1** fluorene derivative agrees with the experimental value of 0.7.

2.10 Theory of two-photon excited anisotropy

The experimental data of two-photon excited anisotropy r_{2PA} of **s1** and **s2** were presented above in section 2.7. Despite of numerous reports on r_{2PA} of various molecules (either fundamental studies[50],[51],[59]-[65] or practical applications[48],[49],[66]) the theoretical description and explanation of the spectral behavior of $r_{2PA}(\lambda)$ is limited to a single report.[50] However, for symmetrical quadrupolar dyes the proposed three-state model[50] predicts different values of r_{2PA} for the different electronic transitions. This discrepancy was ascribed to some ground-state symmetry breaking leading to deviations of the transition dipole moments from expected directions. However, a quantitative

understanding of the phenomenon is missing, we therefore undertook a detailed analysis of two-photon induced anisotropies to extend ESM calculations to these elusive quantities.

2PA cross-section δ depends on transition dipole moments $\boldsymbol{\mu}_{oi}$, $\boldsymbol{\mu}_{if}$ of all states involved in the process: initial state o, final state f and intermediate state i:[61]

$$\delta \sim g(\nu_\lambda + \nu_\kappa)\left[\sum_i \left(\frac{(\boldsymbol{\lambda}\cdot\boldsymbol{\mu}_{oi})(\boldsymbol{\mu}_{if}\cdot\boldsymbol{\kappa})}{\varepsilon_i - \varepsilon_\lambda} + \frac{(\boldsymbol{\kappa}\cdot\boldsymbol{\mu}_{oi})(\boldsymbol{\mu}_{if}\cdot\boldsymbol{\lambda})}{\varepsilon_i - \varepsilon_\kappa}\right)\right]^2 \qquad (2.6)$$

where $g(\nu_\lambda + \nu_\kappa)$ is a normalized line shape function, ε_i is the energy of the intermediate state, $\varepsilon_\lambda, \varepsilon_\kappa$ are the energies of incident photons and $\boldsymbol{\lambda}$ and $\boldsymbol{\kappa}$ are their polarization vectors in the laboratory coordinate frame. $\boldsymbol{\lambda}$ and $\boldsymbol{\kappa}$ are unit-length vectors that are real for linearly polarized light and complex for circular polarization. The sum in (2.6) is generally referred as two-photon absorption tensor $\boldsymbol{S}_{of}$:[61]

$$\boldsymbol{S}_{of} = \sum_i \left(\frac{(\boldsymbol{\lambda}\cdot\boldsymbol{\mu}_{oi})(\boldsymbol{\mu}_{if}\cdot\boldsymbol{\kappa})}{\varepsilon_i - \varepsilon_\lambda} + \frac{(\boldsymbol{\kappa}\cdot\boldsymbol{\mu}_{oi})(\boldsymbol{\mu}_{if}\cdot\boldsymbol{\lambda})}{\varepsilon_i - \varepsilon_\kappa}\right) \qquad (2.7)$$

For 2PA measurements in solutions the tensor $\boldsymbol{S}_{of}$ must be averaged over all possible orientations. Orientation averaged $\langle\delta\rangle$ is a function of three parameters depending on the polarizations of the incident photons:[61]

$$\langle\delta\rangle = \delta_F F + \delta_G G + \delta_H H \qquad (2.8)$$

where $\delta_F = \sum_{a,b} S_{aa} S_{bb}$, $\delta_G = \sum_{a,b} S_{ab} S_{ab}^*$ and $\delta_H = \sum_{a,b} S_{ba} S_{ba}^*$ are molecular absorptivity parameters, and

$$F = 4(\boldsymbol{\lambda}\cdot\boldsymbol{\kappa})^2 - 1 - (\boldsymbol{\lambda}\cdot\boldsymbol{\kappa}^*)^2$$
$$G = -(\boldsymbol{\lambda}\cdot\boldsymbol{\kappa})^2 + 4 - (\boldsymbol{\lambda}\cdot\boldsymbol{\kappa}^*)^2 \quad (2.9)$$
$$H = -(\boldsymbol{\lambda}\cdot\boldsymbol{\kappa})^2 - 1 + 4(\boldsymbol{\lambda}\cdot\boldsymbol{\kappa}^*)^2$$

are three independent direction in an abstract experimental space defined by the different combinations of $\boldsymbol{\lambda}$ and $\boldsymbol{\kappa}$ vectors orientations.

The intensity I of two-photon excited fluorescence in solution is proportional to the averaged two-photon absorption tensor and mutual orientation of polarizations of emitted photon $\boldsymbol{\chi}$, fluorescence emission vector $\boldsymbol{F}$ and polarization of absorbed photons $\boldsymbol{\lambda}$, $\boldsymbol{\kappa}$:[65]

$$I = \langle \left|\boldsymbol{\lambda}\cdot\boldsymbol{\kappa}\cdot\boldsymbol{S}_{of}\right|^2 |\boldsymbol{\chi}\cdot\boldsymbol{F}|^2 \rangle \quad (2.10)$$

The averaging and complete analysis in the general case of different polarizations $\boldsymbol{\lambda}$, $\boldsymbol{\kappa}$ and $\boldsymbol{\chi}$ is rather cumbersome,[65] and requires 15×15 averaging matrix M_{ij}. Here we limit our attention to the practically important case of the degenerate 2PA followed by spontaneous emission. In that case, the two absorbed photons have equal polarization, i.e. $\boldsymbol{\lambda} \equiv \boldsymbol{\kappa}$ and therefore $\boldsymbol{\lambda}\cdot\boldsymbol{\kappa} = \boldsymbol{\lambda}\cdot\boldsymbol{\kappa}^* = 1$ and $F_a S_{bc} = F_a S_{cb}$. The averaging matrix M_{ij} is now 4×4 symmetric matrix and fluorescence intensity can be written as:[65],[63]

$$I = \sum_{i,j=1}^{4} P_i M_{ij} Q_j \quad (2.11)$$

where P_i depends on the polarization of excitation beam and emitted photon and Q_j depends of 2PA tensor $\boldsymbol{S}_{of}$ (see below). It is important to emphasize that the averaging of the Equation (2.10) is performed in the assumption of the absence of any molecular motion between the process of 2PA and fluorescence (viscous solvents).Parameters in Equation (2.11) are defined as follows:[65],[63]

$$\begin{aligned} P_1 &= 1 & Q_1 &= 1 \\ P_2 &= 1/2(|\boldsymbol{\lambda}\cdot\boldsymbol{\kappa}|^2 + |\boldsymbol{\lambda}\cdot\boldsymbol{\kappa}^*|^2) & Q_2 &= \frac{|\boldsymbol{F}\cdot\boldsymbol{S}|^2}{|\boldsymbol{F}|^2\delta_G} \\ P_3 &= |\boldsymbol{\kappa}\cdot\boldsymbol{\kappa}|^2 & Q_2 &= \frac{\delta_F}{\delta_G} \\ P_4 &= Re[(\boldsymbol{\lambda}\cdot\boldsymbol{\kappa})(\boldsymbol{\lambda}^*\cdot\boldsymbol{\kappa})(\boldsymbol{\kappa}^*\cdot\boldsymbol{\kappa})] & Q_2 &= \frac{(\boldsymbol{F}\cdot\boldsymbol{S}\cdot\boldsymbol{F})Tr\boldsymbol{S}}{|\boldsymbol{F}|^2\delta_G} \end{aligned} \quad (2.12)$$

These parameters define the dependence of the fluorescence intensity on the polarization of the incident photons. Now, using Equations (1.7) and (2.12) we can write the expressions for two-photon excited anisotropy. In case of linear polarization of the excitation beam $P_3 = 1$, P_2 and P_4 are equal to 1, if polarizer in detection channel is oriented vertically, or 0 for horizontal orientation. In these conditions the anisotropy is:[63]

$$r_{2PA} = \frac{-4 + 12Q_2 - 2Q_3 + 6Q_4}{14 + 7Q_3} \quad (2.13)$$

r_{2PA} depends on three parameters that for planar chromophores reduce to two:

$$r_{2PA} = \frac{18Q_2 + Q_3 - 7}{14 + 7Q_3} \quad (2.14)$$

2.11 Modeling two-photon excited anisotropy spectra

According to Equations (2.7), (2.9) and (2.12), the calculation of two-photon excited fluorescence anisotropy for different circular and linear polarizations requires the transition dipole moments and energies of the excited states. In Ref.[50] these parameters were partially estimated from the experimental data, partly calculated using density functional theory. Here we

exploit ESM to explicitly account for electron-vibration coupling and for solvation effects, leading to a quantitative analysis of the spectral results.

We start the discussion with purely electronic part of ESM to calculate r_{2PA} of symmetric and asymmetric quadrupolar dye and then demonstrate the effect of solvent and vibrational coupling. The electronic structure of the dyes in ESM is obtained by the diagonalization of relevant electronic Hamiltonian H_{el} (see Equations (2.3) and (2.5)). Knowing the eigenvalues (energies of the states) and eigenfunctions all necessary values entering the equations for r_{2PA} are obtained. For asymmetric quadrupolar dyes results depend strongly on the amount of asymmetry (defined by the relative energies of η_L and η_R and τ_L and τ_R) as well as on the bending angle α. ESM predicts high and constant value of r_{2PA} for the two electronic transitions $G \rightarrow E_1$ and $G \rightarrow E_2$, in agreement with that reported in Ref.[50] (see Figure 2.13 (a), calculations performed with the model parameters adopted for **s1** (see Table 2)). More interesting is the case of symmetric quadrupolar dyes, when symmetry imposes specific results irrespective of model parameters. Specifically, different values of r_{2PA} for $G \rightarrow E_1$ and $G \rightarrow E_2$ transitions are expected. Due to symmetry, for the $G \rightarrow E_1$ transition the 2PA tensor is 2×2 matrix with $S_{xx} = S_{yy}$. In this case[62] $Q_2 = 1/2, Q_3 = 2$ and $Q_4 = 1$ so that $r_{2PA} = 1/7 \approx 0.1428$. However experimental value for this transition is 0.52 (see Figure 2.14). In Ref.[50] this discrepancy was attributed to the symmetry-breaking effects resulting in asymmetrical charge distribution in the molecule. For pure electronic part of ESM that can be modeled by introducing a distortion parameter ϵ in Hamiltonian (2.3):

$$H_{el} = \begin{pmatrix} 0 & -\tau & -\tau \\ -\tau & 2\eta - \epsilon & 0 \\ -\tau & 0 & 2\eta \end{pmatrix} \qquad (2.15)$$

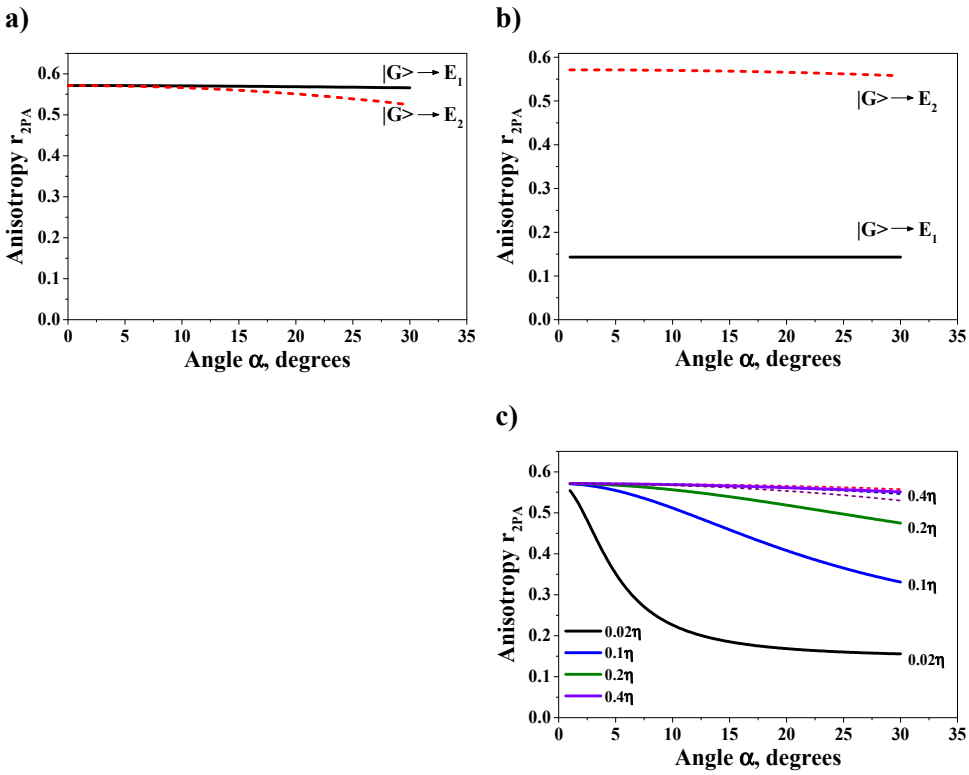

Figure 2.13 *Calculated r_{2PA} for $G \rightarrow E_2$ (dotted lines) and $G \rightarrow E_1$ (solid lines) transitions for asymmetrical quadrupolar dye (a) and undistorted (b) (using model parameters for **s2**) and distorted (c) symmetrical quadrupolar dye. Distortion parameter ϵ is measured in the units of η (see Equation (2.15)).*

The distortion means that the two molecular arms are not equal and charge is distributed asymmetrically. As seen in Figure 2.13 even small asymmetry significantly changes the value r_{2PA} for $G \rightarrow E_1$ transition. For $\epsilon = 0.1\eta$ and slightly bent ($\alpha \leq 10°$) molecules r_{2PA} for $G \rightarrow E_1$ transition almost equals r_{2PA} for $G \rightarrow E_2$. This case confirms assumptions made in Ref.[50] to explain the constant values of r_{2PA} of symmetrical molecules. High values of parameters ϵ lead to significantly asymmetrical charge distribution and therefore

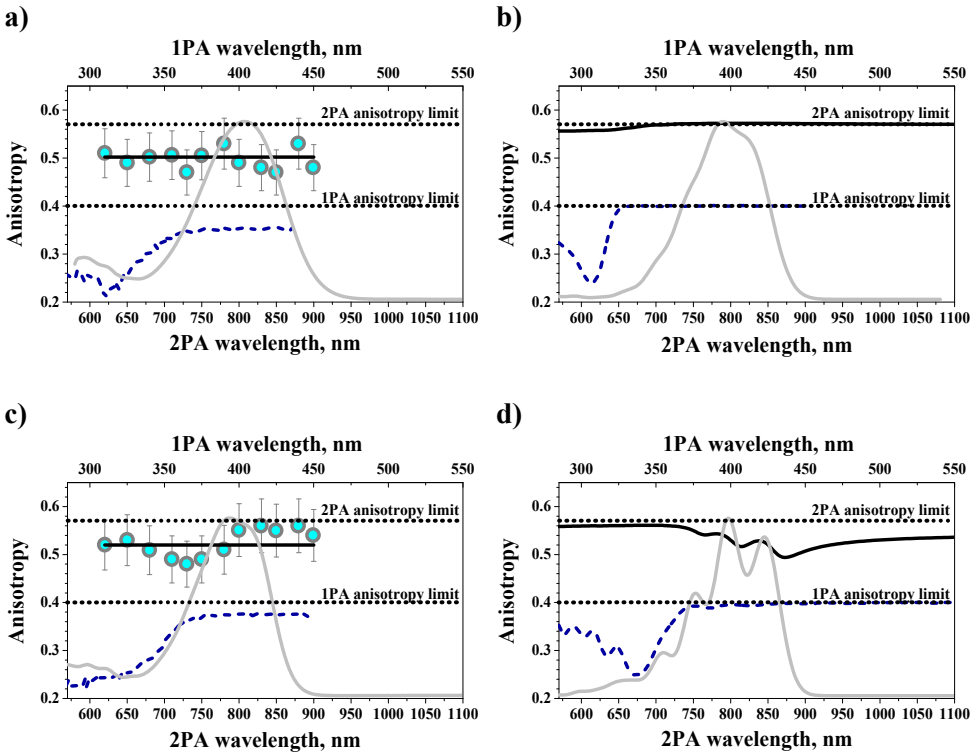

Figure 2.14 *Experimental (a, c) and calculated (b, d) 1PA (solid grey lines), one-photon (dashed blue lines) and two-photon (grey circles – experimental data, dashed black lines – modeling) excited fluorescence anisotropy spectra of* ***s1*** *(a, b) and* ***s2*** *(c, d). 1PA and 2PA spectra measured in TOL, anisotropy spectra recorded in pTHF.*

the anisotropies of both transitions become similar and equal that of asymmetrical quadrupolar dye.

Although the previous results are in agreement with previous reports we have to artificially introduce the distortion parameter ϵ in H_{el} to account for symmetry breaking. However, the full Hamiltonian includes electronic-vibrational coupling and solvation that are generally responsible for symmetry breaking. Two-photon excited fluorescence anisotropy was calculated for **s1** and **s2** using parameters listed in Table 2 for emission wavelength $\lambda_{em} = 450$ nm

and at 300 K. As shown in Figure 2.14 predicted values are in excellent agreement with the experimental data: for both dyes r_{2PA} is independent on the wavelength and approaching the limiting value. Here it is important to notice that nor additional parameters nor *ad hoc* assumptions must be introduced to calculate two-photon excited anisotropy, we are in fact using exactly the same models as described above to reproduce other spectral properties.

2.12 Fluorescent organic nanoparticles

Organic nanoparticles (ONPs) were prepared based on **s1** and **s2** dyes following the simple reprecipitation procedure, described in Ref.[67]. Briefly, a drop of 100 μL of 1 mM solution of **s1** or **s2** dyes in THF was rapidly injected in a vial with 9.9 mL of MilliQ water under vigorous stirring (Figure 2.15). As both dyes are hydrophobic, the abrupt replacement of THF with water induces dye aggregation. The solution immediately became yellowish, with no sign of precipitation. The mixture was left under stirring for 1 hour and then all measurements were performed. The obtained suspension is stable over days.

Results of dynamic light scattering (DLS) measurement of **s1**-based ONPs (**s1**$_{ONPs}$) and **s2**-based ONP (**s2**$_{ONPs}$) are shown in Figure 2.16. Both dyes form nanoparticles with monomodal and narrow-to-moderate size distribution, as demonstrated by the low values of polydispersity index (PDI), equal to 0.07 for **s2**$_{ONPs}$ and 0.15 for **s1**$_{ONPs}$. The average hydrodynamic diameters of synthesized ONPs were ≈160 nm and ≈80 nm for **s1**$_{ONPs}$ and **s2**$_{ONPs}$, respectively. Although the described preparation method does not allow a precise control of the growth parameters, the results of DLS PDI and average diameter measurements were reproducible within ±10%.

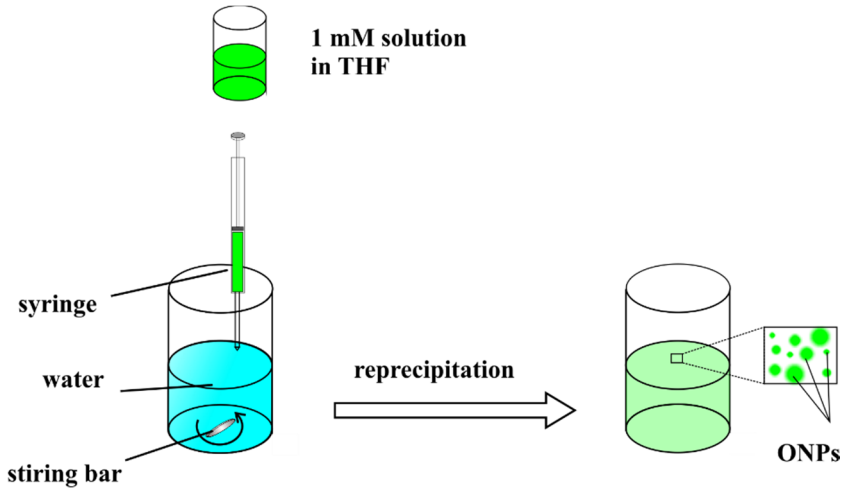

Figure 2.15 *Schematic of ONPs preparation procedure.*

Fluorescence and absorption spectra of **s1**$_{ONPs}$ and **s2**$_{ONPs}$ are plotted in Figure 2.17 and main photophysical properties are presented in Table 3. For ease of comparison the parameters of monomer dyes are also listed. For both **s1**$_{ONPs}$ and **s2**$_{ONPs}$ fluorescence excitation spectra overlap with the corresponding absorption profiles and are independent of the emission wavelength.

The absorption spectrum of **s1**$_{ONPs}$ in water is red-shifted compared to the absorption spectrum of **s1** in the most polar DMSO (see Figure 2.17 and Figure 2.2) while absorption maximum of **s2**$_{ONPs}$ remains at the same wavelength as for **s2** in organic solvents. Absorption bands of both suspensions are broad and the molar extinction coefficient is reduced by ≈70% for **s2**$_{ONPs}$ and by ≈50% for **s1**$_{ONPs}$ compared to the corresponding ε_{max} for **s1** and **s2** in THF. Fluorescence spectrum of **s1**$_{ONPs}$ peaks at 512 nm. With reference to the solvatochromic behavior of **s1** (see Table 1 and Figure 2.2) **s1**$_{ONPs}$ fluorescence is similar to that observed in medium-polarity environment. This suggests that fluorescence comes from dye nanoaggregates, and specifically from chromophores buried inside the nanoparticles that do not experience the polar environment due to water.

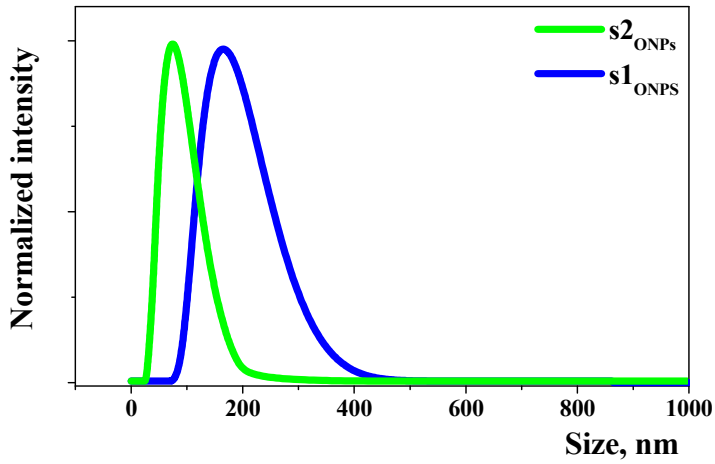

Figure 2.16 *The* ***s1****$_{ONPs}$ and* ***s2****$_{ONPs}$ intensity-weighted DLS size distribution.*

The emission of **s2**$_{ONPs}$ was almost completely quenched (fluorescence quantum yield was estimated to be <0.5%) and a flat and broad spectrum with maximum around 520 nm was detected. The fluorescence of **s1**$_{ONPs}$ also exhibited quenching, even if less marked than for **s2**$_{ONPs}$. The 10% fluorescence quantum yield measured for **s1**$_{ONPs}$ is large enough to make these nanoparticles of interest for further studies. Fluorescence quenching is commonly observed for dye aggregates and is known as aggregation-caused quenching.[68] The interactions of chromophores closely located within a nanoparticle result in fluorescence quenching and red-shift and broadening of absorption spectra. However a completely opposite effect can also be observed for some type of molecules and is called aggregation-induced emission leading to significant enhancement of fluorescence quantum yield.[69]

In contrast with simple monoexponential fluorescence decay kinetics of **s1** in organic solvents, the fluorescence of **s1**$_{ONPs}$ exhibits more complex biexponential decay (see Figure 2.17 and Table 3). That was also observed[70]-[72] for various ONP synthesized by reprecipitation. The fluorescence decay component with the longest lifetime is attributed to emission of chromophores located in the core of a nanoparticle, while interactions between dye molecules

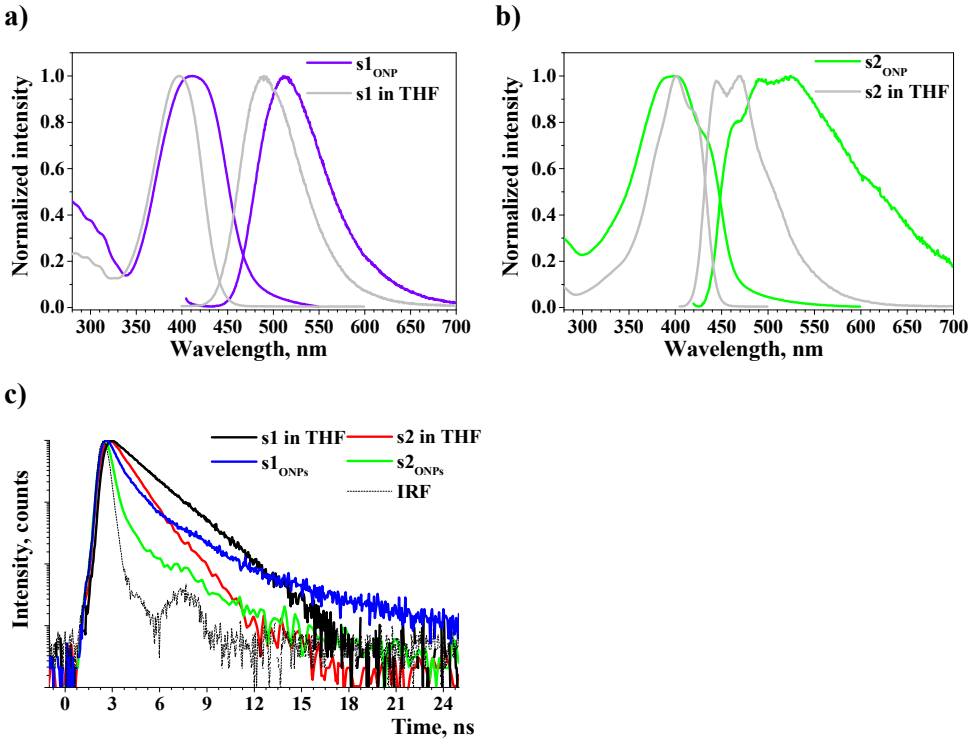

Figure 2.17 *Normalized absorption and fluorescence of* ***s1****$_{ONPs}$ (a, blue line) and* ***s2****$_{ONPs}$ (b, green line) in water and* ***s1*** *(a, grey line) and* ***s2*** *(b, grey line) in THF. c) Fluorescence decays of* ***s1*** *(black line) and* ***s2*** *in THF (red line),* ***s1****$_{ONPs}$ (blue line),* ***s2****$_{ONPs}$ (green line) and instrument response function (thin dashed line)*

located close to the ONP surface and hence interacting with water leads to fluorescence quenching and results in shorter fluorescence lifetime.

The photodecomposition quantum yield was determined for **s1**$_{ONPs}$ (see Table 3). The nanoparticles demonstrate similar photobleaching decay $D(\lambda, 0) - D(\lambda_{max}, t_{irr}) = f(t)$ as observed for solvated dye (see Figure 2.18). The value of Q_{ph} **s1**$_{ONPs}$ of was found to be $0.7 \cdot 10^{-4}$ what is only slightly higher compared to the photostability **s1** in organic solvents (except of ACN), although the photostability of organic dyes in water is typically much lower than in organic solvents and can be even 2 orders of magnitude worse. This effect may be

Table 3. Main photophysical and photochemical properties of **s1**$_{ONPs}$ and **s2**$_{ONPs}$. Absorption λ_{max}^{abs} and emission λ_{max}^{fl} wavelengths maxima; ε_{max} - the extinction coefficient at λ_{max}^{abs}; Q_{fl} - the fluorescence quantum yield; [a]τ_{fl} - the fluorescence lifetime and Q_{ph} - the photodecomposition quantum yield.

Compound	λ_{max}^{abs}, nm	λ_{max}^{fl}, nm	ε_{max}, 10^3 M^{-1} cm^{-1}	Q_{fl}, %	τ_{fl}, ns	Q_{ph}, 10^{-4}
s1$_{ONPs}$	413	512	33	10	0.7 (0.75) 3.8 (0.25) $\langle\tau\rangle$: 2.7	0.7
s2$_{ONPs}$	400	≈520	40	<0.1	<0.5	-
s1	383-407	439-545	44-53	80-96	1.4-2.4	0.09-10
s2	397-403	431-474	72-78	50-70	1.4-2	40-80

[a] in parenthesis are normalized amplitudes of corresponding fluorescence decay components. $\langle\tau\rangle$ is the average lifetime.

attributed to high polarity of water as well as to its strong hydrogen-donating and -accepting ability.[29],[73]

The low fluorescence quantum yield did not allow the determination of 2PA cross-section of **s2**$_{ONPs}$ using 2PF method, also the concentration of this suspension was too low for Z-scan. However the fluorescence of **s1**$_{ONPs}$ under two-photon excitation was detectable and allowed us to measure their 2PA cross-section in 620-900 nm spectral range. The intensity of up-converted emission of **s1**$_{ONPs}$ exhibited quadratic dependence on the excitation pulse energy at all wavelengths, what is expected for a two-photon absorption process (see example in Figure 2.19). Here we emphasize that the 2PA cross-section of ONPs was estimated using the formula (1.9) and the *nominal* dye concentration, i.e. 10^{-5} M.

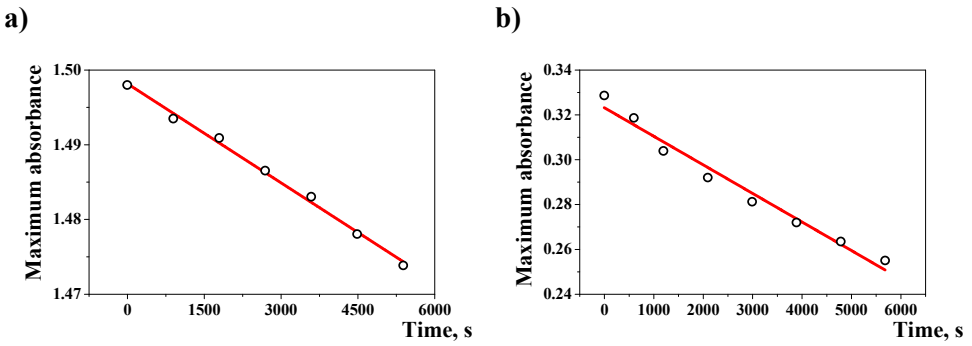

Figure 2.18 *Maximum absorption decay of* ***s1*** *in THF (a) and* ***s1***$_{ONPs}$ *in water under CW irradiation.* λ_{irr}*≈400 nm for* ***s1*** *and ≈410 nm for* ***s1***$_{ONP}$*, power density 5* $mW \cdot cm^{-2}$.

2PA spectra of **s1**$_{ONPs}$ suspension (see Figure 2.19) exhibit only one broad peak with maximum located near the half of the energy of the 1PA band. The shape of **s1**$_{ONPs}$ 2PA spectra changes compared to the monomeric **s1,** the most pronounced alteration being the complete quenching of the 2PA band observed at 620 nm for **s1** in toluene. Overall, the 2PA cross-section of suspension is reduced compared to the isolated **s1** molecule. The spectral shape alterations and 2PA cross-section reduction upon aggregation in water are commonly observed for ONPs synthesized from fluorescent dyes.[70]-[72] These effects are attributed to the negative cooperative effects of through-space inter-chromophoric interactions observed in dense packed nanoparticles.[58],[70],[71] As it was shown theoretically, the 2PA response of aggregates of quadrupolar dyes depends on the molecular orientation and the distance between chromophores, and can be either quenched or enhanced.[58] The amplification of the 2PA response is observed for J aggregates, if the dyes are aligned in an ordered array or for "ladder" geometry, i.e. face-to-face orientation with a lateral shift. In the case of ONPs synthesized with a reprecipitation method this self-alignment is highly unlikely and due to the various distributions of the intermolecular orientations and distances the 2PA cross-section is reduced.

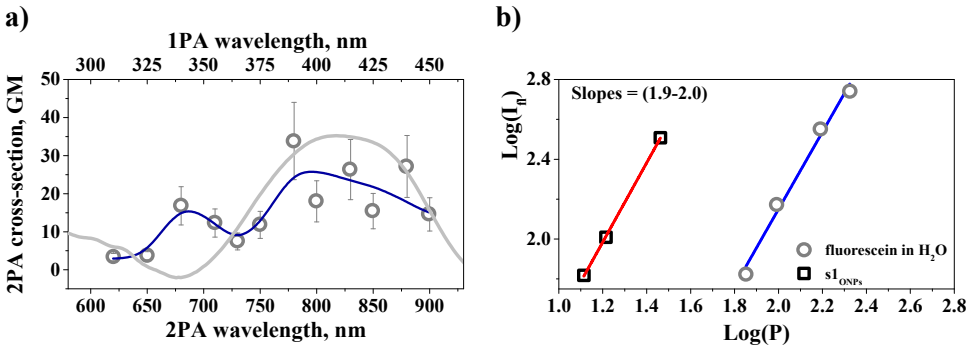

Figure 2.19 *(a) 2PA spectra (grey circles), 1PA (grey line) of* ***s1****$_{ONPs}$ in water. Blue line is to guide an eye. b) Logarithmic plots of dependence of emission intensity of* ***s1****$_{ONPs}$ (black squares) and fluorescein (gray circles) on the excitation power upon excitation at* λ_{exc}*=780 nm. Blue and red lines are linear fit.*

However, even though the 2PA response of **s1**$_{ONPs}$ is quenched, the large number of chromophores in one aggregate leads to the fact that 2PA cross-section of a single nanoparticle is several orders of magnitude higher compared to the monomeric dye. For example in Ref. [70],[71] the number of molecules per nanoparticle was estimated to be ≈10^4 leading to giant 2PA cross-section of a single ONP.

2.13 Conclusions

This chapter collects a comprehensive set of linear, nonlinear optical properties and photostability of symmetric and asymmetric quadrupolar fluorene derivatives. Both dyes are highly fluorescent, exhibit acceptable 2PA cross-section in the tuning range of Ti:Sapphire lasers and demonstrate efficient ASE in polar solvents. These properties make them appealing candidates for photonic applications, but the relatively low photostability of **s2** has to be taken into account. We estimated STE cross-section of two dyes in polar solvent and

showed that time-resolved STED experiment agreed well with the pump-probe data.

Experimental data were rationalized using essential-state model. We discuss in details the nature of 2PA bands and a particularly interesting case of two-photon anisotropy. The ESM model naturally accounts for symmetry lowering in symmetrical quadrupolar molecules, due to the solvation and vibronic coupling, predicting high and constant values of two-photon anisotropy in symmetrical quadrupolar dyes, in full accordance with the experiment.

The last section describes an attempt to solubilize hydrophobic fluorene derivatives using simple one-step reprecipitation method. Both dyes form ONPs with monomodal size distribution and hydrodynamic diameters of 160 nm (**s1**$_{ONPs}$) and ≈80 nm (**s2**$_{ONPs}$). The aggregation-induced fluorescence quenching significantly reduces fluorescence quantum yields of fluorene-based ONPs leading to almost complete elimination of the fluorescence of **s2**$_{ONPs}$. **s1**$_{ONPs}$ remained fluorescent and we were able to study their two-photon response using 2PF. Interestingly, the photostability of **s1**$_{ONPs}$ in water was comparable to the photostability of **s1** in organic solvents.

3 QUATSOMES: BIOCOMPATIBLE NANOCARRIERS OF FLUORESCENT DYES

In this chapter we discuss the different routes to create quatsomes-based organic nanoparticles. The motivation behind this work is to take advantage of the attractive properties of quatsomes (QS) to create stable fluorescent organic nanoparticles for photonics applications. Quatsomes are small (50-200 nm) unilamellar vesicles developed in Nanomol group (Barcelona).[74],[75] QS are synthesized by simple one-step method, called DELOS-SUSP[75] based on depressurization of a sterol (cholesterol, β-sitosterol) solution in CO_2-expanded ethanol into an aqueous solution containing a quaternary surfactant (hexadecyltrimethylammonium bromide (CTAB), myristalkonium chloride, cetylpyridinium chloride) (see Figure 3.1). QS are formed immediately after depressurization due to the self-organization of sterols. In current work we used QS synthesized from cholesterol and CTAB taken in equimolar ratio. It was shown[76] that the 1:1 ratio between cholesterol and surfactant gives pure vesicular phase, where bilayer is formed by synthons of CTAB and cholesterol molecules (Figure 3.1).

We have investigated various different strategies of creating fluorescent organic nanoparticles (FONs) based on QS. The first approach of decorating QS with dyes exploits the strong positive charge on the QS surface to electrostatically bind water-soluble anionic dye. The second approach implies including a hydrophobic dye inside the membrane, also allowing the solubilization of hydrophobic dyes. Finally, the third approach aimed to

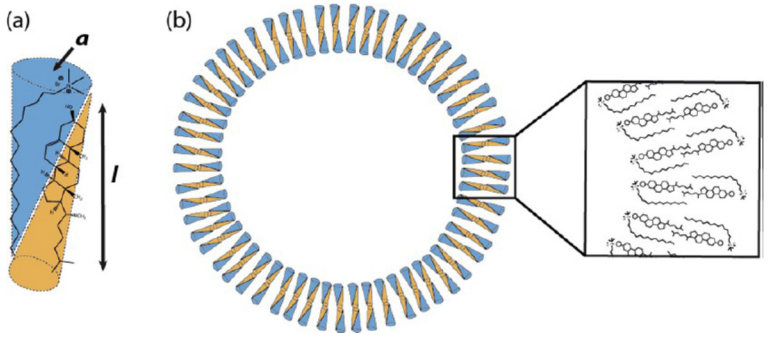

Figure 3.1 *A scheme illustrating the formation of (a) cholesterol/CTAB bimolecular synthon and their assembling into bilayer vesicles (b). Reprinted with permissions from Ref.[76] Copyright 2013 American Chemical Society*

substitute the cholesterol in the QS membrane with a modified cholesterol bearing an attached chromophore. Before optical measurements the colloidal stability and the morphology of all samples were checked to ensure that guest molecules do not significantly affect these properties. The QS synthesis and modifications, cryogenic transmission electron microscopy (Cryo-TEM) and colloidal characterization were performed in Institut de Ciència de Materials de Barcelona (ICMAB) by Antonio Ardizzone. Detailed description of synthetic route can be found in Ref.[75],[77]

3.1 Quatsomes labeled with fluorescein. Preparation, characterization and optical properties.

Since the QS membrane carries a positive charge, it can be decorated with anionic dyes via electrostatic interactions. This effect was studied[78]-[80] for micelles formed by cationic surfactant. However, the micelle formation occurs at relatively high surfactant concentration, above the critical micelle

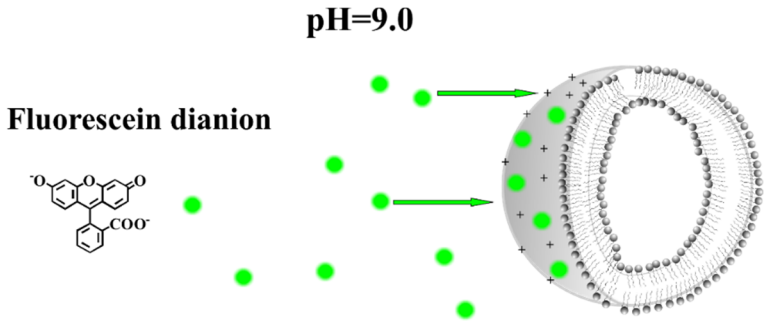

Figure 3.2 *Schematic illustrating the fluorescein dianion (green dots) interacting with positively charged quatsome membrane at basic pH.*

concentration, therefore it is not possible to work with diluted suspensions of nanoparticles. In other terms if the suspension is diluted below a critical concentration, the micelles do disrupt. The stability of QS upon dilution instead allows us to study dye-nanoparticle electrostatic interactions for different dye/QS ratios.

Fluorescein (Fl) dye exists in water solution in different forms,[9] depending on the medium acidity. Fl is in a cationic form at pH<2.2, in a neutral form at pH=2.2-4.4, in an anionic form at pH=4.4-6.7, finally in a dianionic form at pH>6.7. The scheme of interaction between QS and Fl dianion is sketched in Figure 3.2. Samples were prepared as follows: a fluorescein solution in MilliQ water was added to a QS suspension and then the pH was adjusted to 9.0 by dropwise addition of 0.01 M NaOH. We have prepared 7 different samples of fluorescein-decorated QS (Fl-QS), with different concentration of nanoparticles, while keeping the Fl concentration constant and equal to 10^{-6} M (see Table 4). The dye loading *L* was estimated as:

$$L = C_{dye}/(C_{CTAB} + C_{ch}) \qquad (3.1)$$

where C_{dye}, C_{CTAB} and C_{ch} are the concentrations of the dye, CTAB and cholesterol respectively. All samples were filtered in the centrifugal filters with

Table 4. Main photophysical parameters of Fl-QS samples: [a]L is the dye loading; [b]$C_{Fl}/(0.5 \cdot C_{CTAB})$ - the molar ratio between Fl and CTAB available for interaction; absorption λ_{max}^{abs} and emission λ_{max}^{fl} wavelengths maxima; Q_{fl} - the fluorescence quantum yield; [c]τ_{fl} – the fluorescence lifetime and Q_{ph} - the photodecomposition quantum yield.

Sample	L, 10^{-3}	$C_{Fl}/(0.5C_{CTAB})$ $\times 10^3$	λ_{max}^{abs}, nm	λ_{max}^{fl}, nm	Q_{fl}, %	τ_{fl}, ns	Q_{ph}, 10^{-5}
Fl-QS-1	0.1	0.4	501	521	93	4.2	1.3±0.5
Fl-QS-2	0.5	2	501	521	89	4.2	3±1
Fl-QS-3	1	4	501	521	78	4.2	2.2±0.6
Fl-QS-4	5	20	500	520	73	4.2	-
Fl-QS-5	10	40	500	520	-	0.7 (0.06) 3.9 (93)	-
Fl-QS-6	50	200	490	512	-	1.2 (33) 3.8 (67)	-
Fl-QS-7	170	670	490	512	-	4.06	-
[d]Fl	-	-	490	512	95	4.1	[e]8±2 [f]7±1

[a] dye loading calculated using Equation (3.1)

[b] $0.5 \cdot C_{CTAB}$ is the concentration of CTAB molecules available for interaction with Fl dianion. Since it is highly unlikely that the dye can penetrate through hydrophobic inner part of the bilayer it can interact only with half of CTAB molecules that form the outer surface of the membrane.

[c] in parenthesis are normalized amplitudes of corresponding fluorescence decay components.

[d] studied at pH=9.0 adjusted by NaOH

[e] value obtained with fluorescence method (see Equation (1.14))

[f] value obtained with absorption method (see Equation (1.15))

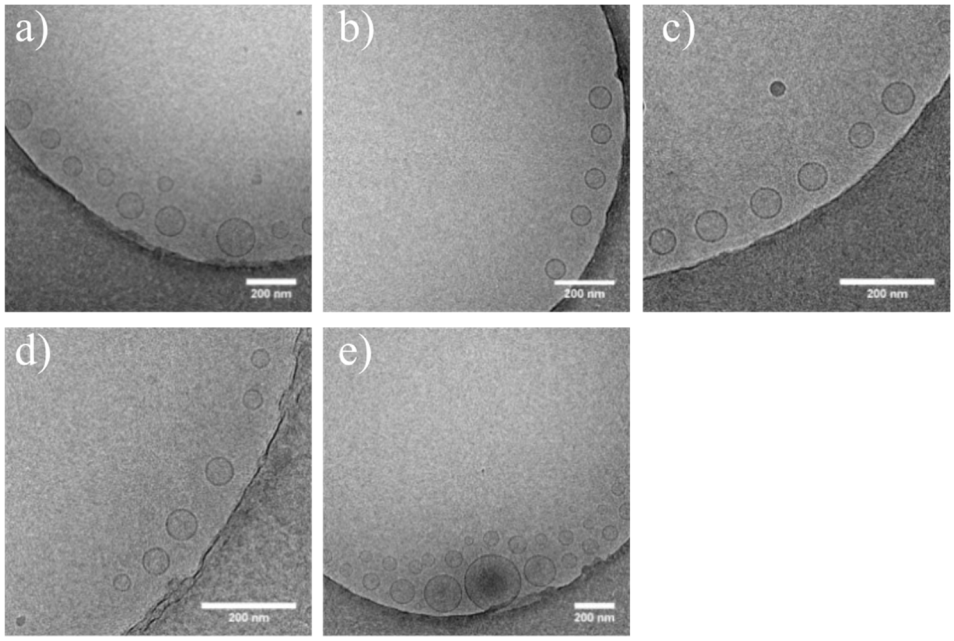

Figure 3.3 *CryoTEM images of Fl-QS-2 (a), Fl-QS-4 (b), Fl-QS-5 (c), Fl-QS-6 (d), Fl-QS-7 (e). Scale bar in all images equals 200 nm.*

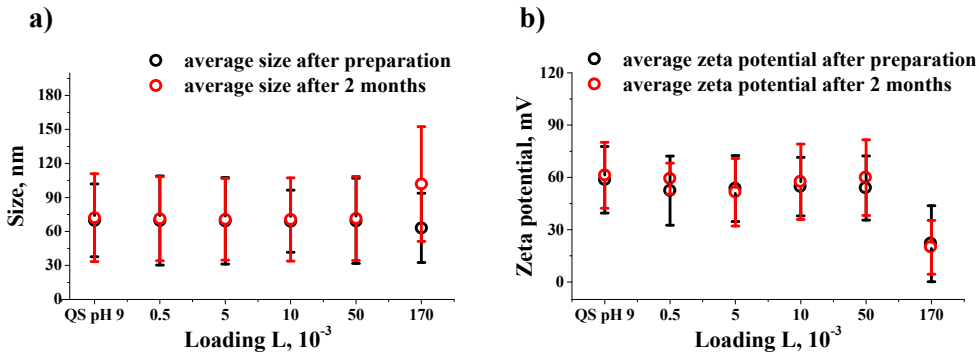

Figure 3.4 *Average size and zeta potential of QS-Fl with different loadings.*

molecular weight cutoff of 100 kDa to check the presence of free Fl molecules. Unbounded dye was actually found in the samples Fl-QS-5, Fl-QS-6 and Fl-QS-7.

The structure and stability of QS upon Fl addition was checked by Cryo-TEM (1 week after the synthesis) and monitored in time (1 week and 2 month after the synthesis) with DLS and zeta potential measurements. The great advantage of the Cryo-TEM microscopy is that the samples remain in water and do not need to be stained or fixed, so it gives a "snapshot" of nanoscale objects and allows to investigate their native features. The Cryo-TEM images of QS-Fl samples with different amount of Fl (see Figure 3.3) reveal round shaped nanoparticles 50-70 nm in diameter and no effect on the structure or morphology of QS with the increasing of dye loading was observed.

The same conclusion can be drawn from the results of hydrodynamic diameter and zeta potential measurements shown in Figure 3.4. The average DLS diameter of QS-Fl is ≈70 nm and independent of the dye loading. Zeta potential of QS-Fl samples for dye loading $L \leq 50 \cdot 10^{-3}$ is 50-60 mV and equals to that of free QS, while for QS-Fl-7 sample zeta potential value is lower. Therefore for low values of loading the attachment of dianionic dye does not affect the surface charge of QS, while at $L = 170 \cdot 10^{-3}$ it causes lowering of zeta potential.

The QS with $L \leq 50 \cdot 10^{-3}$ show excellent colloidal stability, with no significant changes observed within 2 months. As it can be seen from Figure 3.4 the hydrodynamic diameter and zeta potential remain stable within the error, although for Fl-QS-7 a slight increase in particles size and polydispersity was detected.

Figure 3.5 and Table 4 compare spectral properties of the fluorescein dianion with Fl-decorated QS. When the dye loading is small, i.e. the concentration of CTAB molecules is significantly higher that the concentration of Fl, the fluorescence and absorption spectra exhibit a red shift of ≈ 10 nm compared to free Fl (see Figure 3.5 and Table 4). This shift is accompanied with

a fluorescence intensity increase and with a decrease in absorption intensity, while the fluorescence decay remains monoexponential with the same fluorescence lifetime that for solvated fluorescein. Upon progressive addition of QS up to dye loading $L < 10 \cdot 10^{-3}$ the maximum absorption continuously decreases and no major changes in the fluorescence spectra are observed. For the sample Fl-QS-5 with dye loading $L = 10 \cdot 10^{-3}$ a pronounced drop in the fluorescence intensity and fluorescence lifetime was detected. Fl-QS-5 and Fl-QS-6 exhibit biexponential fluorescence decay with the shortest lifetime ≈1 ns and lifetime of the second component close to the lifetime of free Fl. For the samples with the highest tested dye loading $L > 10 \cdot 10^{-3}$, absorption and fluorescence spectra are very close to those of free fluorescein.

Fluorescein shows similar spectral behavior when attached to positively charged micelles and in presence of surfactants.[78],[79],[80] Fluorescence and absorption red shift is explained as result of stabilization of the excited state of the dye upon binding.[78] There is an equilibrium between the Fl attached to the QS membrane and free dye molecules. The equilibrium shifts to free Fl molecules as the loading increases. When CTAB molecules are in large excess, all Fl dyes are attached to QS resulting in the red shit of fluorescence and absorption spectra. Starting from loadings $L \geq 10 \cdot 10^{-3}$ significant amount of fluorescein remains unbound, indeed it was possible to detect it after filtration. A drop in fluorescence intensity and average lifetime of FL-QS-5 may be related to self-quenching of fluorescein due to the high local concentration. The decrease in the fluorescence quantum yield (measured only for the samples with negligible amount of free Fl) and the shortest component of biexponential fluorescence decay for Fl-QS-5 and Fl-QS-6 can be attributed to the same effect. For the sample with the highest loadings Fl-QS-6 and Fl-QS-7 fluorescence and absorption spectra are very close to the Fl spectra because the concentration of free dye significantly exceeds the concentration of bound dye. This interpretation is supported by excitation spectra. For Fl-QS-1 – Fl-QS-4

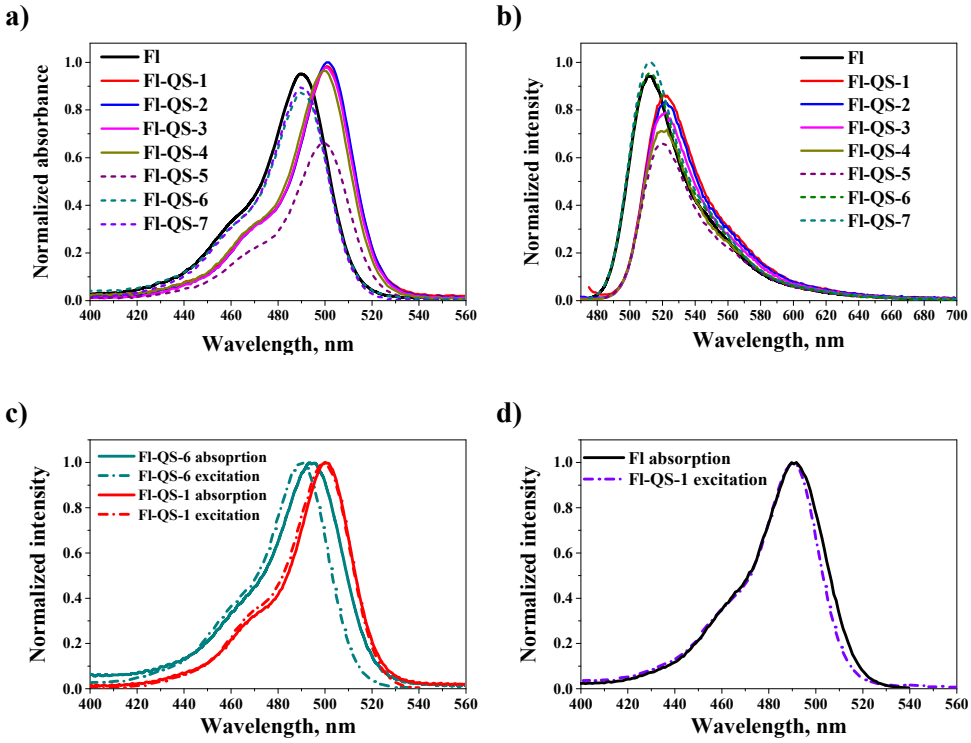

Figure 3.5 *Absorption (a, c, d), fluorescence (b) and excitation (c, d) spectra of Fl and QS-FL. The absorption spectra in (a) are normalized by maximum Fl-QS-2 absorbance. The fluorescence spectra in (b) are normalized by maximum Fl-QS-7 fluorescence intensity. The absorption and fluorescence spectra of sample where free Fl was detected are plotted with the dashed lines Excitation spectrum of Fl-QS-1 matches corresponding absorption spectra (c) and nicely overlaps with absorption of free Fl (d). Note the difference between excitation and absorption spectra of Fl-QS-6, where free Fl was detected.*

excitation profiles nicely match corresponding absorption spectra indicating the presence of single species in solution. Instead, for Fl-QS-5 and Fl-QS-6, a clear difference between excitation and absorption spectra is observed (see Figure 3.5), suggesting that several species are present in solution. Excitation of Fl-QS-7 almost completely overlaps with the absorption spectra of free fluorescein.

The relatively low photostability of fluorescein represents its major disadvantage. One of the approaches to overcome this drawback is the dye nanostructuration. An enhancement of fluorescein photostability inside nanoreactors[81] and zeolite pores[82] was reported. The quantum yield of photochemical decomposition Q_{ph} was estimated for three QS-Fl samples, where the dye is in the bound form, and for free Fl in water (pH=9.0) for comparison. As the absorption of the Fl-QS samples is small, Q_{ph} was estimated using the fluorescence method (Equation (1.15)). The photostability of fluorescein was studied using both absorption and fluorescence method for consistency. Fluorescence degradation upon low intensity continuous-wave laser irradiation is shown in Figure 3.6. It can be clearly seen that Fl-QS are much more stable than free Fl. The quantum yield of photodecomposition of Fl-QS is up to 6 times lower than that of free Fl. We mention that both method of photostability measurement gave the same value of Q_{ph} for Fl. Since the concentration of Fl for fluorescence method was 10^{-6} M while for absorption method it was $2 \cdot 10^{-5}$ we conclude that the reaction of fluorescein photodecomposition is concentration-independent (first order photoreaction). Estimated values of Q_{ph} for free fluorescein agree with the literature data.[83],[29]

Two pathways of fluorescein decomposition were proposed[84] to describe the dye bleaching: the dye-to-oxygen and dye-to-dye reaction. The increase of photostability of encapsulated or nanostructured Fl is related to the quenching of the dye-to-oxygen reaction because of less accessibility of chromophore to the oxygen dissolved in the water. Detailed discussion of the photochemistry of fluorescein can be found in Ref.[84]

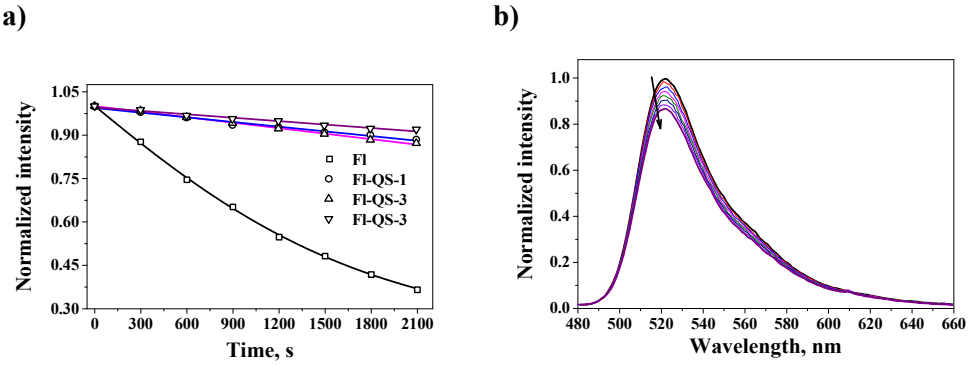

Figure 3.6 *a) Normalized emission intensity decay of Fl, Fl-QS-1, Fl-QS-3. b) Bleaching of Fl-SQ-1 fluorescence under CW irradiation. The time interval between adjacent spectra is 300 s. (λ_{irr}≈476 nm power density 10 mW·cm^{-2})*

3.2 Quatsomes loaded with cyanines. Preparation, characterization and optical properties.

Carbocyanines are a subclass of the large family of cyanine dyes. These dyes are of interest for various photonics application including stochastic optical reconstruction microscopy, 2PF microscopy, photodynamic therapy, optical switching and others. Cyanines have strong fluorescence in green-to-NIR region of interest for biological applications, they are characterized by high molar extinction coefficients, large two-photon response and excellent photostability. In this section we discuss the optical properties of QS loaded with three carbocyanine dyes: 1,1'-dioctadecyl-3,3,3',3'-tetramethyl-indocarbocyanine perchlorate (DiI), 1,1'-dioctadecyl-3,3,3',3'-tetramethyl-indodicarbocyanine perchlorate (DiD) and 1,1'-Dioctadecyl-3,3,3',3'-tetramethylindotricarbocyanine

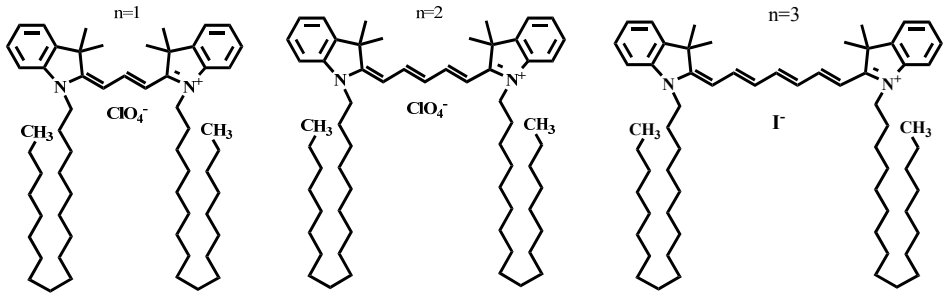

Figure 3.7 *Chemical structures of DiI (left), DiD (center) and DiR (right).*

iodide (DiR), chemical structures are presented in Figure 3.7. These dyes are commercially available and widely used in biomedical studies as neuronal traces.[85]

Dye solution in ethanol was added to cholesterol and then QS were prepared in a standard way[75],[77], resulting in a homogeneous deeply-colored suspension of dye-decorated QS. We will further refer to the QS loaded with DiI, DiD and DiR as I-QS, D-QS and R-QS respectively. As for Fl-QS, several samples with different dye loading defined according to the Equation (3.1) were studied (see Figure 3.8), relevant *L* values being listed in Table 5.

Colloidal stability of all samples was monitored using DLS and nanoparticles tracking analysis (NTA) one week and two month after the preparation. NTA is relatively new (first marketed in 2006) light-scattering method for the measurements of the hydrodynamic diameter and size distribution of nanoparticles in liquid solutions. [86] A sample illuminated with a focused laser beam is observed under a conventional microscope and scattered light is detected with a CCD matrix or a CMOS video camera. The NTA software analyzes the recorded tracks of each particle and calculates the hydrodynamic diameter using the two-dimensional Stokes-Einstein equation. In contrast with DLS, NTA technique can estimate the concentration of nanoparticles in the suspension in the range of ~10^6-10^9 ml^{-1}. The sensitivity of NTA depends on the scattering properties of the nanoparticles, their size

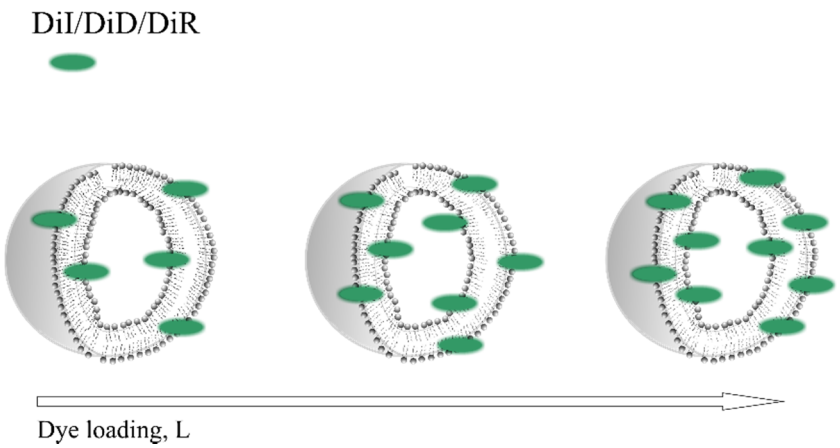

Figure 3.8 *Scheme demonstrating the increase of the local concentration of carbocyanine dyes in QS.*

distribution, concentration and the sensitivity of a detecting camera. Typically it is assumed that the detection limit of NTA is 50 nm.[86]

The DLS instrument was equipped with 633 nm laser making the measurements of D-QS and R-QS impossible due to the strong absorption and\or emission of the samples at this wavelength (see Figure 3.9). The average diameters of R-QS and D-QS listed in Table 5 were measured with NTA and because of its limitation they must be considered with care, keeping also in mind that these are hydrodynamic diameters. However, our main purpose in using NTA and DLS techniques was to check the colloidal stability and possible aggregation of QS. Details of NTA and DLS measurements can be found in Ref.[77]

As it can be seen from Table 5, all samples were stable for at least 2 months after preparation, and the inclusion of the dyes in QS membrane does not affect nanoparticle stability. High values of zeta potential for I-QS proved excellent colloidal stability of dye-loaded quatsomes. Cryo-TEM images of QS loaded with carbocyanines are shown in Figure 3.10. Small unilamellar vesicles

Table 5. Main colloidal and photophysical parameter of QS loaded with carbocyanines: the dye loading [a]L; the average diameter[b]; zeta potential ζ; the fluorescence quantum yield Q_{fl}; maximum extinction coefficient ε_{max} and the photodecomposition quantum yield Q_{ph}.

Sample	L, 10^{-3}	Average diameter, nm	ζ, mV	Q_{fl}, %	ε_{max}, 10^3 M^{-1} cm^{-1}	Q_{ph}, 10^{-5}
DiI in EtOH	-	-	-	11	140	<0.001
I-QS-1	0.6	72 / 69	82	20	115	0.4
I-QS-3	3.3	73 / 76	95	13	112	1
I-QS-5	7	70 / 73	94	10	104	2
DiD in EtOH	-	-	-	30	246.5	<0.008
Cy5 in H_2O	-	-	-	25	[c]250	0.46
D-QS-1	0.57	96 / 114	-	23	246.6	1.3
D-QS-2	1.3	105 / 101	-	19	200	1.4
D-QS-3	3.0	85 / 95	-	11	170	1.9
D-QS-4	4.2	89 / 97	-	10	160.8	1.9
D-QS-5	6.6	106 / 109	-	7	140	1.8
DiR in EtOH	-	-	-	10	270.8	-
R-QS-1	0.5	126 / 121	-	3	201	-
R-QS-3				1	170	-
R-QS-5	5	103 / 114	-	1	136	-

[a] dye loading calculated using Equation (3.1)

[b] measured with NTA for D-QS and R-QS and with DLS for I-QS (see text for explanation). Numbers before and after slash refer to the average diameters estimated one week and one two month after synthesis respectively.

[c] from the GE Healthcare Life Sciences website

with diameters mostly less than 100 nm were found in all samples. The observed size and morphology is marginally affected by dye loading or by the nature of the dye.

Fluorescence and absorption spectra of DiI, DiD and DiR in ethanol and dye-loaded quatsomes are presented in Figure 3.9 (a, c, e). Let's consider free dyes in solution first. All studied carbocyanines show strong absorption (with maximum extinction coefficient ε_{max} up to $270 \cdot 10^3$ $M^{-1} \cdot cm^{-1}$) and emission ($Q_{fl} = 10\% - 30\%$) in the green-to-NIR spectral region. Absorption spectra reveal sharp narrow peaks with a well-resolved vibrational shoulder in the short-wavelength region of the bands. The shoulder is observed in different polymethine dyes and corresponds to a typical vibrational frequency 1200±200 cm^{-1}. The peak of main absorption band and fluorescence spectra shifts by ≈100 nm to the red (from 550 nm for DiI to 647 nm for DiD and to 750 nm for DiR) with increasing the conjugation length *n* by one ethylene unit and also becomes broader. This is an empirical rule which is generally holds true for polymethine dyes.[87],[88]

Now let's discuss the optical properties of cyanines loaded into QS. The absorption spectra of cyanines in dye-loaded QS do not show noticeable spectral shifts (see Figure 3.9 (a, c, e)) and nicely overlap with corresponding spectra of free dyes in ethanol in the region close to 0-0 peak, while in the blue wing the absorption increases with the dye loading. These concentration-dependent changes of absorption spectra of cyanines are well-known and are related with the formation of aggregates. Depending on the mutual orientation of the dye molecules, two types of aggregates are distinguished: head-to-tail or staircase-type orientation gives rise to red-shift and is known as *J-aggregates*, while blue-shift is associated with parallel face-to-face geometry known as *H-aggregates* (see Figure 3.11). While J-aggregates are fluorescent and often their fluorescent quantum yield is higher than for the non-aggregated dye, H-aggregates are non-fluorescent. It was shown that cyanines tend to form aggregates in water solution

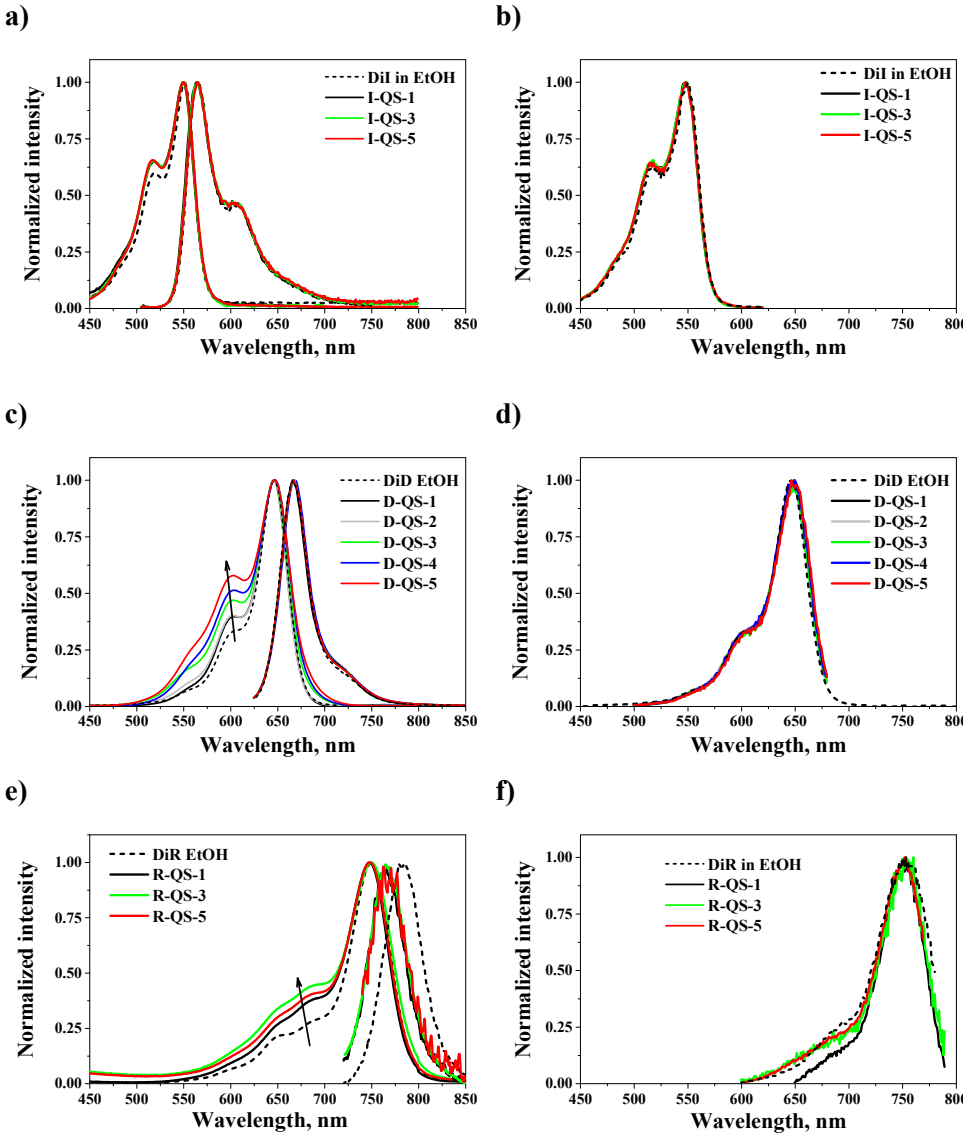

Figure 3.9 *Absorption (a, c, e), fluorescence (a, c, e) and excitation (b, d, f) spectra of DiD in EtOH and D-QS (a, b), DiI in EtOH and I-QS (c, d) and DiR in EtOH and R-QS (e, f).*

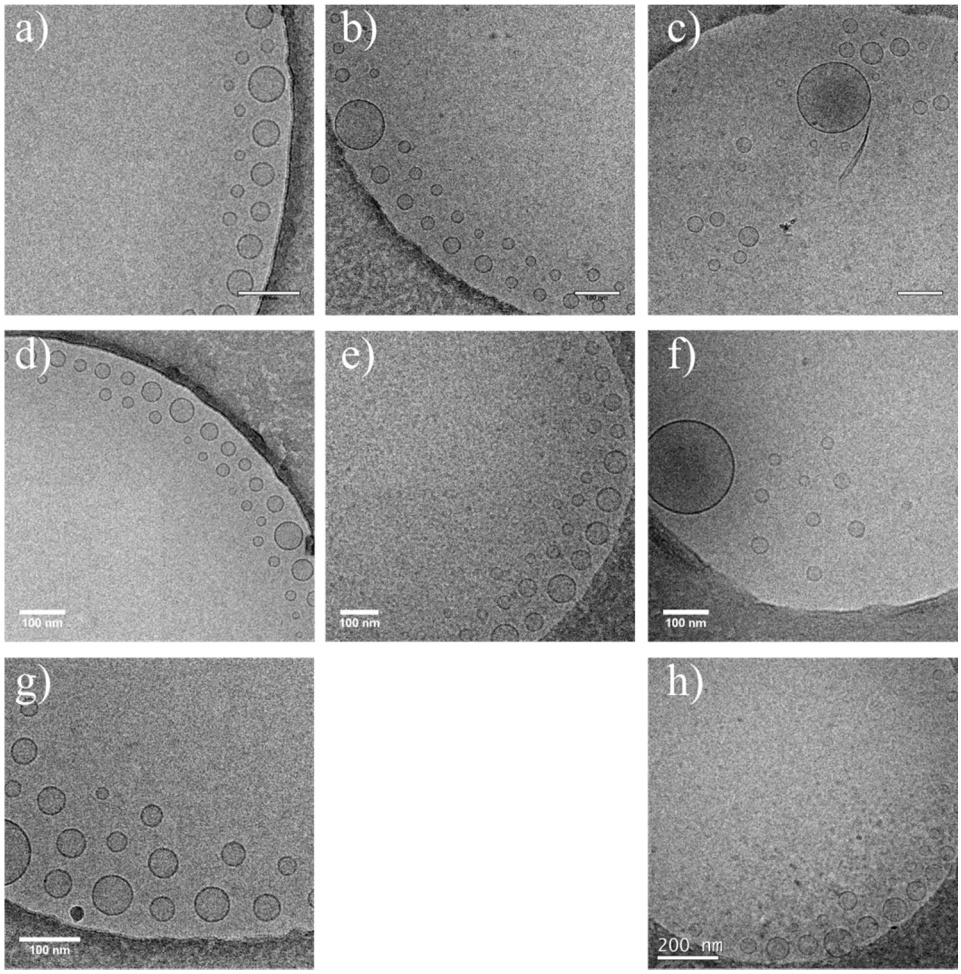

Figure 3.10 *Cryo-TEM images of D-QS (top row), I-QS (middle row) and R-QS (bottom row) (a) D-QS-1, (b) D-QS-3, (c) D-QS-5, (d) I-QS-1, (e) I-QS-3, (f) I-QS-5, (g) R-QS-1 (h) R-QS-5.*

and upon binding with nanoparticles or biological macromolecules and that leads to fluorescence quenching and molar extinction coefficient decrease.[89],[90],[91],[92]

Observed changes in absorption spectra are very weak in I-QS and more pronounced in D-QS and R-QS, and can be explained based on the different length of the conjugation chain. The ability if cyanine dyes to form H-aggregates in water solutions increases with the length of the polymethine bridge.[92] Minor changes in absorption profile of I-QS could be due to environmental effects and\or formation of small number of aggregates. This suggestion is also supported by the fact that the brightness $\varepsilon_{max} \cdot Q_{fl}$ of D-QS-1 is almost 50% higher that that of free DiI in EtOH (see Table 5). However, the decrease in fluorescence quantum yield and molar extinction coefficient in D-QS and I-QS is more abrupt and brightness of D-QS and R-QS rapidly decreases with the increasing of loading degree. As seen in Figure 3.9 the excitation spectra of all cyanine-loaded QS overlap nicely with corresponding spectra of free dyes, proving the idea of formation of non-fluorescent aggregates.

These results are consistent with results of Kawabe[93] who observed similar effect of the fluorescence quenching with the increase of amount of long-chain symmetrical cyanines intercalated into DNA, that was attributed to the formation of irregular aggregates. Similarly with I-QS, short cyanine dyes showed fluorescence enhancement and no changes in absorption upon binding.

Cyanine dyes and their derivatives are also gaining considerable interest as probes for nonlinear optical applications, particularly in two-photon bioimaging due to their large two-photon absorption cross-section, low cytotoxicity and high photostability.[94],[95],[96] To investigate the potential of dye-loaded QS we studied the two-photon response of D-QS, because they fluoresce in the red spectral region and exhibit high fluorescence quantum yield. The degenerate two-photon absorption spectra of D-QS-3, D-QS-5 and DiD in ethanol in 780-1400 nm range obtained by 2PF method are shown in Figure 3.12. The quadratic dependence of fluorescence signal on the excitation pulse

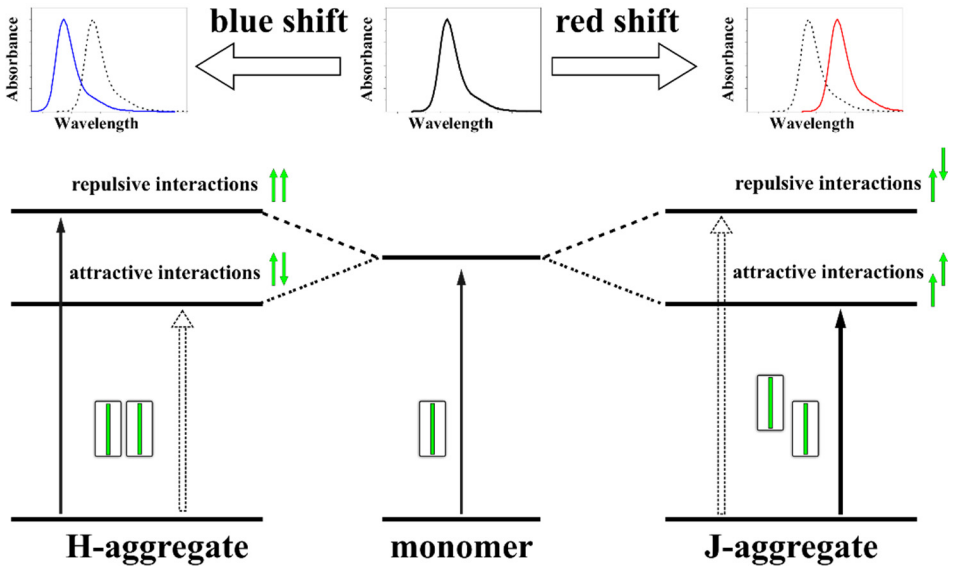

Figure 3.11 *Schematic of H- and J-aggregate structures and corresponding energy levels.*

energy was verified for all wavelengths. A tail of one-photon absorption of DiD limited the possibility of measuring its two-photon response above 780 nm, since the small probability of absorption of two photons it is overwhelmed even by small 1PA. As it was discussed before, the one-photon excitation anisotropy is a useful tool for analyzing 2PA spectra, so the anisotropy spectrum of DiD in pTHF was also collected.

2PA spectrum of DiD is similar to that observed for symmetrical cyanines and displays two bands, one sharp and intense at 800 nm with 2PA cross-section δ≈900 GM and a shallow peak at 1100-1200 nm with δ≈100 GM. The excitation anisotropy in the 700-900 nm region exhibits two valleys and a peak, pointing to the presence of several electronic transitions that are not active in 1PA spectrum. The large value of δ for the high-energy 2PA transition is ascribed to a state allowed in 2PA and forbidden in 1PA, as expected for

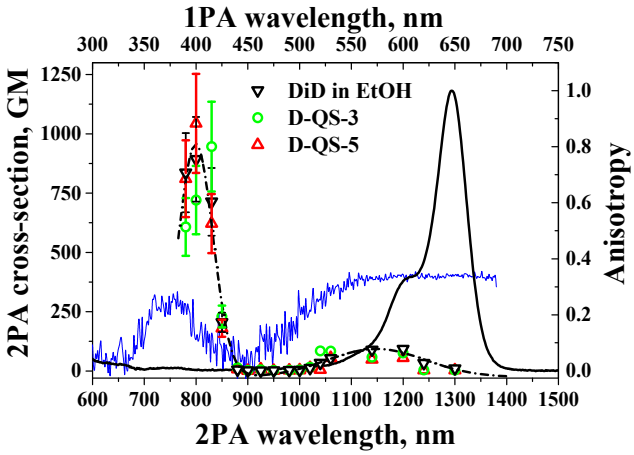

Figure 3.12 *Two-photon absorption spectra of D-QS-3, D-QS-5 and DiD in ethanol. Black line is one-photon absorption spectra of DiD in ethanol, blue line is one-photon excitation anisotropy of DiD in pTHF. Dashed line is to guide an eye.*

symmetrical molecules.[97],[98] The second 2PA band is observed within 1PA contour. In this spectral region (550-700 nm) one-photon excitation anisotropy is constant suggesting a single $S_0 \rightarrow S_1$ electronic transition and the 2PA transition to this state is nominally forbidden.

However, the selection rule is relaxed by the coupling to molecular vibrations, in a mechanism similar to the Herzberg-Teller vibronic activation of forbidden bands in linear absorption spectra, and/or by symmetry-lowering as due to the polar solvation.[87],[99], Indeed the maximum of the lowest energy 2PA band in symmetric cyanines always corresponds to the vibrational shoulder of 1PA band.[87],[88] Also J. Fu et al.[87] have demonstrated the increase of the intensity of the weak 2PA band with the lengthening of the polymethine chain. For example, in the indolium series of polymethine molecules maximum cross-section of the weak band increased from 10 GM for a molecule with small

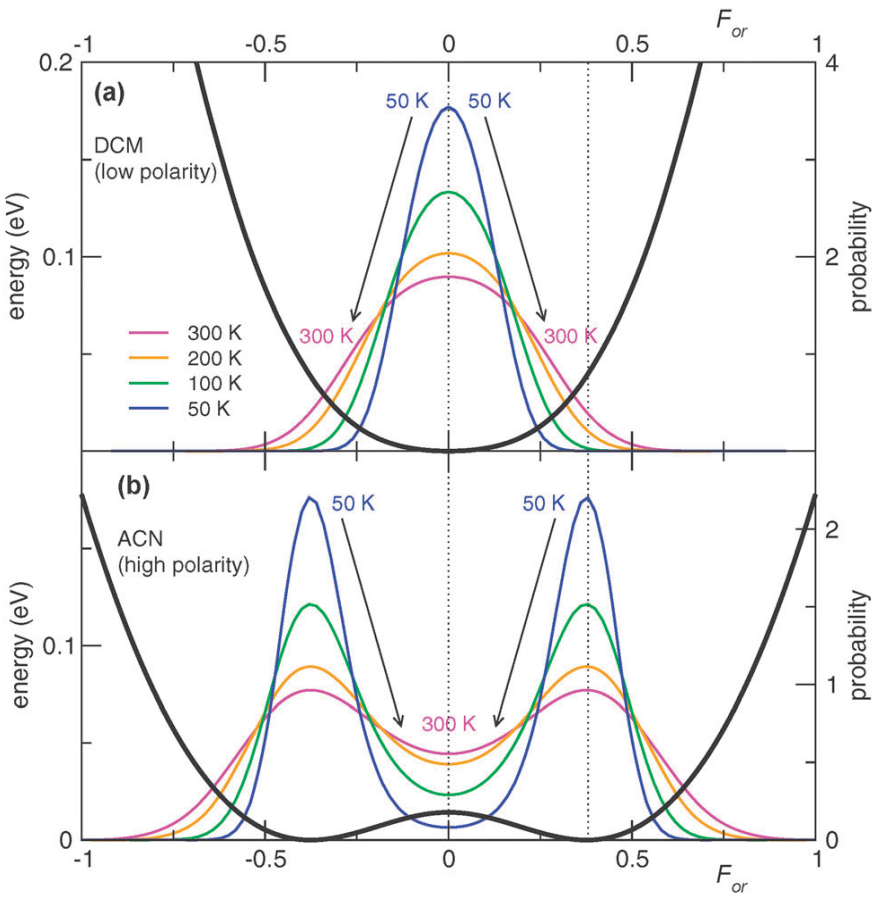

Figure 3.13 *(a) and (b): calculated ground-state energy (black thick line) vs. the solvation reaction field F_{or} for the low-polarity solvent (a, ε_{or} = 0.23 eV modeling DCM) and for the high-polarity solvent (b, ε_{or} = 0.35 eV modeling ACN); Boltzmann probability distributions of the reaction field (based on the ground state energy) at different temperatures (see legend). Adapted from Ref.[100] with permission of The Royal Society of Chemistry.*

conjugation length (n=1) to 600 GM when n=4, indicating that the lengthening of the chain favors the symmetry breaking.

Polar solvents can also induce symmetry-breaking in molecules with large charge separation as demonstrated by strong increase in intensity of

vibrational shoulder of symmetrical polymethines.[98],[100] This effect was attributed to existence of dye molecules with asymmetric charge density and was fully explained using the essential-state models.[99],[100] The probability distribution dependence of the solvation reaction field F_R in solvents of different polarity modeled for symmetric polymethine dye is shown in Figure 3.13. In the solvent of medium polarity (panel a) the distribution is monomodal and symmetric, indicating the presence mainly of molecules with symmetric charge density distribution. In the polar ACN the situation is completely different. The field distribution is bimodal showing a significant amount of dye molecules in a symmetry-broken state. This effect depends also on the polymethine chain length, and it is much more pronounced in the cyanines with long chains.[99] The solvent and vibronic contribution to the low-energy 2PA band can be described using four-level model, discussed in details in Ref.[101]

Despite of evidence of aggregation of carbocyanines in QS, the two-photon response of D-QS coincides within the error with the spectrum of free dye in ethanol and does not show any changes with the dye loading. That implies that the two-photon response of the H-aggregates within tested concentration range is negligible. This is a big advantage of QS for cyanines formulations in water. Various FONs show decreased two-photon response in water compared to the 2PA of corresponding dyes in organic solvents. For example, maximum 2PA cross-section of micelle-encapsulated cyanine 5 (Cy5) - a hydrophilic dye that has the same chromophore part as DiD - is reduced 5 times compared to the free dye in DMSO.[102]

The studies of optical properties of the quatsomes-based FONs loaded with carbocyanine show that they might be attractive candidates for imaging applications. To have a better insight in their application potential the photostability of I-QS and D-QS was studied (see Table 5 and Figure 3.14). Under the available laser power density of 22 mW/cm^2 the decrease in absorption of DiI and DiD was very small, therefore only the upper bound of

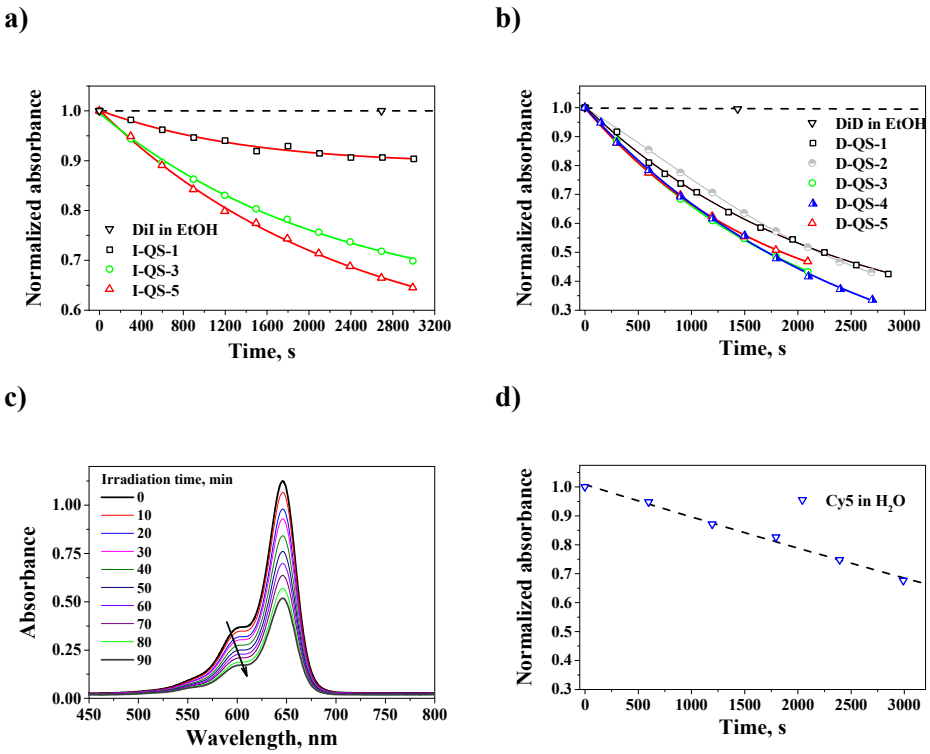

Figure 3.14 *Photobleaching of (a) DiI, I-QS (λ_{irr}≈660 nm), (b) DiD and D-QS (λ_{irr}≈531 nm) and Cy5 (λ_{irr}≈647 nm) (c, d). Power density is 22 mW/cm^2.*

Q_{ph} for these dyes could be estimated. However, due to the different solvents the photostability of DiD and DiI in ethanol cannot be compared with the photostability of dye-loaded QS. Therefore for comparison we estimated the Q_{ph} of Cy5 in water (see Figure 3.14). The estimated photostability (see Table 5) agrees well with reported in Ref.[29] The photodecomposition quantum yield of I-QS and D-QS varies in the range of Q_{ph} =0.4·10^{-6}-2·10^{-5} and the D-QS samples are less stable compared to the Cy5. However, D-QS have the same Q_{ph} reported for DiD in aprotic DMSO and are much more photostable (2 order of magnitude) than other surfactant-based micelle formulation of DiD in water.[102]

The reason of lower photostability of D- and I-QS in water can be attributed to aggregation and solvent effects. It is well-known that the

photostability of cyanines generally is affected by the aggregation and by the concentration of oxygen. [89],[103],[104], Monomeric form (concentration C~μM) of indo-, thia- and oxacarbocyanines in organic solvent exhibits low photodegradation quantum yields (Q_{ph}<10^{-6}), while aggregates (C~mM) are significantly less photostable (Q_{ph}>10^{-3})[103]. The oxygen removal reduces Q_{ph} to ≈10^{-4}. Solvents polarity and specific solute-solvent interactions also affect the photostability. Generally, Q_{ph} of organic dyes in water is reduced compared to the other solvents.[29],[102] Since the solubility of oxygen in ethanol is higher than in water[9] the aggregation state and specific solvent interaction seem to be the dominant factors in reducing the Q_{ph} of DiD and DiI in QS. This is also supported by molecular dynamics simulations[77] and photophysical studies (see above).

The photobleaching of DiD and DiD-loaded lipid nanoparticles (DiD-LNP) under similar excitation geometry (simultaneous illumination of whole sample by a homogeneous laser beam, λ_{irr}≈633 nm) was also studied by Texier et al.[91] They have calculated the half-lives of the samples from the slopes of fluorescence bleaching curves and found that the DiD in methanol was one order of magnitude more stable than DiD-LNP in phosphate-buffered saline. It should be noted that these results can not be directly compared with the photodecomposition quantum yields Q_{ph}, because of the probable difference in molar extinction coefficients of DiD and DiD-LNP (not reported) at λ_{irr}≈633 nm the number of absorbed photons differs in each sample, leading to the different rate of bleaching. However, qualitatively they are similar with observed trends of photodegradation of DiD in ethanol and D-QS in water. The reason of lower photostability of DiD-LNPs was similarly attributed to the possible interactions of chromophore with oxygen and ions that are able to diffuse through the fluid surfactant surface of LNP.[91]

3.3 Quatsomes labeled with fluorescent sterol. Preparation, characterization and optical properties

We discussed two approaches for preparing QS-based fluorescent organic nanoparticles based on introducing extrinsic fluorophores using electrostatic or hydrophobic interactions. In order to demonstrate the great flexibility of QS we checked the possibility of substituting the cholesterol of QS membrane with its fluorescent analog. Currently fluorescent sterols are divided into two big groups:[105],[106]

a) intrinsically fluorescent sterols
b) sterols covalently linked to extrinsic chromophore groups.

Dehydroergosterol and cholestatrienol are the most widely used representatives of the first group[107], but they are prone to photobleaching and have poor brightness (the product $Q_{fl} \cdot \varepsilon_{max}$) because of low fluorescence quantum yield (Q_{fl}=4% in EtOH) and molar extinction coefficient (ε_{max}=(10-11)·10^3 M^{-1}·cm^{-1}). Both these sterols fluoresce in the UV range (~380 nm) so UV-optimized optics and sensitive detector are required for imaging.

The second group includes sterols with attached fluorescent tags. This represents a much more flexible approach, since it allows some freedom in the choice of the appropriate fluorophore. Boron-dipyrromethene dyes (BODIPY), 5-dimethylamino-1-naphthalenesulfonyl (dansyl) and 7-nitrobenz-2-oxa-1,3-diazole (NBD) chromophore groups are commonly used for these purposes. Amongst others, NBD tagged sterols have attractive properties for bioimaging - NBD has strong fluorescence in the yellow-green part of the spectrum, reasonably high ε_{max}≈(20-25)·10^3 M^{-1}·cm^{-1} (for 22- and 25-NBD-cholesterol) and is sufficiently photostable.[105] NBD-tagged cholesterol was chosen as a test fluorescent lipid for substitution of cholesterol in QS. We used 5-cholesten-3β-ol 6-[(7-nitro-2-1,3-benzoxadiazol-4-yl)amino]caproate (NBD-6 cholesterol, chemical structure is shown in Figure 3.15).

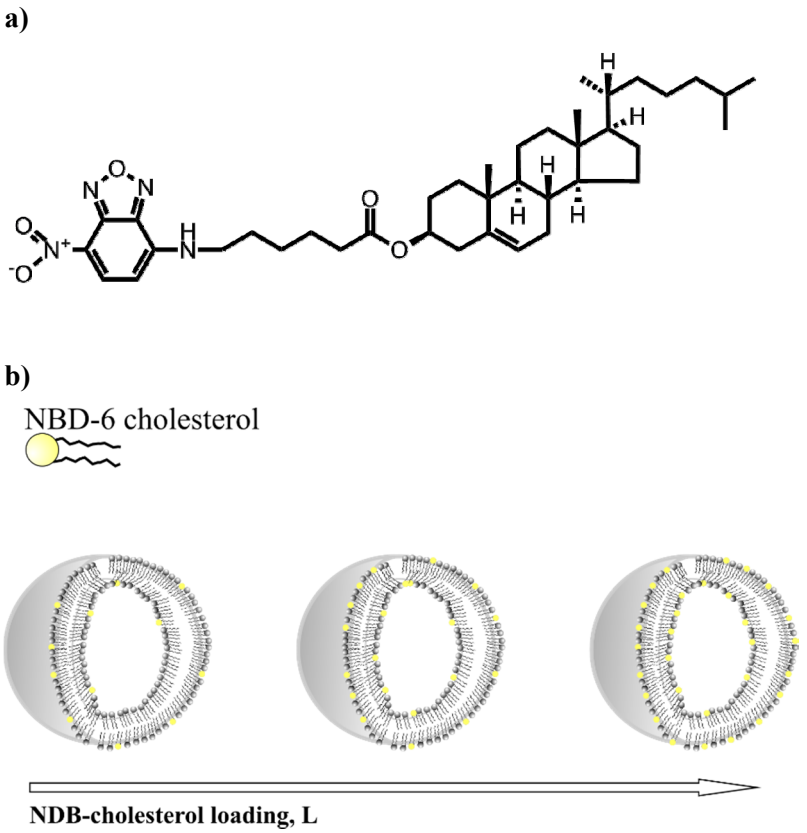

Figure 3.15 *(a) Chemical structure of NBD-6 cholesterol. (b) Sketch of N-QS structures with increasing the NBD-6 cholesterol loading L.*

Five different samples of QS (see Figure 3.15 (b)) where cholesterol was substituted with its fluorescent analog (N-QS) were prepared by DELOS-SUSP method.[75] NBD-6 cholesterol and cholesterol were dissolved in ethanol in proportions reported in the Table 6 and then the standard procedure of QS preparation was followed. The N-QS-4 and N-QS-5 samples were prepared using half amount of cholesterol and CTAB, therefore resulting concentration of QS was approximately two times less than for other samples. As previously described for Fl-QS and for QS loaded with carbocyanine dyes, the colloidal

stability and the morphology of N-QS were tested by DLS and Cryo-TEM microscopy techniques.

According to the DLS measurements all N-QS suspensions have monomodal size distribution with average hydrodynamic diameter of ≈70 nm (see Figure 3.16). These results are consistent with DLS and NTA analysis of dye-loaded quatsomes. Also, as for Fl-QS and I-QS DLS, N-QS samples have high positive zeta potential (≥ 60 mV), equal to that of plain QS (see Figure 3.16). High surface charge ensures long term stability of nanoparticles and no apparent changes in the average hydrodynamic diameter and zeta potential were observed within 2 months. No effect of NBD-6 cholesterol loading on size or zeta potential was detected. Cryo-TEM images of N-QS samples with different degree loading do not show any evidence of NBD-6 cholesterol influence on the nanoparticles morphology. Small unilamellar vesicles with similar morphology were found in all samples (see Figure 3.17).

The fluorescence and excitation spectra of NBD-6 cholesterol in ethanol and N-QS in water are plotted in Figure 3.18 and main photophysical parameters are listed in Table 6. Absorption spectra of NBD-6 cholesterol show two bands: one broad and intense band with maximum at 470 nm and a second less intense band at 330 nm. Both bands show minor red-shift in N-QS. According to the quantum-chemical calculations[108] the long-wavelengths band is attributed to the single electronic transition from the ground to the first excited state $S_0 \rightarrow S_1$, while band at 330 nm appears due to the $S_0 \rightarrow S_3$ transition.

Fluorescence spectra of NBD-6 cholesterol are affected by incorporation in QS. Fluorescence of free NBD-6 cholesterol in ethanol peaks around 530 nm while fluorescence of N-QS is red-shifted and broadened. The concentration-dependent red-shift and broadening of NBD-6 cholesterol fluorescence at low cholesterol concentrations was also observed in unilamellar[109],[110] as well as in multilamellar[111],[112] vesicles. Although the maximum of fluorescence spectra

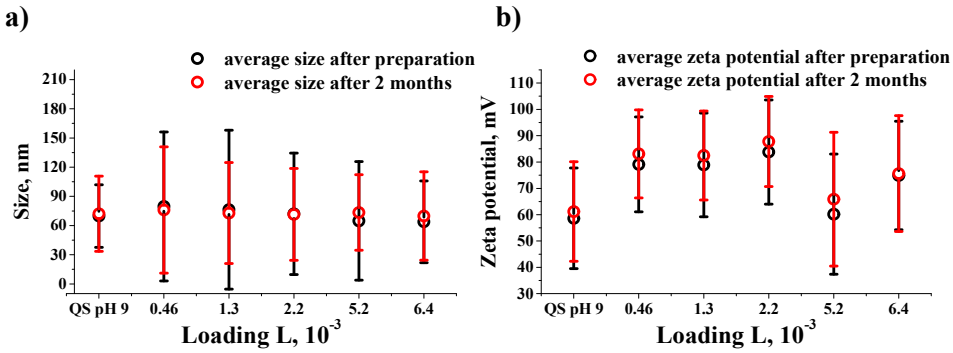

Figure 3.16 *Average size and zeta potential of N-QS with different loadings.*

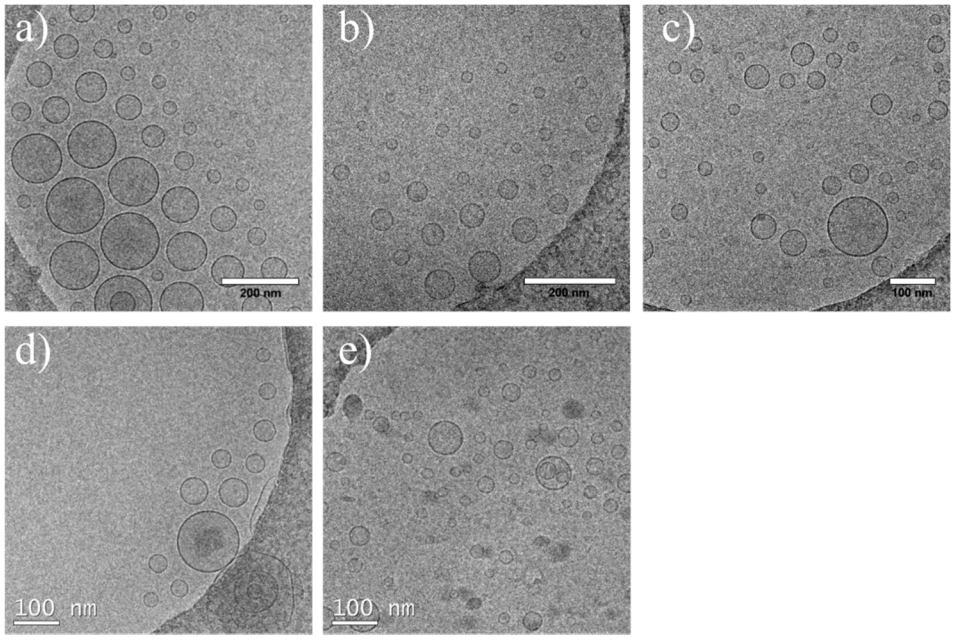

Figure 3.17 *Cryo-TEM images of QS loaded with NBD-6 cholesterol. a) N-QS-1, b) N-QS-2, c) N-QS-3, d) N-QS-4, e) N-QS-5. Scale bar equals 200 nm in (a), (b) and 100 nm in (c)-(e).*

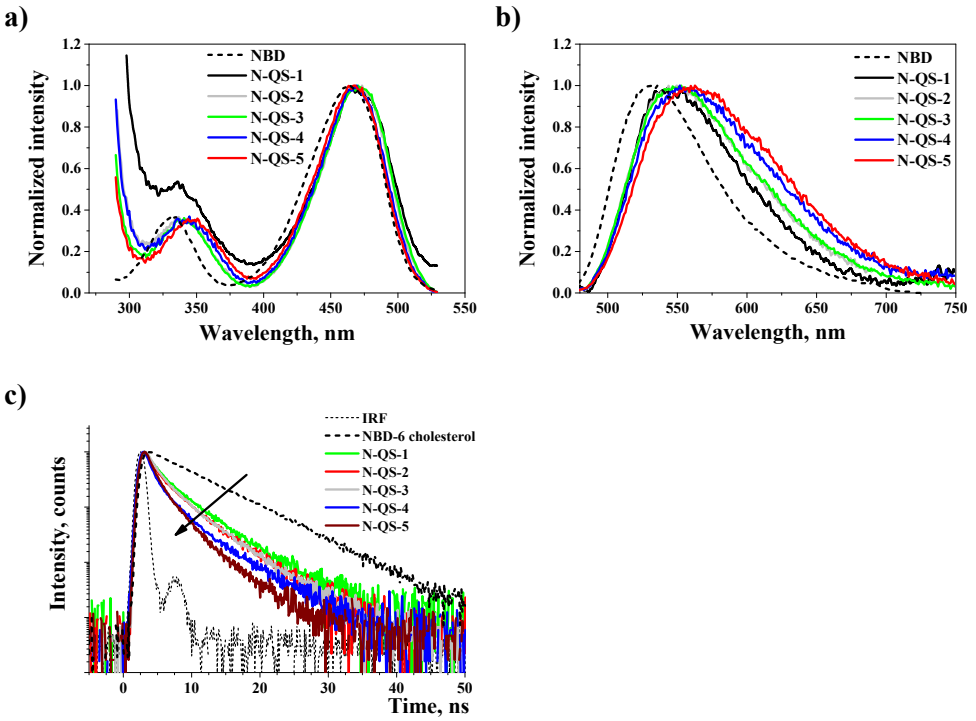

Figure 3.18 *(a) Normalized excitation, fluorescence (b) spectra and fluorescence decay curves (c) of NBD-6 cholesterol and N-QS. IRF is instrument response function.*

of NBD-6 cholesterol is known to depend on the solvent polarity,[108],[113] the spectral broadening is typically associated with aggregation. As is was shown in the literature[111],[114],[112] NBD cholesterol tend to aggregate even at very low local concentrations, forming tail-to-tail dimers (see Figure 3.19). This aggregation leads to effective fluorescence self-quenching.[109],[115] Since the structure of NBD-6 cholesterol is very close to pure cholesterol the possibility of dimer formation between these two molecules in cholesterol-rich membranes has also been checked.[109] The fluorescence of NBD-6 cholesterol was insensitive to the concentration increase of pure cholesterol in dipalmitoylphosphatidylcholine

Table 6. Main photophysical parameters of NBD-6 cholesterol and N-QS: dye loading *L;* maximum extinction coefficient ε_{max}; Q_{fl} - the fluorescence quantum yield; [a]τ_{fl} - the fluorescence lifetime and Q_{ph} - the photodecomposition quantum yield.

Sample	N-QS-1	N-QS-2	N-QS-3	N-QS-4	N-QS-5	[b]NBD-6 cholesterol
L, 10^{-3}	0.46	1.3	2.2	5.2	6.4	-
ε_{max}, 10^3 $M^{-1}\cdot cm^{-1}$	18	16	13	13	12	23
Q_{fl}, %	8	4	4	2	3	50
τ_{fl}, ns	0.3 (0.11) 2.1 (0.4) 5.8 (0.49) $\langle\tau\rangle$=3.7	0.6 (0.20) 2.5 (0.45) 6.0 (0.35) $\langle\tau\rangle$=3.4	0.6 (0.15) 2.3 (0.48) 5.8 (0.37) $\langle\tau\rangle$=3.3	0.5 (0.30) 2.0 (0.46) 6.4 (0.25) $\langle\tau\rangle$=2.6	0.5 (0.23) 1.9 (0.55) 4.9 (0.21) $\langle\tau\rangle$=2.2	7.1
Q_{ph}, 10^{-5}	3.6±0.3	5.0±0.5	4±2	4±1	5.8±0.9	4.8±0.3

[a] in parenthesis are normalized amplitudes of corresponding fluorescence decay components, $\langle\tau\rangle$ is the average lifetime.

[b] in ethanol solution

unilamellar vesicles, therefore formation of this type of complex was ruled out, showing the presence of dimers formed only by fluorescent sterols. The fluorescence quantum yield, the fluorescence lifetime and molar extinction coefficient of N-QS decreased with the increasing the dye loading. This trend is similar to that observed for Fl-QS and QS loaded with the carbocyanine dyes.

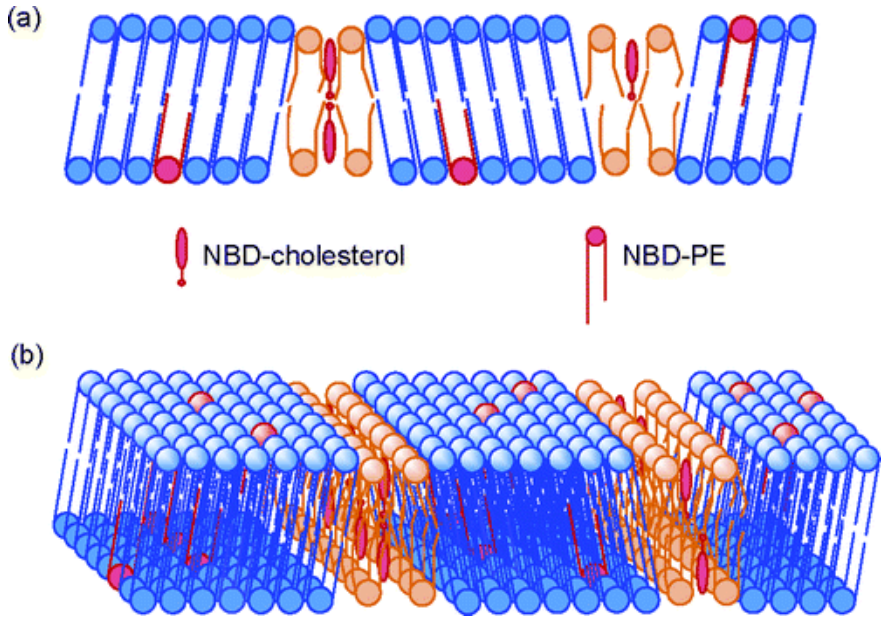

Figure 3.19 *Schematic flat (a) and 3D (b) representations depicting the distribution of 25-NBD-cholesterol in dipalmitoyl-sn-glycero-3-phosphocholine membranes. Reprinted with permission from Ref. [112] Copyright 2007 American Chemical Society.*

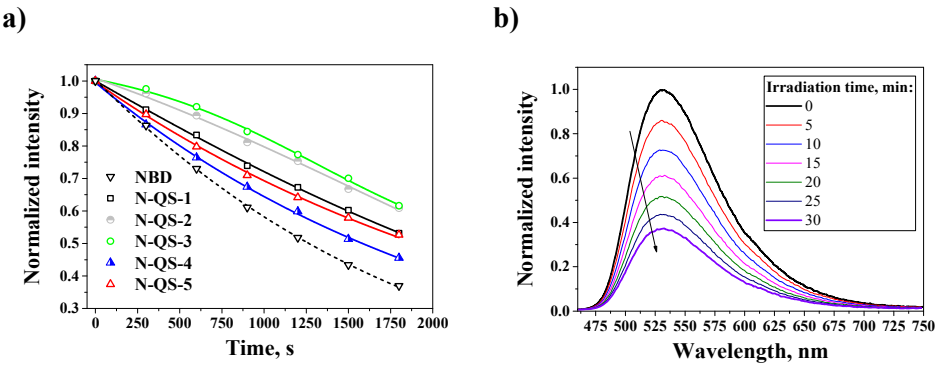

Figure 3.20 *(a) Normalized emission intensity decay of NBD-6 cholesterol in ethanol and N-QS-1. (b) Photobleaching of NBD-6 cholesterol fluorescence under CW irradiation. The time interval between adjacent spectra is 300 s. (λ_{irr}≈476 nm power density 60 mW·cm^{-2}).*

The fluorescence quantum yield of NBD-6 cholesterol in ethanol is ≈50% and its fluorescence decays exponentially with the lifetime of 7.1 ns.

In N-QS fluorescence decay was found to be triexponential and an abrupt drop both in τ_{fl} and Q_{fl} was observed. The fluorescence lifetime further decreases in the samples with the increasing dye loading. Typically, the lifetimes of NBD derivatives in organic solvents are in the range of 5-11 ns, however in the presence of water NBD becomes weakly fluorescent (Q_{fl} ≤0.3%) with the τ_{fl} ≤1 ns[113],[116]. This effect was explained by formation of a hydrogen bond that increase the non-radiative decay constant rate.[116] Molecular dynamics simulations[108] of NBD-labeled lipids in lipid bilayers show that NBD group is largely exposed to water and forms large number of H-bonds and the complex character of fluorescence decay profile was attributed to the significant variations of the degree of NBD solvation.

Surprisingly, the photostability of NBD-6 cholesterol in ethanol is comparable with its photostability in N-QS (see Figure 3.20 and Table 6). Although fluorescence data suggests that the NBD group is in contact with water, this has minor impact on the photostability of the probe.

3.4 Conclusions

In this chapter we demonstrate various strategies of creating fluorescent organic nanoparticles using quatsomes as nanocarriers. First approach utilizes the electrostatic interaction between anionic dye (fluorescein) and positively charged surface of the membrane. Fluorescence and absorption spectra of fluorescein attached to the membrane exhibited small red-shift accompanied with the fluorescence quantum yield decrease. Due to the dynamic nature of binding these samples are of interest only for fundamental studies, however the nanostructuration of fluorescein over QS improves its photostability of up to 6 times.

The second strategy demonstrates the potential of QS for solubilizing hydrophobic carbocyanine dyes in water. The aggregation of cyanine dyes loaded in the membrane is detrimental, leading to decreased fluorescent quantum yield and molar extinction coefficients. However, these changes were found to be dependent on the conjugation length *n* and, at least for I-QS they are marginal. The two-photon absorption cross-section of D-QS do not show any dependence on the loading degree and equal that of free dye in ethanol. This is a big advantage of QS for solubilizing dyes in water, over other FONs, where 2PA cross-section of dyes usually decreases. Cyanine-loaded QS are significantly less photostable compared to the free dyes, but still stable enough for most applications.

In the third approach we demonstrate the possibility of creating QS-based fluorescent nanoparticles by substituting the cholesterol of QS membrane with fluorescent NBD-cholesterol. Similarly to Fl-QS and carbocyanine-loaded QS the fluorescence quantum yield of N-QS was found to be lower compared to the free NBD-cholesterol in ethanol, due to the aggregation and interactions with solvent. The encapsulation of NBD-6 in the membrane has no effect on the photostability of the dye.

Colloidal properties of all samples of QS-based fluorescent nanoparticles were the same as for plain QS, and no noticeable changes in hydrodynamic diameter were observed within two months, with the only exception of the sample of QS-FL-7, where high concentration of anionic dye causes lowering of zeta potential. The observed size and morphology is marginally affected by loading degree in all three studied cases. Small unilamellar vesicles with similar morphology were found in all samples.

Overall QS offer a versatile strategy for nanostructuring organic dyes in biological environment, leading to stable suspension with a good photostability, while preserving the 2PA brilliance. QS offer additional advantages, as they can be further functionalized on the outer wall with designed functional groups to target specific biological entities, as needed for bioimaging. Moreover, they have

already been used as carriers for drugs,[74] opening the perspective of theranostic applications.

4 DYE-DECORATED QUATSOMES FOR RESONANCE ENERGY TRANSFER APPLICATIONS

When light is shined on two nearby molecules, an interesting process may occur, known as *energy transfer*. Specifically, if light is absorbed by one of the two molecules, the energy can be transferred from the excited energy donor (D^*) to the nearby molecule, the energy acceptor (A), bringing it to the excited state. The $D^*A \rightarrow DA^*$ process is called *energy transfer*. The energy can be transferred by a two-step process, when an acceptor absorbs a photon emitted by a donor molecule. This trivial type of energy transfer is known as *radiative energy transfer*. It does not affect the rate constants of excited state relaxation of the donor and takes place only when the distance between D and A exceeds the wavelengths of the photon. The efficiency of this type of energy transfer is defined by the concentration and spectroscopic properties of D and A, such as the donor fluorescence quantum yield, acceptor 1PA cross-section and spectral overlap between D fluorescence and A absorbance.

When D and A are closer than the wavelength of the exchanged photon, the energy transfer occurs without the emission of real photons and is called *non-radiative energy transfer*. Although it also requires the spectral overlap of donor emission and acceptor absorption it is a distance-dependent process and provides information about the mutual orientation of the donor-acceptor pairs. Depending on the type of molecular interactions several mechanisms can be involved in non-radiative energy transfer. At very short distances (<10 Å), when molecular orbitals of D and A overlap, energy can be transferred through electron exchange[10] in the so-called Dexter mechanism. The efficiency of Dexter energy transfer falls off exponentially with the distance, as contrasted

with r^{-6} dependence predicted by Förster for the dipolar interactions as described below in more details.

4.1 Förster resonance energy transfer

The most important mechanism of non-radiative energy transfer occurs when the distances between D and A are in the range of 10-100 Å. According to the theory of resonance energy transfer developed by Förster[117] (FRET) the interacting chromophores are approximated as point dipoles. A simplified energy level scheme of two interacting molecules is presented in Figure 4.1. Here we refer to the case of weak interactions that do not change the electronic structures of D or A. In this system the excited donor molecule can transfer its energy to the nearby acceptor with a rate $k_{FRET}(r)$ defined by:[117]

$$k_{FRET}(r) = \frac{1}{\tau_D}\left(\frac{R_0}{r}\right)^6 \tag{4.1}$$

where τ_D is the lifetime of donor in absence of acceptor, r is the $D-A$ distance, and R_0 is the Förster distance. R_0 is defined as the $D-A$ distance at which a donor molecule has 50% probability to decay through energy transfer. R_0 depends only on the spectral properties of donor and acceptor:[9]

$$R_0^6 = \frac{9000 ln10 \kappa^2 Q_D}{126\pi^2 N_A n^4} \int I_D(\lambda)\varepsilon_A(\lambda)\lambda^4 d\lambda \tag{4.2}$$

where $I_D(\lambda)$ and Q_D are area-normalized fluorescence spectra ($\int I_D(\lambda)d\lambda = 1$) and the fluorescence quantum yield of the donor in absence of energy transfer $\varepsilon_A(\lambda)$ is acceptor molar extinction coefficient, and κ^2 is the orientational factor, describing D and A dipole orientations.

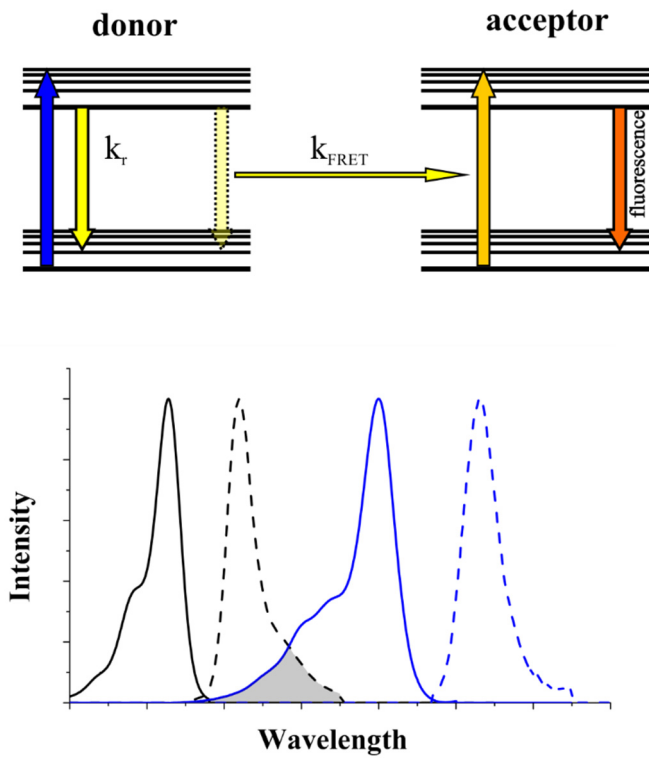

Figure 4.1 *Top – Jablonski diagram for FRET process. Non-radiative processes are excluded for simplicity. Bottom – donor (black) and acceptor (blue) absorption (solid) and emission (dashed curves) spectra. Spectral overlap is shaded.*

From Equations (4.1) and (4.2) the conditions for FRET are:

- Proximity of the donor and acceptor molecules, $r = (10 - 100)$ Å
- Significant values of the spectral overlap integral
- Favourable orientation of D and A (non-zero κ^2 factor)
- High values of donor fluorescence quantum yield

It is important to notice that the shaded area in Figure 4.1 equals to the spectral overlap and does not give an estimate of the magnitude of the overlap integral, because of wavelength to the fourth power factor in the integral (4.2)

and of the different units of ε_A and I_D. Typical R_0 values for commonly used $D-A$ pairs are in the range of 30-90 Å.[9],[10] When FRET between dyes bound to macromolecules (DNA, RNA) or vesicles is studied, the values of I_D and ε_A in corresponding environments have to be used to calculate the overlapping integral. In that case the local value of the refractive index n in the material should be used, that is sometimes hard to know. In general, this does not introduce significant errors because of the limited variability range of n.

The factor κ^2 in equation (4.2) depends on the mutual orientation of the donor and acceptor dipole moments and can be expressed as:[117]

$$\kappa = \boldsymbol{d}\cdot\boldsymbol{a} - \mathbf{3}(\boldsymbol{r}\cdot\boldsymbol{d})(\boldsymbol{r}\cdot\boldsymbol{a}) \qquad (4.3)$$

where $\boldsymbol{d}$ and $\boldsymbol{a}$ are unit vectors pointing in the direction of donor and acceptor dipole moments respectively, and $\boldsymbol{r}$ is unit vector pointing in the direction from donor to acceptor, or if we consider three angles between these three vectors as shown in Figure 4.2:

$$\kappa^2 = (cos\theta_{da} - 3cos\theta_d cos\theta_a)^2 \qquad (4.4)$$

Depending on the $D-A$ orientation κ^2 takes values from 0, when $\boldsymbol{d}$ is perpendicular to $\boldsymbol{a}$, to 4 when donor and acceptor are aligned head to tail. These cases are demonstrated in Figure 4.2.

Since FRET occurs during excited state lifetime of the donor, the κ^2 value is defined by the rotational and translational mobility of donor and acceptor species during this timescale. In non-viscous solutions typical rotational diffusion times of small chromophores are in the order of tens of picoseconds, what is much smaller compared to the typical excited state lifetimes, in the order

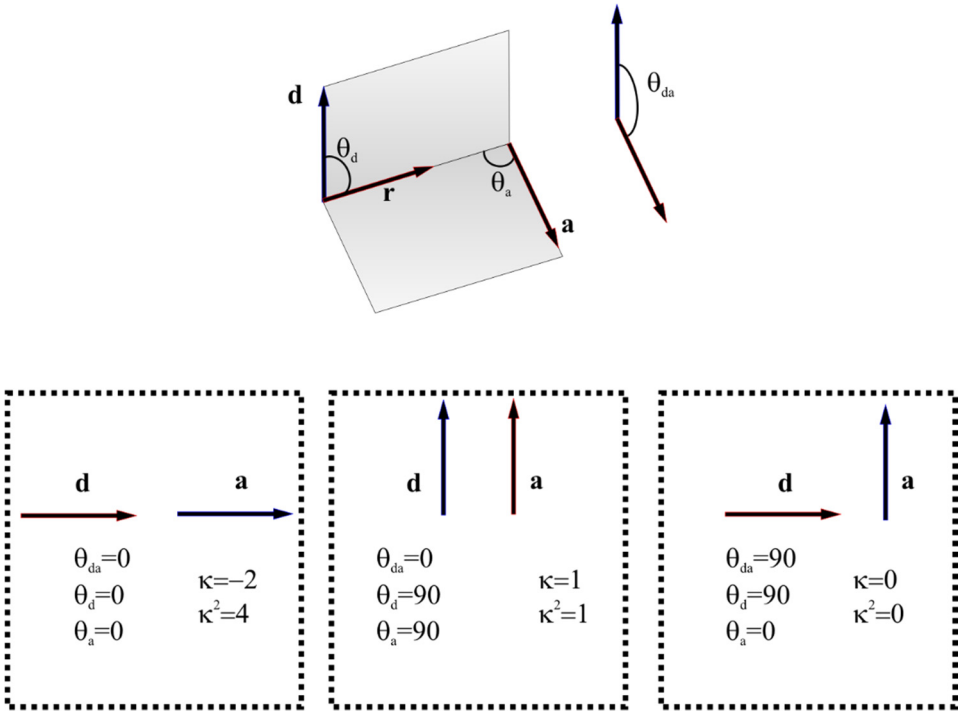

Figure 4.2 *Top – definitions of the angles between D and A dipoles. Bottom – values of* κ *for some fixed* $D-A$ *orientations.*

of nanoseconds. Therefore, before energy transfer occurs chromophores in non-viscous solvents take all possible mutual orientations during the excited state lifetime of the donor. This is known as *dynamic-averaging regime*. The values of κ^2 are averaged over all possible $D-A$ orientations and for an isotropic distribution $\langle\kappa^2\rangle = 2/3$.

However, in many practical cases when D and A are rigidly bound to biomacromolecules such as DNA, membranes, proteins, or put in rigid matrix the rotational and translational motion of molecules may be restricted. In this case the positions of D and A are fixed within the decay time of D, and for each $D-A$ pair energy transfer occurs with different efficiency. The values of κ has

to be averaged in *static regime* for all pairs, and for random spatial distribution of D and A $\langle\kappa\rangle^2 \approx 0.4762$.[117]

4.2 FRET applications

Since FRET opens an additional de-excitation channel for a donor molecule, with a rate given by equation (4.1), the ratio of the fluorescence quantum yield of donor in presence Q_D and absence of energy transfer Q_D^0 becomes:

$$E_{FRET} = Q_D/Q_D^0 = \frac{k_r/(k_r + k_{nr} + k_{FRET})}{k_r/(k_r + k_{nr})} = \frac{R_0^6}{R_0^6 + r^6} \qquad (4.5)$$

The ratio E_{FRET} in (4.5) measures the efficiency of FRET. It can also be estimated from the decrease in donor fluorescence lifetime or, for fluorescent acceptors, it can be related to the increase in the acceptor fluorescence quantum yield. E_{FRET} gives information about the distance and relative orientation between donor and acceptor species. The very steep dependence of E_{FRET} on the $D - A$ distance makes this technique very sensitive and suitable for measuring distances with resolution up to several Å. This fact lead Stryer and Haugland[118] to describe FRET as a *spectroscopic ruler*. In practice, because of nonlinear dependence of FRET efficiency of the $D - A$ distance the technique is applicable in the range of $0.5R_0$ to $1.5R_0$ (see Figure 4.3). Apart of qualitative measuring the distances FRET is also useful as a quantitative measure of proximity of two molecules. The range of FRET distances is comparable with the size of different biomacromolecules, making it particularly appealing for biological applications. This includes studying wide range of molecular recognition and analytes detection,[9],[119],[120] and it complements fluorescence lifetime imaging spectroscopy allowing visualization of complex processes in

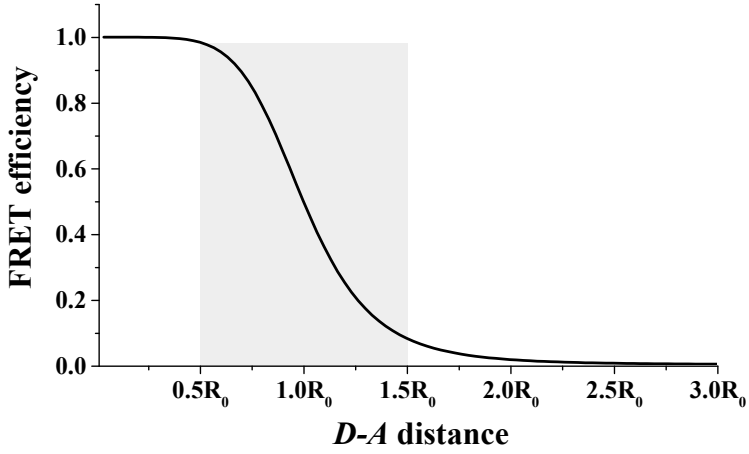

Figure 4.3 *FRET efficiency dependence on $D-A$ distance.*

live cells such as protein–protein interactions or conformational changes within proteins.[121]

Another appealing application of FRET in bioimaging exploits the large spectral separation between excitation and emission, made possible by FRET that is much larger than usually observed for a single dye. As an example, the application of traditional NIR dyes for imaging is complicated by small Stokes shift resulting in self-quenching and a cross-talk between excitation and emission. The application of FRET to overcome the problem of small Stokes shift was demonstrated in Ref.[122] for methylene blue dye. Authors reported more than 200 nm Stokes shift for a RuBpy and methylene blue FRET pair with excitation at 465-495 nm and emission at 700 nm. Also by using appropriate $D-A$ pair the emission wavelengths may be tuned to the region of minimum background autofluorescence or to the tissue transparency window.

Although in most cases FRET relies on the detection of changes in the acceptor emission or on ratiometric measurements, the acceptor does not necessarily need to be fluorescent. Some of the applications exploit FRET to

quench the donor emission by transferring the excitation to a non-fluorescent dye. Molecular probes that are used for this purpose are called dark quenchers. As they are non-fluorescent, the spectral part that otherwise would have been otherwise occupied by the acceptor fluorescence can be used for additional fluorophores or even additional donor-quencher pairs.[123]

FRET finds myriad of applications in different fields, but it is important to know its main limitations:

- FRET is the dominant mode of energy transfer only in the limited range of distances of roughly 10-100 Å. At very short distances when r is close to the size of the molecule the interactions of higher multipolarity may contribute significantly to energy transfer. At longer distances $r > 100$ Å contributions to the interaction matrix element, that are neglected in the Förster theory become relevant,[124] and for even longer distances $r \sim \lambda$ radiation energy transfer occurs.[10],[117]
- The exact values of effective refractive index n and the orientational factor κ^2 in equation (4.2) are unknown in most cases.

4.3 Quatsomes for FRET. Preparation, characterization and optical properties

In Chapter 3 we showed that QS are appealing scaffolds for nanostructuration of different dyes in water. Here we develop this approach towards labelling QS with pair of dyes, and as a proof of concept we choose the DiI/DiD pair. The preparation procedure is similar to that described in Ref.[75],[77] but in this case the solution of two dyes in ethanol was used. Fluorescence spectrum of DiI (see Figure 4.4) shows a significant overlap with DiD absorption, suggesting the possibility to use the DiI/DiD pair for FRET with DiI acting as energy donor and DiD as energy acceptor.

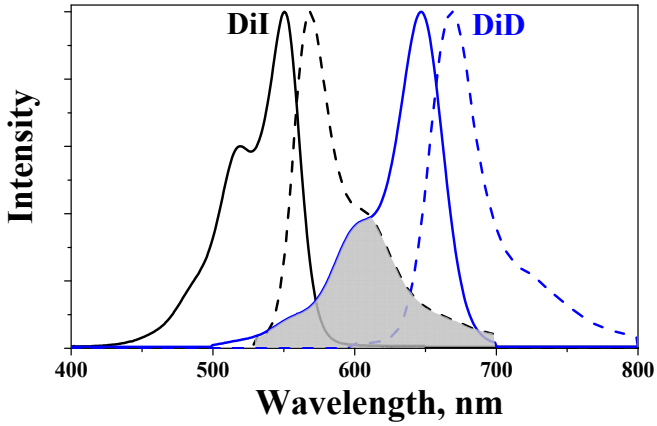

Figure 4.4 *DiI and DiD spectral overlap.*

Two different samples with different loadings and constant concentration ratio (1:1) of the dyes was were prepared: I,D-QS-1 and I,D-QS-5 (see Table 7). The choice was based on previous reports[125],[126] were the authors demonstrated close to 100% efficiency of FRET for polymeric nanoparticles doped with carbocyanine dyes taken in equimolar ratio.

Since Q_D, $I_D(\lambda)$ and $\varepsilon_A(\lambda)$ values that enter the equation (4.2) vary depending on the dye loading, FRET distances were calculated using corresponding values. Q_D, $I_D(\lambda)$ were taken for DiD-QS-1 and DiD-QS-5 samples and $\varepsilon_A(\lambda)$ values were taken for I-QS-1 and I-QS-5. Calculated Förster distances (see Table 7) are comparable with the QS membrane thickness, showing the possibility of energy transfer through bilayer between two dyes, located at the inner and outer interfaces of the membrane.

Samples prepared for FRET demonstrated similar colloidal properties and excellent long-term stability as other cyanine-labeled QS. Loading two dyes in QS does not affect the morphology of the nanoparticles, as it can be seen from the Cryo-TEM images (Figure 4.5). Size distribution, average diameter and absorbance of I,D-QS-1 and I,D-QS-5 remained stable at least within one month.

Table 7. Properties of I,D-QS.

Sample	Dye loading, L, 10^{-3}	Average diameter, nm	Förster distance R_0, nm
I,D-QS-1	0.7	102	56
ID-QS-5	7	138	60

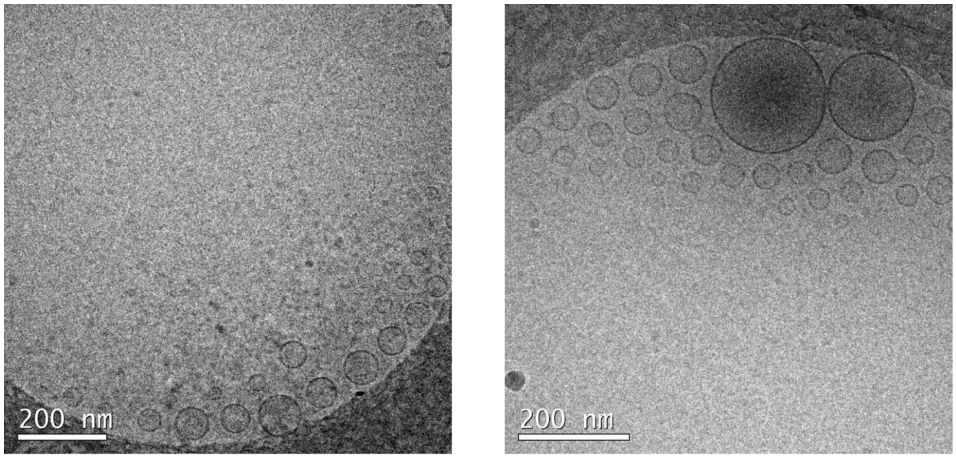

Figure 4.5 *CryoTEM images of I,D-QS-1 (left) and I,D-QS-5 (right)*

Linear absorption and fluorescence spectra of I,D-QS-1 and I,D-QS-5 compared with corresponding spectra of single dye-labeled and mixtures of single dye-labeled QS are shown in Figure 4.6. Absorption spectra of I,D-QS were normalized by maximum absorbance of DiD and absorption of spectra I-QS-5 and D-QS-5 were normalized to match peaks at 550 nm (maximum DiI absorption) and 647 nm (maximum DiD absorption) respectively.

Absorption spectra of I,D-QS contain two peaks, corresponding to absorption of DiI and DiD and can be represented as a sum of absorption spectra of single dye-loaded nanoparticles, demonstrating the successful encapsulation

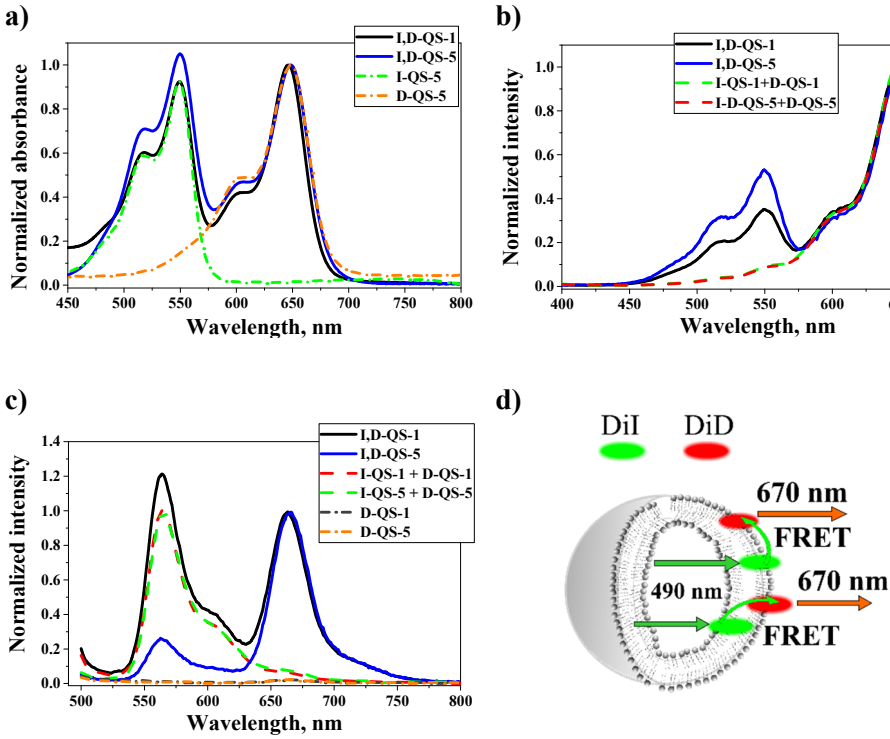

Figure 4.6 *a) Normalized absorption spectra of I,D-QS-1 and I,D-QS-5 and single dye-labeled QS (I-QS-5 and D-QS-5). b) Excitation spectra of I,D-QS-1 and I,D-QS-5 and of mixtures of single-dye labeled QS (I-QS-1+D-QS-1 and I-QS-5+D-QS-5). c) Fluorescence spectra of I,D-QS-1 and I,D-QS-5, and of mixtures of single-dye labeled QS (I-QS-1+D-QS-1 and I-QS-5+D-QS-5) and single-dye labeled QS (D-QS-1 and D-QS-5). d) A scheme demonstrating FRET between DiI and DiD in QS.*

of the two dyes in QS. Although molar ratio of two dyes was kept constant the ratio between maximum absorbance of DiD and DiI dyes in I,D-QS changes with the increasing loading. This fact is in agreement with observed DiD tendency to form non-fluorescent aggregates in D-QS at large loadings, as was discussed in Chapter 3.

Emission spectra of I,D-QS show clear evidence of energy transfer occurring between DiI and DiD in I,D-QS-1 and I,D-QS-5. Upon excitation at 490 nm, where the absorption of D-QS is negligible, the fluorescence spectra of I,D-QS exhibit two peaks due to the fluorescence of DiI under direct excitation and the fluorescence of DiD due to energy transfer, while the fluorescence of D-QS-1 and D-QS-5 under the same experimental condition was not detected (Figure 4.6 (c)). To check the possibility of FRET between dyes encapsulated in different nanoparticles the emission of mixtures I-QS-1+D-QS-1 and I-QS-5+D-QS-5 was also collected. Excitation at 490 nm leads only to the fluorescence of DiI at 565 nm, proving negligible FRET for these samples. This is also confirmed by excitation profiles of mixtures (I-QS-1+D-QS-1 and I-QS-5+D-QS-5) and I,D-QS. The excitation spectra of I,D-QS reveal two maxima, indicating that excitation of DiI gives rise to the DiD emission, that is absent in case of I-QS + D-QS mixture.

Relative emission intensity of DiD in I,D-QS-5 sample is much lower compared to the I,D-QS-1 sample. This quenching is explained by higher dye loading in I,D-QS-5, that results in smaller average distance between D and A molecules and higher energy transfer efficiencies. The efficiency of FRET was calculated based on comparison between absorption spectrum and corrected excitation spectrum collected in the emission maximum of the acceptor[10] $I_A(\lambda, \lambda_A^{fl})$

$$E_{FRET} = \frac{D_A(\lambda_A)}{D_D(\lambda_D)}\left(\frac{I_A(\lambda_D, \lambda_A^{fl})}{I_A(\lambda_A, \lambda_A^{fl})} - \frac{D_A(\lambda_D)}{D_D(\lambda_A)}\right) \qquad (4.6)$$

Here $D_A(\lambda_A)$ and $D_D(\lambda_D)$ are the maximum absorbance of donor and acceptor, λ_A and λ_D, respectively. As expected, the highest efficiency of FRET was observed in the sample with highest loading I,D-QS-5 $E_{FRET}^{(5)} = 60\%$ while for I,D-QS-1 $E_{FRET}^{(1)} = 40\%$.

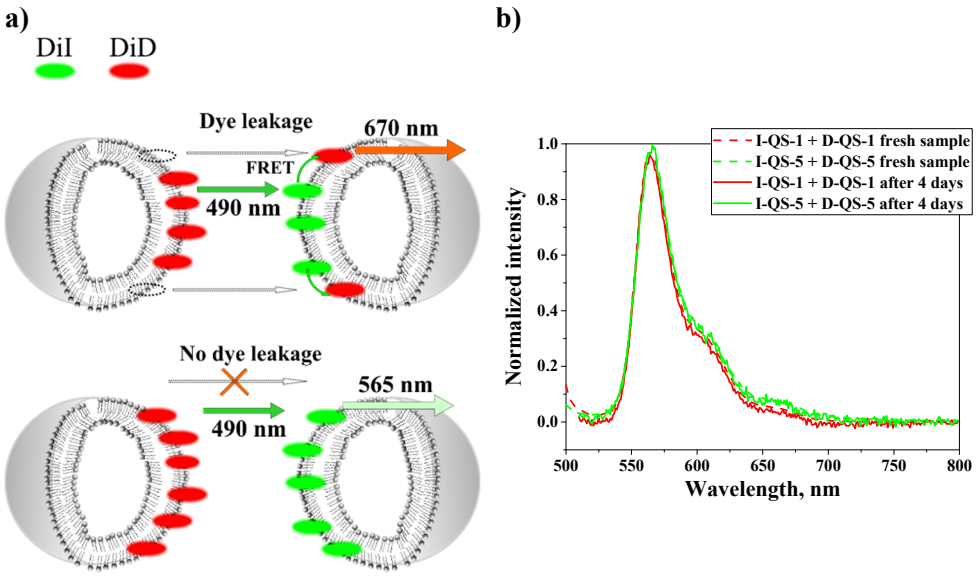

Figure 4.7 *a) Scheme of the encapsulation stability test of dye-loaded QS. b) Normalized fluorescence spectra of freshly prepared (dashed lines) I-QS-1+D-QS-1 and I-QS-5+D-QS-5 and 4 days after (solid lines).*

FRET can also serve as an additional tool to test encapsulation stability of guest molecules in QS. This parameter is especially important when QS are considered for delivery applications and potential leakage of the loading before the nanoparticles reach the target has to be prevented. To check the stability of DiD and DiI dyes in QS using FRET, fluorescence spectra of I-QS-1+D-QS-1 and I-QS-5+D-QS-5 mixtures were recorded at different times after the preparation.

Just after synthesis dyes are encapsulated in different nanoparticles and separated by a large distance, so no FRET signal is observed. In case of significant exchange dynamics DiD and DiI will be located in the same nanoparticle giving rise to FRET (see Figure 4.6 (a)). As it follows from Figure 4.7 (b) fluorescence spectra of samples remained stable with time, proving absence or at least negligible leakage of guest dyes from the membrane.

4.4 Conclusions

In this chapter we briefly discussed the energy transfer processes with focus on FRET process and provided a short overview of FRET theory and applications. The experimental section includes studies of optical properties and stability of QS loaded with two carbocyanine dyes - DiI and DiD. Significant spectral overlap between DiI emission and DiD absorption suggests utilizing this pair of dyes for FRET, with DiI as a donor and DiD as an acceptor. When the two dyes are encapsulated within the same bilayer highly efficient energy transfer is observed, as demonstrated by strong DiD emission upon excitation of DiI. The efficiency of FRET differs for the samples with different dye loading reaching efficiencies as high as 60%.

I,D-QS showed excellent colloidal stability and good dye encapsulation stability, as also demonstrated by FRET-based test that proved the absence of any leaking or dye exchange between particles. We underline that I,D-QS may be of interest for multicolor bioimaging: relevant nanoparticles in fact can be excited by the same light emitting in different spectral regions that can be detected simultaneously. This allows to get different images of the same spot upon a single measurement, increasing the sensitivity and the detail of the measurement.

5 QUATSOMES FOR BIOIMAGING

We have described so far fundamental studies of fluorene dyes, fluorene-based FONs and carbocyanine-loaded QS. We demonstrated the attractive optical properties of **s1** and **s2** dyes and showed the potential and flexibility of QS for solubilizing hydrophobic dyes. In this chapter, based on these data, we take a step towards the practical application of the studied fluorescent labels *in-vitro* in conventional fluorescent microscopy and in novel super-resolution stochastic optical reconstruction microscopy (STORM).

Fluorescent images with QS loaded with fluorene derivatives were obtained by Xinglei Liu in Prof. Kevin Belfield's group at New Jersey Institute of Technology. The STORM imaging was performed in the group of Dr. Lorenzo Albertazzi at the Institute de Bioingenieria de Catalunya.

5.1 Quatsomes loaded with fluorene derivative. Photophysics and colloidal properties

As previously discussed, the fluorene derivative **s1** is a bright and stable dye with a good potential for applications in photonics and specifically in bioimaging. In this respect its main limitation is hydrophobicity that makes it incompatible with biological media. In Chapter 2 we described a first attempt to overcome this issue nanostructuring **s1** in organic fluorescent nanoparticles obtained *via* reprecipitation method. Resulting nanoparticles showed adequate photostability and reasonable fluorescent quantum yield. To fully investigate the potential of **s1** its solubilization using QS as carriers was also studied. QS loaded with **s1** (**s1**-QS) were synthesized following a similar procedure as

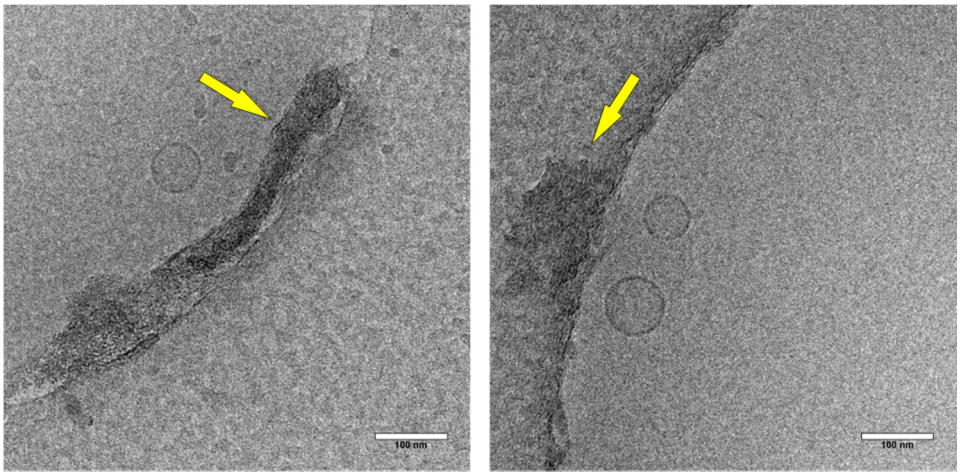

Figure 5.1 *Cryo-TEM images of **s1**-QS. Yellow arrows point to the aggregates of **s1** Scale bar in all images equals 100 nm.*

described in Chapter 3 for carbocyanine-loaded QS. Specifically, an ethanol solution of **s1** was loaded together with cholesterol in a high-pressure vessel and then QS were prepared according to the standard procedure.[75] Cryo-TEM images of **s1**-decorated QS in Figure 5.1 reveal the presence of unilamellar round vesicles coexisting with dark aggregates of irregular shape, which are attributed to **s1** aggregates. In spite of its hydrophobicity, **s1** does not bind to the membrane during QS formation, rather it forms separate aggregates similar to those obtained by reprecipitation.

a)

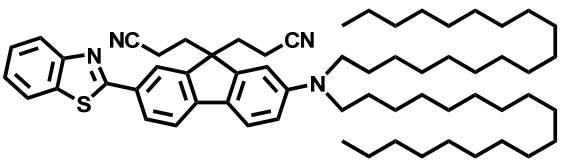

b)

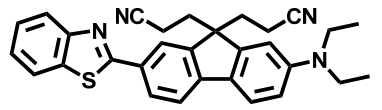

Figure 5.2 *Molecular structures of compounds DiC18 (a) and **s1** (b)*

Table 8. Main photophysical parameters of DiC18. Absorption λ_{max}^{abs} and emission λ_{max}^{fl} wavelengths maxima; ε_{max} - extinction coefficient at λ_{max}^{abs} and Q_{fl} – the fluorescence quantum yield.

Solvent	CHX	TOL	THF	DCM	ACN
λ_{max}^{abs}, nm	389	400	400	404	401
λ_{max}^{fl}, nm	422	447	482	503	532
ε_{max}, 10^3 M^{-1} cm^{-1}	52	46	44	40	44
Q_{fl}, %	92	100	85	100	100

Based on the success of solubilizing of carbocyanines with long aliphatic chains a modification of the structure of **s1** was proposed and performed in Prof. K. D. Belfield's group. 7-(benzo[d]thiazol-2-yl)-9,9-diethyl-N,N-dioctadecyl-9H-fluoren-2-amine (DiC18) is **s1** with added two long chains aiming to increase its lipophilicity (see Figure 5.2). Synthetic route is briefly summarized in Appendix A. Since the chromophoric part of the molecule remains intact, the photophysical properties of DiC18 in different solvents (see Table 8) are very close to those of **s1.**

Three samples of QS loaded with different amount of DiC18 were synthesized and characterized by Cryo-TEM and DLS. Cryo-TEM images in Figure 5.3 show that DiC18 does not affect the morphology and the lamellarity of QS. However Cryo-TEM revealed the presence of small dark "patches" attached to the surface of nanoparticles, either surrounded by membrane or freestanding. The composition of these patches is difficult to determine, as they may consist of either pure DiC18 or of mixture of DiC18 and membrane components (cholesterol and CTAB). For all loadings, QS bearing at most one "patch" of DiC18 were only detected. Cryo-TEM images of DiC18-QS-3

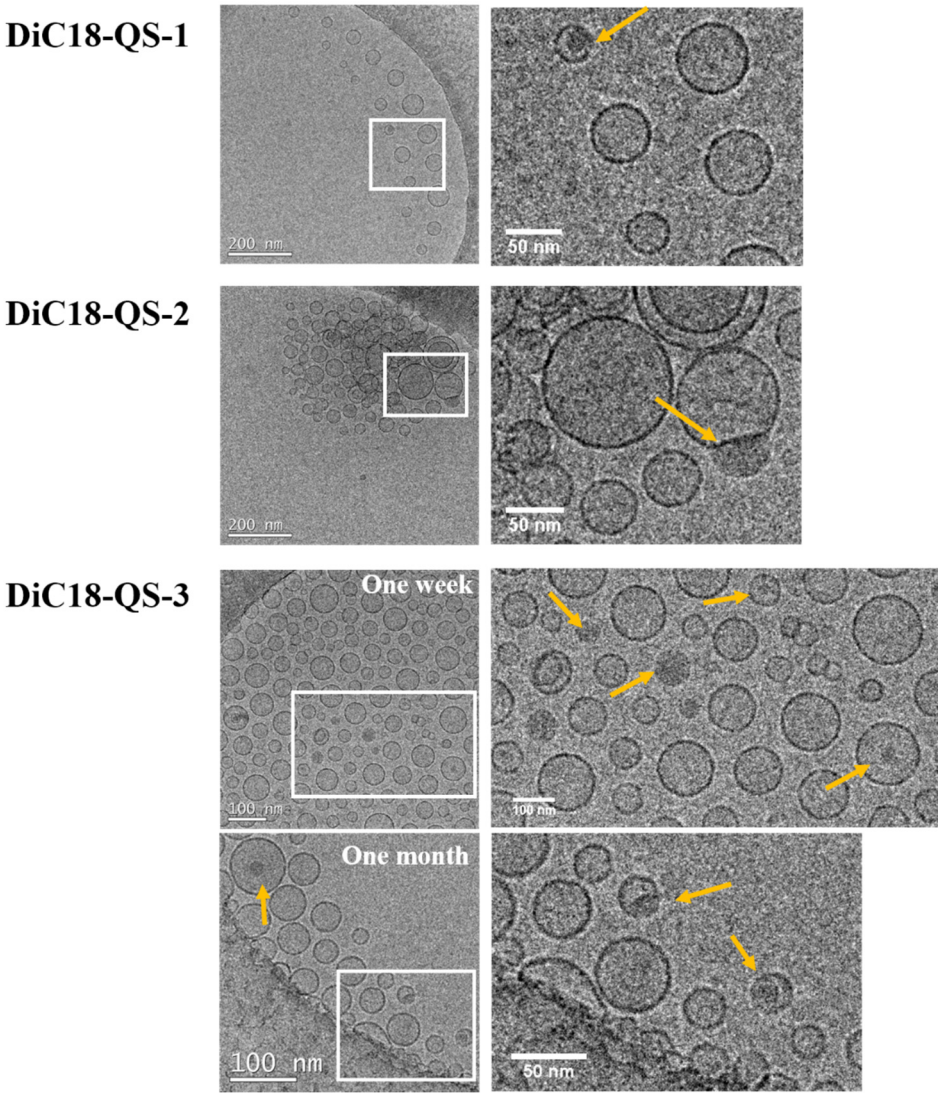

Figure 5.3 *Cryo-TEM images of DiC18-QS. Images in the right column are magnified views of the boxed regions in the left column. Yellow arrows point to the aggregates of* ***s1****.*

Table 9. Main colloidal parameters of QS loaded with fluorene derivative DiC18: dye loading [a]L; average diameter[b]; zeta potential ζ; absorption λ_{max}^{abs} and emission λ_{max}^{fl} wavelengths maxima; maximum extinction coefficient ε_{max} and the fluorescence quantum yield Q_{fl}.

Sample	L, 10^{-3}	Average diameter, nm	ζ, mV	λ_{max}^{abs}, nm	λ_{max}^{fl}, nm	ε_{max}, 10^3 M^{-1} cm^{-1}	Q_{fl}, %
DiC18-QS-1	0.9	70±38 / 73±35	86±20	392	452	39	46
DiC18-QS-2	7	58±30 / 55±28	78±27	394	455	40	37
DiC18-QS-3	13	60±32 / 60±30	75±18	394	461	36	21
s1$_{ONPs}$	-	165	-	413	512	33	10

[a] dye loading calculated using Equation (3.1)

[b] measured with DLS. Numbers before and after slash refer to the average diameters estimated one week and one month after synthesis respectively.

confirm the system stability within one month. The long-term stability of DiC18-QS was also monitored with DLS (see Table 9). The average hydrodynamic diameter did not change within one month after synthesis and the high positive zeta potential ensures high colloidal stability in all samples.

Table 9 collects main photophysical properties of DiC18-QS. Absorption, fluorescence and fluorescence excitation spectra are plotted in Figure 5.4. Increasing the loading of DiC18 leads to the effects similar to those expected for aggregation-caused quenching, with a decrease of the quantum yield and of molar extinction coefficient in line with what was observed for

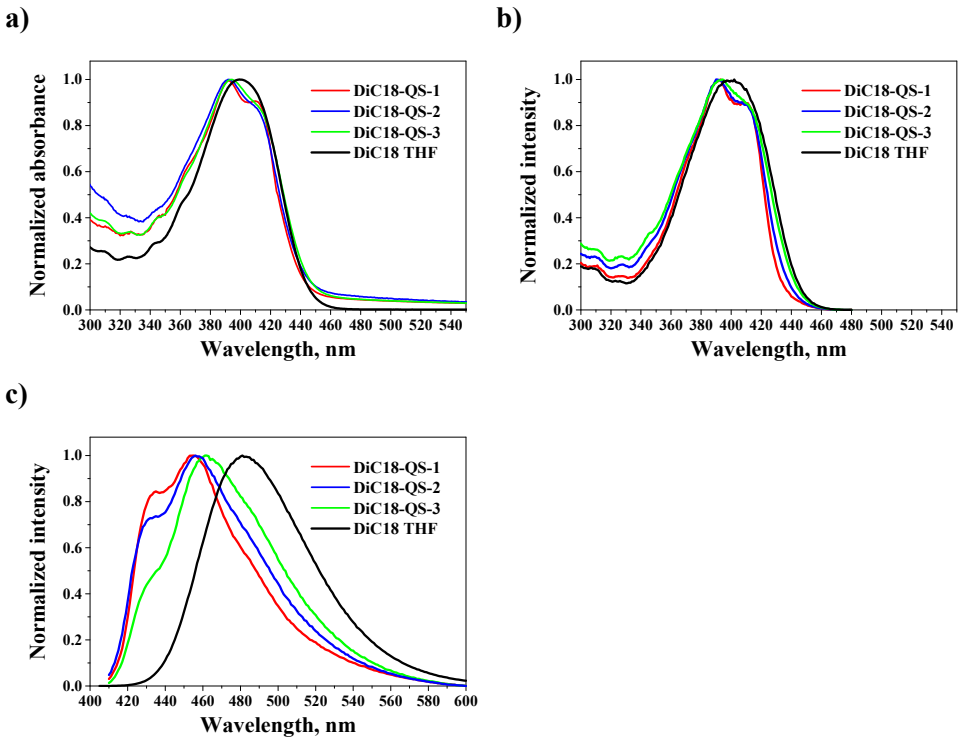

Figure 5.4 *Normalized absorption (a), fluorescence excitation (b) and fluorescence (c) spectra of DiC18-QS.*

Fl-QS and carbocyanine-loaded QS. The spectral position of absorption maxima of DiC18-QS do not show any noticeable change compared to free dye in organic solvents (see Table 8 and Table 9). Fluorescence spectra of DiC18 depend strongly on the solvents polarity and the fluorescence of DiC18 loaded QS in water is similar to what is measured in a medium polarity environment. Much as in the case of $\mathbf{s1}_{ONPs}$ (see Chapter 2) this is ascribed to the local environment of the fluorescent dye that is buried inside the aggregates and/or the QS membrane, corresponding to a much less polar environment than water.

5.2 Quatsomes loaded with fluorene derivative: bioimaging

In the previous section we demonstrated that **s1** derivative can be successfully solubilized in water using QS. Previous studies[127],[128],[129] show excellent performance of micelle-encapsulated hydrophobic dyes of fluorene family for linear and nonlinear bioimaging and therefore we tested the potential of DiC18-loaded quatsomes as probes for fluorescent labeling *in vitro*. The HCT116 (human colorectal carcinoma) cell line was used for all tests. It was demonstrated[129],[130] that some hydrophobic fluorene derivatives can be used for microscopy imaging if they are solubilized in 0.2-5 % DMSO in water solution. The control sample was prepared according to this approach as follows: HCT116 cells were incubated in 20 μM of DiC18 in 1% (vol) of DMSO in DMEM ((Dulbecco's Modified Eagle's Medium for supporting the growth of mammalian cells) for 2 hours. Samples of cells labeled with DiC18-QS-3 were prepared in the same way by diluting DiC18-QS-3 with DMEM and incubating with cells for 2 hours.

Stained cells were visualized by confocal laser scanning microscopy (60x, oil immersion objective, λ_{exc}=377 nm) and differential image contrast (DC) microscopy (see Figure 5.5). Fluorescence microscopy of DiC18 labeled HCT116 does not reveal any signal. Taking into account that **s1** forms fluorescent aggregates in water the lack of fluorescence in this sample can be attributed to the absence or extremely low cell uptake of pure DiC18. In contrast, bright fluorescence was observed in cells incubated with DiC18-QS-3 and, as shown in Figure 5.5 (e), a fluorescent signal is observed from the cells interior. This indicates a good uptake of QS by cancer cells, demonstrating strong potential of QS as nanocarriers of hydrophobic dyes for bioimaging *in vitro* and opening prospects for *in vivo* applications. The cell uptake is mediated by a passive intracellular delivery mechanism of QS inside the cells, mainly due to the endocytosis[127],[131]. It can be facilitated by functionalizing the surface of

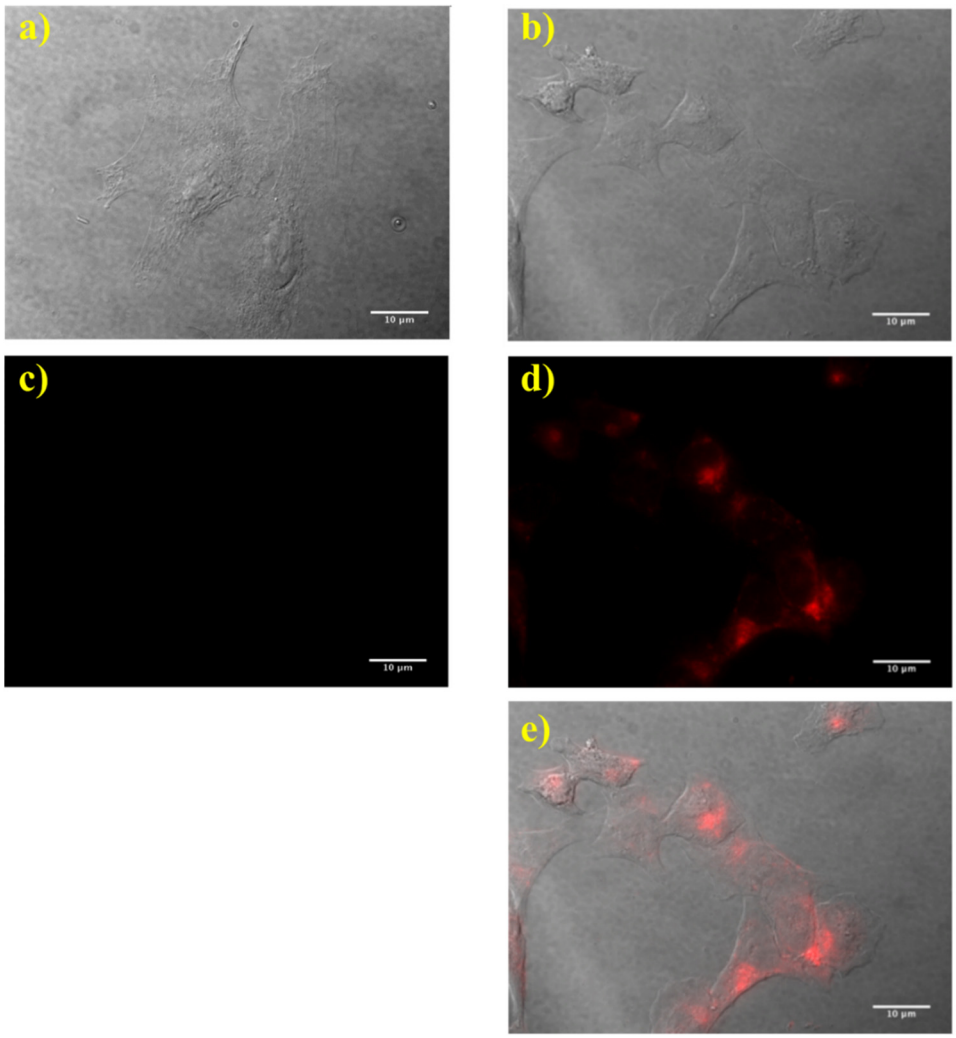

Figure 5.5 *Differential image contrast (a, b) and fluorescence microscopy (c, d) images of HCT116 cells stained with DiC18 (a, c) and DiC18-QS-3 (b, d, e). Image (e) shows an overlap of b and d. Scale bar in all images equals 10 µm.*

the nanoparticles[131] with cell-penetrating peptides or amphiphilic polymers. In this respect quatsomes are very interesting scaffolds offering different functionalization strategies.[74]

Although these preliminary studies demonstrate the possibility of using dye-labeled QS for cells staining, it is important to define the localization of these FONs inside the cells. A living cell is a very complex structure comprising various compartments and organelles. The simplest strategy to image them is staining using organelle-specific dyes, as, for example, nucleus-selective dyes (Hoechst, SYTO 9), lysosome- (LysoTracker Red) or mitochondria-specific (MitoTracker Red) fluorophores. The generally used strategy to define the localization of new fluorescent labels in living cells is the co-staining of cells with known organelle-specific dyes and checking the fluorescence signal colocalization in the images of the same sample. High degree of colocalization can prove the same staining pattern of studied labels.

The colocalization studies of free[132],[129] and micelle-encapsulated[128] fluorene derivatives as well as other FONs for bioimaging[131] show that these labels mostly demonstrate lysosomal staining activity. To reveal the labeling pattern of DiC18-QS-3 two sets of samples were prepared. First set include HCT116 cells co-stained with DiC-QS-3 and LT red, and the second set was co-stained with DiC-QS-3 and MT red.

Figure 5.6 shows fluorescent and DC images of co-stained cells demonstrating that the fluorescence distribution pattern of DiC18-QS-3 is different from that due to mitochondrial-specific dye MitoTracker red (MT red), showing low colocalization of DiC18-QS-3 with mitochondria. On the other hand, the analysis of fluorescent images of HCT116 cell images co-stained with lysosomal marker LysoTracker red (LT red) reveals strong visual correlation (Figure 5.6 (d)) with the intracellular distribution of DiC18-QS-3. That is indicative of lysosomal localization of DiC18-QS-3.

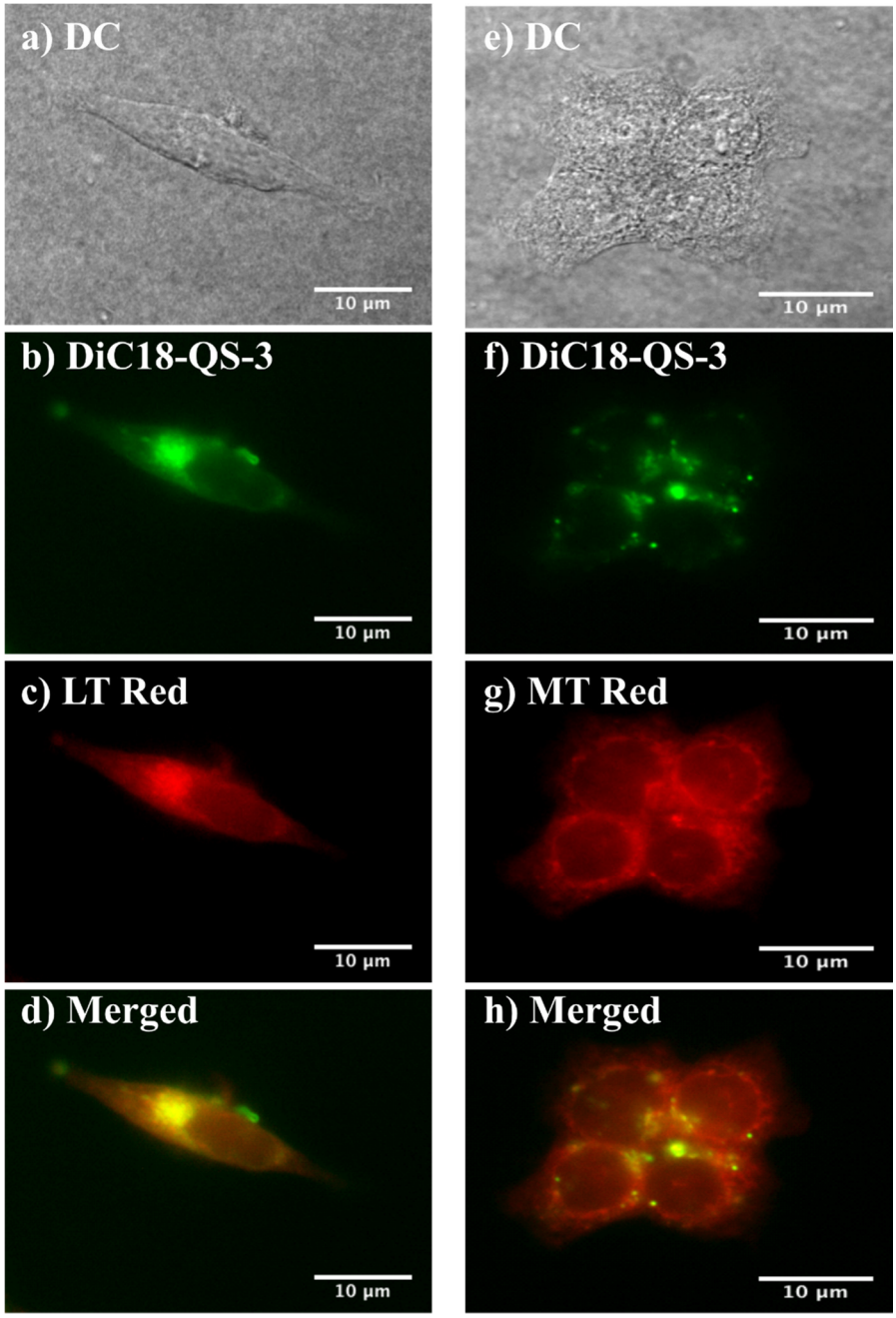

Figure 5.6 *DC (a, e) and fluorescence microscopy (b-d, f-h) images of HCT116 cells stained with DiC18-QS-3 (b, f, d, h), LT red (c) and MT red (g). Images (d) and (h) show an overlap of (b, c) and (f, g) respectively. Scale bar in all images equals 10 µm.*

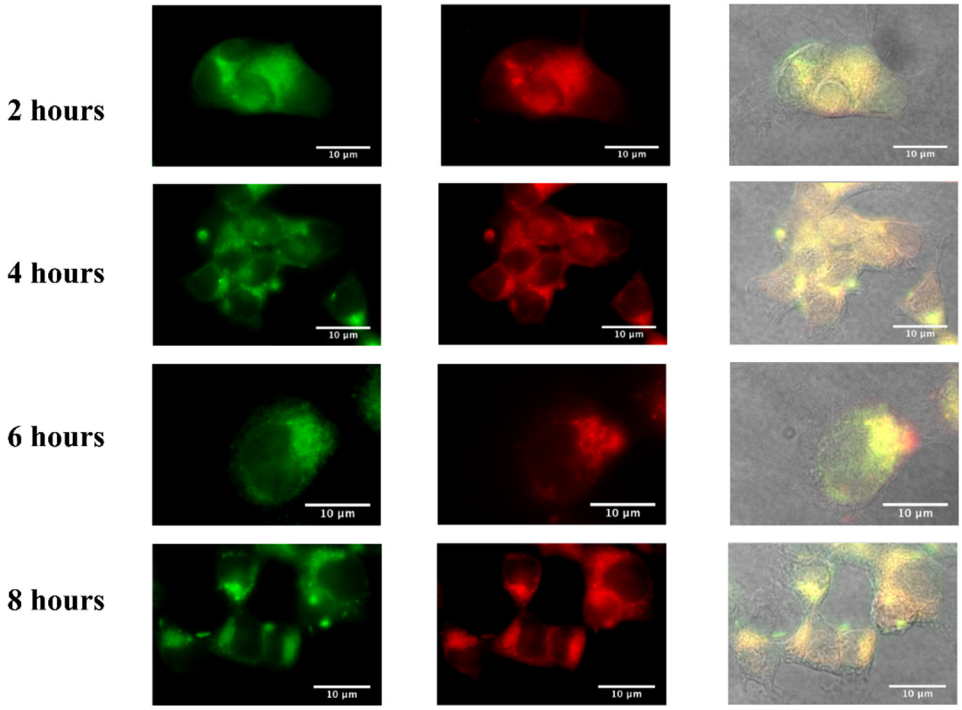

Figure 5.7 *Fluorescence microscopy (left and middle columns) images of HCT116 cells stained with DiC18-QS-3 (left column) and lysotracker red (middle column). Right column: overlapped fluorescent and DC images. Each row corresponds to the different incubation time (see legend). Scale bar in all images equals 10 µm.*

In Chapter 3 and 4 we demonstrated excellent long-term stability of QS loaded with various dyes. These experiments were conducted in ultrapurified MilliQ water, however the interior of a living cell is crowded with a large variety of macromolecules as well as with inorganic substances that interact in a complex way. Therefore the long-term stability of dye-labeled QS in biological environment was tested in four sets of samples. The initial step was the same as for colocalization studies: HCT116 cells were co-stained with DiC18-QS-3 and LT red, then after rinsing in phosphate-buffered saline cells were incubated in

DMEM for 2, 4, 6 and 8 hours respectively. Before imaging, the cells were again rinsed in phosphate-buffered saline

The fluorescent images in Figure 5.7, referring to HCT116 cells co-stained with DiC18-QS-3 and LR red do not show any loss in fluorescence signal after 8 hours of incubating. These results supports the idea of excellent stability of DiC18-QS not only in water but also inside the cells. The high degree of colocalization of DiC18-QS-3 and LT red is indicative of high specificity of DiC18-QS for lysosomal labeling, showing good prospects for DiC18-QS as lysosomal probes for long-term bioimaging.

5.3 Principles of stochastic optical reconstruction microscopy (STORM)

Conventional laser scanning confocal microscopy is a powerful tool in biological sciences, being noninvasive and flexible. Relevant resolution is limited to approximately 200 nm, as dictated by light diffraction. The diffraction limit, also known as Abbe limit[133], was first described by Ernst Abbe in 1873. It can be demonstrated using an example of two points observed in a microscope. Because of light diffraction at the edges of objective and lenses, a single point light source appears as a blurred spot (Figure 5.8), surrounded by diffraction rings, called Airy diffraction pattern. Consequently two point emitters can be resolved only if the distance between them is larger than roughly $\approx\lambda/2$, corresponding for most microscopes to ≈200 nm. Closer points are observed as a single spot and cannot be separated (see Figure 5.8).

In the past decades, several techniques emerged that “break” the diffraction limit opening new fluorescent “nanoscopy” methods or superresolution methods. They are based on different physical principles and include stochastic optical reconstruction microscopy (STORM), photoactivation localization microscopy, structured illumination microscopy and stimulated

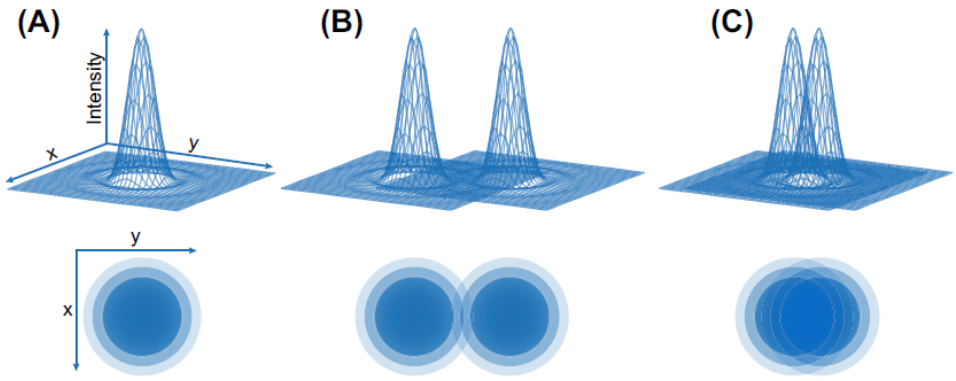

Figure 5.8 *Demonstration of spatial resolution of conventional laser scanning confocal microscopy. A) Intensity distribution of an emitting spot with subdiffraction size. B) Two spots can be resolved if their intensity distributions do not overlap. C) Two closely located emitters are resolved as a single spot. Reprinted from Ref.*[134]

emission depletion microscopy. One of the first demonstrations of sub-diffraction-limit bioimaging of filament of DNA with 20 nm was performed by M. Rust et al.[135] using cyanine 3 (Cy3) and cyanine 5 (Cy5), analogues of DiI and DiD carbocyanines, but without the alchyl chains. We have studied extensively the photophysical properties of cyanine-loaded QS (Chapter 3) and demonstrated the application of QS for conventional microscopy. Taking into account appropriate photophysical properties of cyanines for using them as fluorescent probes for STORM we explore the possibility of application of DiI- and DiD-QS for super-resolution bioimaging.

The basic principle of STORM technique is shown in Figure 5.9. It is based on single molecule detection and *a priori* knowledge that each detected diffraction-blurred spot is due to the fluorescence of a single fluorophore. From this knowledge the center of the diffraction-limited spot can be estimated with

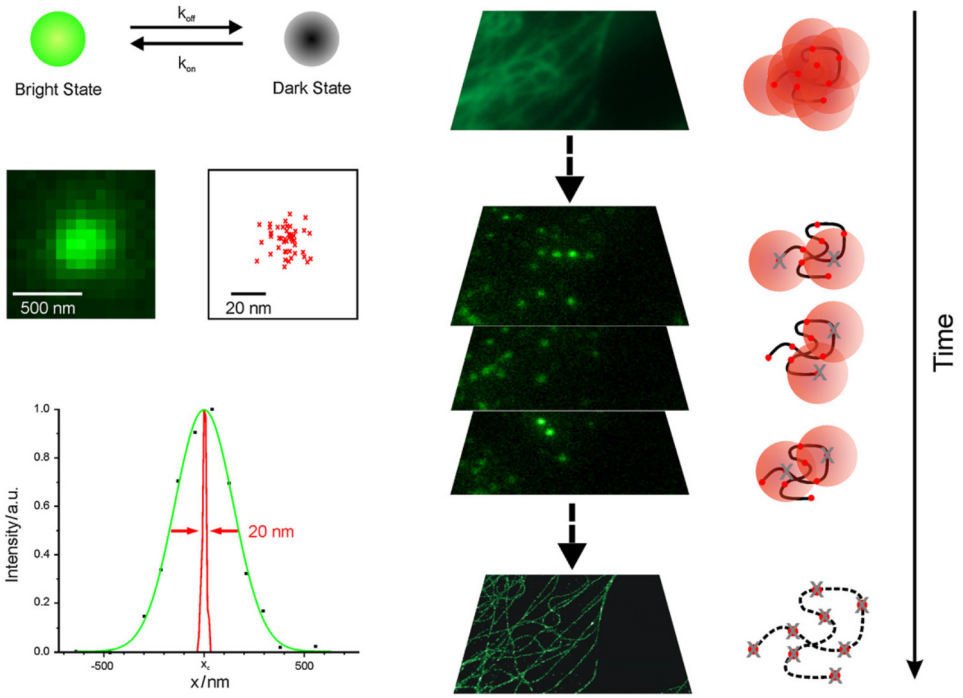

Figure 5.9 *Principles of STORM. Reprinted from Ref.[138] with permission of IOP Publishing.*

precision[134] proportional to the $\sim 1/\sqrt{N}$ where N is the number of collected snapshots. Resulting super-resolved image is obtained when the position of many fluorophores is determined (Figure 5.9). The major technical difficulty is to ensure that the signal comes from a single emitter. This can be achieved by labeling the sample very sparsely, what is undesirable because it does not give the full fluorescent image of the sample. The other approach is to collect fluorescence from a small subpopulation of labels, so that each fluorophore is distant from the other and their images do not overlap. In STORM this is achieved by switching the fluorophore from an emitting (bright) state to a non-emitting (dark) state. The first demonstration[135] of STORM was based on photoswitching of Cy5-Cy3 pair using two laser beams – a 633 nm was used to excite Cy5 and to switch it to the stable dark state, and 532 nm switched Cy5 back to the bright state. The Cy3 molecule located in vicinity (~1 nm) facilitated

the switching, however the role of the Cy3 molecule in the enhancement of Cy5 conversion efficiency from the dark to the bright state remains unclear.[136] Also, the conversion of Cy5 to the dark state upon reaction with thiol-containing compound and spontaneous reactivation (blinking) was observed.[137] This method is called direct STORM (dSTORM) and the rate of switching can be tuned by the concentration of thiol compounds and the irradiation intensity. In the work presented here no photoswitching laser line is used, and a single wavelength is used for excitation.

Three important properties of STORM can be underlined:

1. with increasing the number of collected snapshots there is no theoretical limit to the resolution, for example even 100 collected snapshots lead to the resolution 10 times below the diffraction barrier;
2. a suitable fluorescent label must emit as many photons as possible before bleaching, therefore photostability of the probe is of ultimate importance for obtaining high quality super-resolved images;
3. because STORM image is reconstructed from a stack of multiple fluorescent images of small subpopulation of excited fluorophores the time resolution of this method is low, typically ranging from hundreds of milliseconds to tens of seconds.

Importantly, STORM as compared with e.g. STED does not require intense laser beams and it can serve as a noninvasive tool to study interaction inside living cells with nanometer-scale resolution.[140],[134] An example comparing confocal microscopy with STORM is shown in Figure 5.10. As it can be seen the greatly enhanced resolution of STORM allows resolving the densely packed mitochondria and microtubules

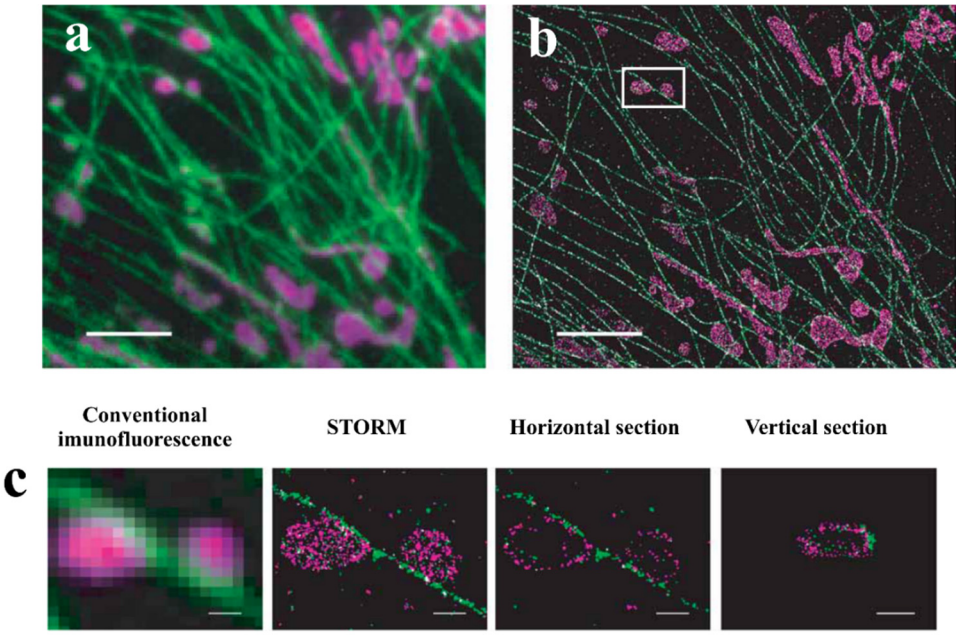

Figure 5.10 *Bioimaging of mitochondria and microtubules. a) Conventional confocal microscopy image of mitochondria (magenta) and microtubules (green). b) STORM image of the same area. c) Magnified view of boxed region in a) Scale bars equal 3 μm in (a, b) and 500 nm in (c) Adapted from Ref.*[140] *by permission from Macmillan Publishers Ltd.*

5.4 Quatsomes loaded with cyanines as probes for STORM

As discussed in the previous section, carbocyanine dyes have appropriate photophysical properties for STORM application. Here we demonstrate the applicability of carbocyanine-loaded QS for superresolution bioimaging. STORM images were acquired with Nikon N-STORM system using 561 nm laser for I-QS excitation and 647 nm for D-QS excitation.

The first step was visualizing single QS and single chromophores on the surface of QS. The Cryo-TEM images (Chapter 3) show that the QS diameter is mostly ≤ 100 nm – far below the diffraction limit, therefore QS imaging can

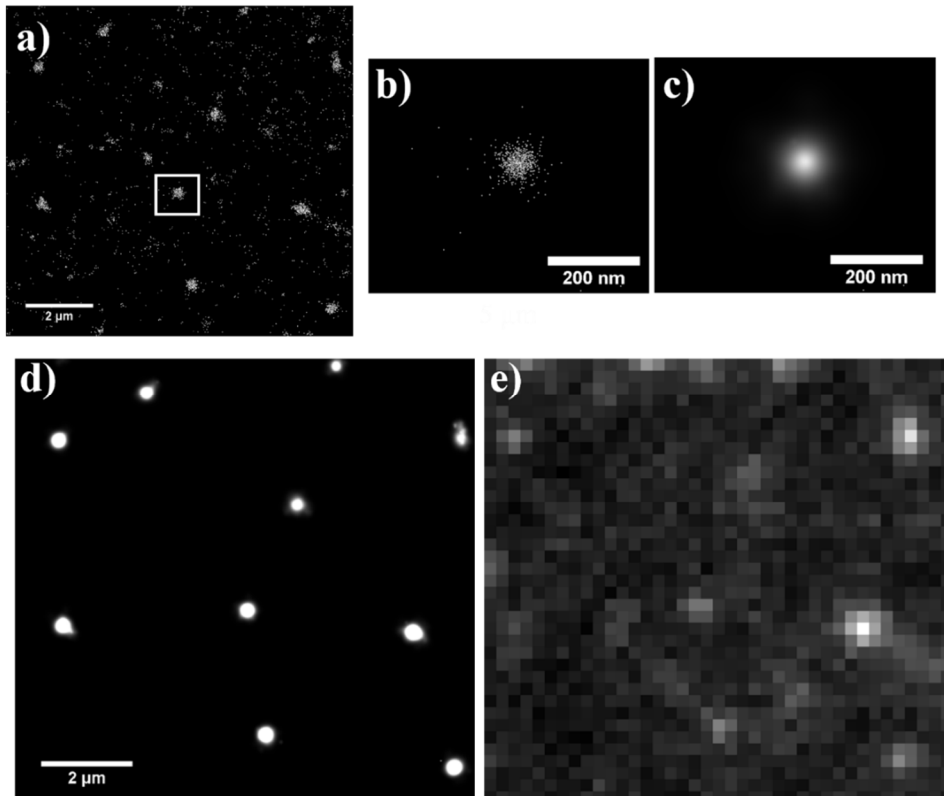

Figure 5.11 *(a-d) STORM imaging of I-QS-1. White dots (a, b) correspond to reconstructed single DiI molecules positions. b) Magnified view of boxed region in (a). (c, d) STORM imaging of a single I-QS-1. e) Wide-field image of QS*

serve as a good demonstration of potential of STORM. Positively charged QS were attached to the negatively charged surface of glass simply by dropping a solution of I-QS-1 onto a glass slide. Then the glass slide was washed twice in MilliQ water and twice in the STORM buffer solution, containing cysteamine and oxygen scavenger. Cysteamine is an aminothiol compound necessary to enhance the spontaneous blinking of DiI and DiD. 20000 frames with 10 ms integration time were collected to reconstruct each image.

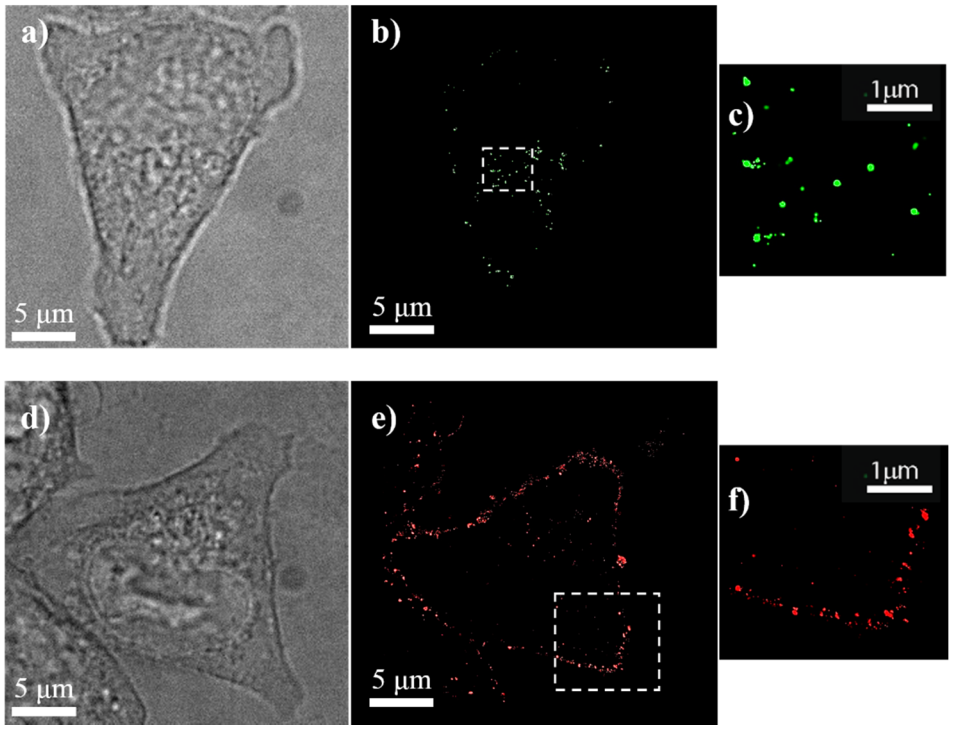

Figure 5.12 *DC (a, d) and STORM (b, c, e, f) images of HeLa cells stained with I-QS-1 (a-c) and D-QS-1 (d-f). c) and f) show magnified views of corresponding boxed regions*

Shown in Figure 5.11 are STORM images of I-QS-1. Single DiI molecules inside the QS membrane were clearly resolved (bright spots in Figure 5.11 (a, b)). The distribution of fluorophores is quite uniform, with no evidence of large aggregates. A single QS can be visualized by summing up all signal arising from each separate DiI molecule and fitting with a single two-dimensional Gaussian distribution (Figure 5.11 (c, d)). The separate QS were resolved as bright spots approximately 100-120 nm in diameter, in good agreement with Cryo-TEM results reported in Chapter 3. Compared with wide-field microscopy (Figure 5.11 (e)) STORM imaging of QS provides not only the

sub-diffraction spatial resolution, but also a highly enhanced contrast. As a result of images processing in STORM the background signal is nearly negligible.

We have already demonstrated the successful uptake of QS by cancer cells. Here we tested the applicability of cyanine-loaded QS for super-resolution bioimaging *in vitro*. HeLa cells were stained with I-QS-1 and D-QS-1 and visualized by means of DC and STORM (see Figure 5.12). Surprisingly, despite of similar structure of two dyes and exactly the same structure of QS, I-QS-1 and D-QS-1 exhibit different labeling patterns. I-QS are internalized by a HeLa cell and distributed inside. Magnified view in Figure 5.12 (c) reveals separated round dots meaning that QS do not aggregate inside the cell. The staining pattern of D-QS-1 corresponds to the cell membrane and irregular shaped aggregates are observed in the magnified view in Figure 5.12 (f). Considering the lipophilic nature of DiD, the dye might leave the QS and label the HeLa cell membrane upon the process of D-QS uptake.

5.5 Conclusions

Chapter 6 concludes the thesis demonstrating the potential of dye-labeled quatsomes as fluorescent probes for conventional fluorescence and superresolved STORM microscopies. The attempt of loading QS with fluorene derivative **s1** was not successful, as the dye forms aggregates and was not dispersed in the membrane. To enhance the solubility of **s1** in the membrane new lipophilic derivative of **s1** with two long alkyl chains, DiC18, was synthesized. DiC18 was successfully loaded in the membrane and fluorene-based DiC18-QS show similar colloidal properties and excellent long-term stability.

DiC18-QS were applied for *in vitro* labeling of HCT116 cancer cells and the colocalization studies of DiC18-QS with organelle-specific dye showed high specificity of DiC18-QS for lysosomal labeling. Long-term imaging

demonstrated that DiC18-QS have good stability in physiological conditions what makes them appealing probes for bioimaging of lysosomes in cancer cells.

Further we tested the cyanine-loaded D-QS and I-QS as fluorescent probes for superresolution microscopy. We started with demonstrating the ability of STORM to resolve single DiI molecules on the surface on QS. Consequently, summing up the signals of DiI single QS were clearly resolved. Next step was STORM imaging of cancer HeLa cells labeled with D-QS and I-QS. Surprisingly, D-QS and I-QS show different staining patterns, while I-QS are uptaken by cells D-QS staining pattern corresponds to cells membrane.

This chapter shows that QS are versatile, biocompatible and flexible scaffolds that can be loaded with variety of dyes and have great potential as fluorescent labels for fluorescent and STORM imaging.

CONCLUSIONS AND PERSPECTIVES

This thesis describes a path from fundamental experimental and theoretical studies of optical response and photostability of dyes and organic nanoparticles to their practical applications in FRET and bioimaging.

We started with characterization of two newly synthesized quadrupolar dyes of fluorene family **s1** and **s2**. Both dyes are highly fluorescent in the blue-green part of the spectra. **s1** was found to have good photostability in the solvents of low-to-medium polarity, however the photodecomposition quantum yield of **s2** is higher that usually observed for fluorene derivatives. For **s1** and **s2** in polar solvents pump-probe experiments revealed gain within the fluorescence bands that was further used for light amplification experiments. Using pump-probe based STED method we have estimated the STE cross-sections σ_{10} for both fluorenes and found that the maximum values σ_{10}^{max} deviated from corresponding 1PA cross-sections. Time-resolved STED dynamics of **s1** and **s2** was consistent with pump-probe data. Despite of success of STED microscopy the number of fundamental studies of STED processes in organic molecules is quite limited. Therefore, there is a need for comprehensive and consistent studies of STE cross-sections in different families of dyes to elaborate structure-property relationships and understand the role of environmental effects in STED. These data is important to guide the synthesis of new optimized probes for STED microscopy.

To reveal the role of symmetry and interplay between solvent effects and vibrational coupling, particularly in two-photon absorption and two-photon excited anisotropy spectra, we used essential-state modeling. The predictive power of ESM is impressive: once parameterized using linear absorption and

fluorescence spectra the model is able to reproduce 2PA spectra, linear and two-photon excited anisotropy spectra.

The hydrophobic nature of **s1** and **s2** makes difficult their direct application for bioimaging. We used a simple reprecipitation method to disperse **s1** and **s2** in water in form of ONPs. Aggregation of **s2** almost completely eliminate its fluorescence, however for **s1** reprecipitation yielded fluorescent, photostable and two-photon active ONPs.

A more versatile approach to the preparation of fluorescent organic nanoparticles is based on quatsomes - stable, water-soluble, cholesterol-rich unilamellar vesicles - as carriers. In this respect three strategies were presented. The first amounts to decorating the outer positively charged surface of the QS membrane with anionic dye. We used fluorescein for these tests. The nanostructuration of fluorescein on QS improved its photostability although the fluorescence quantum yield of Fl-QS decreased compared to the free dye. The second strategy went with the encapsulation of lipophilic carbocyanines inside the QS membrane. Three hydrophobic carbocyanine dyes (DiI, DiD and DiR) covering the yellow to NIR part of the spectrum were successfully solubilized in water using QS as carriers. Although aggregation of cyanines led in some cases to fluorescence quenching, the 2PA cross-section of D-QS was concentration-independent. The photostability of carbocyanine-loaded QS decreased compared to the free dyes in ethanol, but D-QS were found to be much more photostable than other surfactant-based micelle formulation of DiD in water. The third strategy consisted in substituting cholesterol with fluorescent sterol bearing NBD-6 dye. Similarly with the previous two cases, a concentration dependent quenching of fluorescence was observed however the photostability of N-QS was the same as of free NBD-6 cholesterol. All studied sample exhibit excellent long-term stability – no significant changes in hydrodynamic diameter and zeta-potential were observed within two months. As verified by CryoTEM attachment to the membrane or encapsulation of dyes and fluorescent sterol had no effect on the QS structure and lamellarity.

Inspired by successful solubilization of hydrophobic carbocyanines using QS as carriers we tested the possibility of simultaneous loading of two dyes in the membrane. The spectral overlap of DiI fluorescence and DiD absorption suggested a possibility of resonance energy transfer between them. Indeed, efficient FRET from DiI to DiD was observed when these two chromophores were simultaneously encapsulated in QS. High efficiency of energy transfer opens the possibility of creating cascade FRET with three or more chromophores proving that QS have great interest for multiplexing and multicolor bioimaging.

Based on the data collected for **s1** and attractive properties of dye-loaded quatsomes we made an attempt of creating **s1**-loaded nanoparticles. Despite of its hydrophobicity **s1** cannot be encapsulated in the membrane, but we succeed to create fluorene-loaded DiC18-QS only with lipophilic derivative of **s1**. *In vitro* fluorescence microscopy experiments showed that DiC18-QS have good uptake by tumor HCT116 cells and exhibit excellent stability in physiological conditions. Colocalization studies revealed specificity of DiC18-QS for lysosomes over other cell organelles.

Knowing that the first demonstration of sub-diffraction imaging by STORM was performed using Cy5 and Cy3, which have the same chromophoric part as DiI and DiD, we attempted to apply I-QS and D-QS for superresolution microscopy. With STORM we were able to visualize single QS and as well as single chromophores in the membrane. Imaging of HeLa cells incubated with cyanine-loaded QS revealed different staining patterns for D-QS and I-QS: while D-QS stained the cell membrane, I-QS were uptaken by the tumor cells.

The QS membrane can be functionalized for site-specific labeling, what together with different strategies of encapsulating dyes and utilizing (cascade) FRET make dye-loaded QS highly promising probes for bioimaging and theranostic applications.

APPENDIX A. MATERIALS

Solvents and commercial dyes

All used solvent were of spectroscopic grade. Water was Milli-Q purified grade (resistance 18.5 MΩ·cm, total organic carbon <5 ppb) from Milli-Q A10 (Millipore) apparatus. Carbocyanine dyes 1,1'-dioctadecyl-3,3,3',3'-tetramethyl-indocarbocyanine perchlorate (DiI), 1,1'-dioctadecyl-3,3,3',3'-tetramethyl-indodicarbocyanine perchlorate (DiD), 1,1'-Dioctadecyl-3,3,3',3'-tetramethylindotricarbocyanine iodide (DiR) were purchased from Life Technologies (Carlsbad, USA). 5-cholesten-3β-ol 6-[(7-nitro-2-1,3-benzoxadiazol-4-yl)amino]caproate (NBD6 cholesterol) was supplied by Avanti Polar Lipids (Alabama, USA)

Synthesis of 2,2'-((1E,1'E)-(9,9-diethyl-*9H*-fluorene-2,7-diyl)bis(ethene-2,1-diyl))bis(1-methyl-1H-pyrrole) (s2)

A mixture of 2,7-bis(bromomethyl)-9,9-diethyl-*9H*-Fluorene (1.5 g, 3.7 mmol) (prepared according to Ref.[141]) and triethyl phosphite (5 mL) was reflux for 2 hours under N_2. Excess triethyl phosphite was distilled under reduced pressure. The residue was dried under vacuum and used directly for the Horner-Emmons reaction. The intermediate was dissolved in dry N,N-dimetilformammide (10 mL), followed by slow addition of NaH (1.76 g, 73.3 mmol). The mixture was reacted under N_2 atmosphere at room temperature for 1 hour, followed by addition of 1-methyl-1H-pyrrole-2-carbaldehyde (0.8 g, 7.3 mmol). The mixture was then stirred overnight at room temperature. Water was added and the precipitate was collected by filtration, carefully washed with

water and dried. The crude product was purified by column chromatography with hexane/dichloromethane 2:1 as eluent. A yellow powder was obtained (1.09 g, 69%). m.p. 223-224 ºC. ^{1}H NMR (500 MHz, $CDCl_3$) δ: 7.62 (d, *J* = 7.9 Hz, 2H), 7.43 (d, *J* = 9.3 Hz, 2H), 7.37 (s, 2H), 7.01 (d, *J* = 16.2 Hz, 2H), 6.95 (d, *J* = 16.2 Hz, 2H), 6.64 (m, 2H), 6.50 (m, 2H), 6.17 (m, 2H), 3.73 (s, 6H), 2.07 (q, *J* = 7.3 Hz, 4H), 0.37 (t, *J* = 7.3 Hz, 6H). ^{13}C NMR (125 MHz, $CDCl_3$) δ: 150.61, 140.56, 136.72, 132.28, 126.66, 125.01, 123.55, 120.32, 119.70, 116.30, 108.30, 106.67, 55.98, 34.23, 32.91, 8.61. HRMS (APCI) for $C_{31}H_{32}N_2$ theoretical *m/z* $[M+H]^+$=433.2638, found $[M+H]^+$=433.2633

Synthesis of 7-(benzo[d]thiazol-2-yl)-9,9-diethyl-N,N-dioctadecyl-9H-fluoren-2-amine (DiC18)

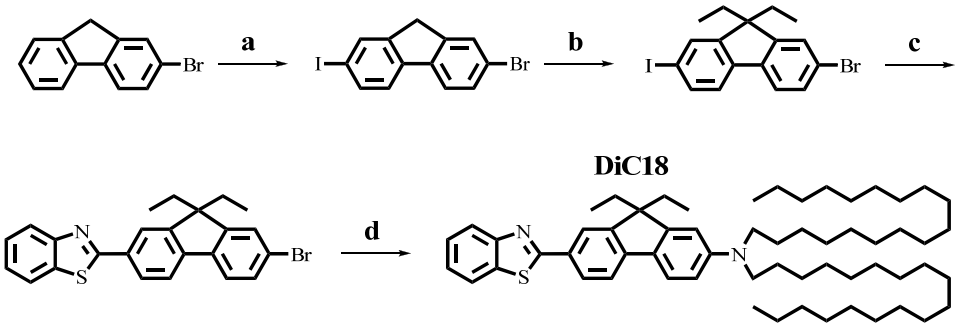

(a) I_2, KIO_3, HOAc, H_2SO_4, H_2O, 100 °C, 2 h, 80%;

(b) bromoethane, KI, KOH, DMSO, room temperature, 12 h, 73%;

(c) 2-(tri-n-butylstannanyl)benzothiazole, $Pd(PPh_3)_4$, toluene, reflux, 8 h, 43%; (d) dioctadecylamine, $Pd(OAc)_2$, $(t\text{-}Bu)_3P$, t-BuONa, toluene, reflux, 16 h, 84%.

REFERENCES

[1] Ostendorf and B. N. Chickov BN, *Photonics Spectra,* 2006, 40, 72–80

[2] C. O. Yanez, A. R. Morales, X. Yue, T. Urakami, M. Komatsu, T. A. H. Järvinen and K. D. Belfield, *PLoS ONE,* 2013, 8, e67559

[3] P.-P. Yang, Y. Yang, Y.-J. Gao, Y. Wang, J.-C. Zhang, Y.-X. Lin, L. Dai, J. Li, L. Wang and H. Wang, *Adv. Optical Mater.,* 2014, 3, 646–651

[4] M. Göppert-Mayer, *Ann. Phys.*, 1931, 401, 273–294

[5] W. Kaiser and C. G. B. Garrett, *Phys. Rev. Lett.,* 1961, 7, 229–231

[6] M. Pawlicki, H. A. Collins, R. G. Denning and H. L. Anderson, *Angew. Chem., Int. Ed.,* 2009, 48, 3244–3266.

[7] S. W. Hell and J. Wichmann, *Opt. Lett.,* 1994, 19, 780–782

[8] U. Resch-Genger, M. Grabolle, S. Cavaliere-Jaricot, R. Nitschke and T. Nann, *Nat. Methods*, 2008, 5, 763–775

[9] J. R. Lakowicz, *Principles of fluorescence spectroscopy*, Springer, 3rd ed., 2006

[10] B. Valeur, *Molecular fluorescence: principles and applications*, Wiley-VCH, Weinheim, 2002

[11] A. M. Brouwer, *Pure Appl. Chem*., 2011, 83, 2213–2228

[12] M. Sheik-Bahae, A. A. Said, T. Wei, D. J. Hagan and E. W. Van Stryland, *IEEE J. Quant. Electron.,* 1990, 26, 760–769

[13] W. Zhao and P. Palffy-Muhoray, *Appl. Phys. Lett.,* 1994, 65, 673–675

[14] S. Hughes and J. M. Burzler, *Phys. Rev. A*, 56, R1103–R1106

[15] G. Tsigaridas, M. Fakis, I. Polyzos, M. Tsibouri, P. Persephonis and V. Giannetas, *J. Opt. Soc. Am. B,* 2003, 20, 670–676

[16] E. W. Van Stryland, M. Sheik-Bahae, A. A. Said and D. J. Hagan, *Proc. SPIE*, 1993, 1852*,* 135–150

[17] C. Xu and W. W. Webb, *J. Soc. Opt. Am. B,* 1996, 13, 481–491

[18] N. S. Makarov, M. Drobizhev and A. Rebane, *Opt. Express*, 2008, 16, 4029–4047.

[19] J. R. Lakowicz and I. Gryczynski in *Topics in fluorescence spectroscopy. Volume 5: nonlinear and two-photon-induced fluorescence*, ed. J. R. Lakowicz, Kluwer Academic Publishers, 2002, pp. 87–144

[20] P. R. Callis, *J. Chem. Phys.*, 1993, 99, 27–37

[21] D. A. Armoogum, R. J. Marsh, N. Nicolaou, O. Mongin, M. Blanchard-Desce and A. J. Bain, *Proc. SPIE*, 2008, 7030, 70300S-1–70300S-10

[22] R. J. Marsh, N. D. Leonczek, D. A. Armoogum, L. Porres, O. Mongin, M. Blanchard-Desce and A. J. Bain, *Proc. SPIE,* 2004, 5510,117–128

[23] K. D. Belfield, M. V. Bondar, A. R. Morales, L. A. Padilha, O. V. Przhonska and X. Wang, *ChemPhysChem.*, 2001, 12, 2755–2762

[24] K. D. Belfield, M. V. Bondar, A. R. Morales, X. Yue, G. Luchita, O. V. Przhonska and O. D. Kachkovsky, *ChemPhysChem.*, 2012, 13, 3481–3491

[25] K. D. Belfield, M. V. Bondar, C. O. Yanez, F. E. Hernandez and O. V. Przhonska, *J. Phys. Chem. B,* 2009, 113, 7101–7106

[26] J. R. Lakowicz and I. Gryczynski in *Topics in Fluorescence Spectroscopy. Volume 5: nonlinear and two-photon-induced fluorescence,* ed. J. R. Lakowicz, Kluwer Academic Publishers, 2002, pp. 305–360

[27] C. Kallinger, S. Riechel, O. Holderer, U. Lemmer, J. Feldmann S. Berleb, A. G. Mückl and W. Brütting, *J. Appl. Phys.,* 2002, 91, 6367–6370

[28] O. Svelto, *Principles of lasers*, Springer, 5th ed., 2010

[29] C. Eggeling, J. Widengren, R. Rigler and C. A. M. Seidel, in *Applied fluorescence in chemistry, biology and medicine.* ed. W. Rettig, B. Strehmel, M. Schrader and H. Seifert, Springer, Berlin, 1999, pp. 193–240

[30] G.H. Patterson and D. W. Piston, *Biophys. J.,* 2000, 78, 2159–2162

[31] T. Jokic, S. M. Borisov, R. Saf, D. A. Nielsen, M. Kühl and I. Klimant, *Anal. Chem.,* 2012, 84, 6723–6730

[32] S. Zhang, T. Wu, J. Fan, Z. Li, N. Jiang, J. Wang, B. Dou, S. Sun, F. Song and X. Peng, *Org. Biomol. Chem.,* 2013, 11, 555–558

[33] K. D. Belfield, M. V. Bondar, Y. Liu and O. V. Przhonska, *J. Phys. Org. Chem.,* 2003, 16, 69–78

[34] S. A. Kurhuzenkau, A. W. Woodward, S. Yao, K. D. Belfield, Y. O. Shaydyuk, C. Sissa, M. V. Bondar and A. Painelli, *Phys. Chem. Chem. Phys*., 2016, 18, 12839–12846

[35] S. Yao, K. J. Schafer-Hales and K. D. Belfield, *Org. Lett.,* 2007, 9, 5645–5648

[36] F.Terenziani, A. Painelli, C. Katan, M. Charlot and M. Blanchard-Desce, *J. Am. Chem. Soc.,* 2006, 128, 15742–15755

[37] S. J. Strickler and R. A. Berg, *J. Chem. Phys.,* 1962, 37, 814–822

[38] K. D. Belfield, M. V. Bondar, A. R. Morales, X. Yue, G. Luchita and O. V. Przhonska, *J. Phys. Chem. C*, 2012, 116, 11261−11271

[39] K. D. Belfield, S. Yao and M. V. Bondar *in Photoresponsive Polymers I,* ed. S. R. Marder, K. S. Lee, Springer, 2008, pp 97-156

[40] K. D. Belfield, C. D. Andrade, C. O. Yanez, M. V. Bondar, F. E. Hernandez and O. V. Przhonska, *J. Phys. Chem. B,* 2010, 114, 14087–14095

[41] K. D. Belfield, M. V. Bondar, F. E. Hernandez, O. V. Przhonska and S. Yao, *J. Phys. Chem. B,* 2007, 111, 12723–12729

[42] K. D. Belfield, M. V. Bondar, F. E. Hernandez, A. E. Masunov, I. A. Mikhailov, A. R. Morales, O. V. Przhonska and S. Yao, *J. Phys. Chem. C,* 2009, 11, 4706–4711

[43] K. D. Belfield, M. V. Bondar, S. Yao, I. A. Mikhailov, V. S. Polikanov and O. V. Przhonska, *J. Phys. Chem. C,* 2014, 118, 13790–13800

[44] L. Ma, Z. Wu, G. Zhou, F. Yuan, Y. Yu, C. Yao, S. Ning, X. Hou, Y. Li, S. Wang and Q. Gong, *J. Mater. Chem. C,* 2015, 3, 7004–7013.

[45] J.-C. Ribierre, L. Zhao, M. Inoue, P. O. Schwartz, J.-H. Kim, K. Yoshida, A. S. D. Sandanayaka, H. Nakanotani, L. Mager, S. Méry and C. Adachi, *Chem. Commun.,* 2016, 52, 3103–3106.

[46] K. D. Belfield, M. V. Bondar, H. S. Haniff, I. A. Mikhailov, G. Luchita and O. V. Przhonska*, ChemPhysChem.,* 2013, 14, 3532–3542

[47] K. D. Belfield, M. V. Bondar, A. R.Morales, X. Yue, G. Luchita and O. V. Przhonska, *J. Phys. Chem. C*, 2012, 116, 11261–11271.

[48] H. D. Vishwasrao, P. Trifilieff and E. R. Kandel, *Biophys. J.,* 2012, 102, 1204–1214

[49] J. Borejdo, A. Shepard, I. Akopova, W. Grudzinski and J. Malicka, *Biophys. J.,* 2004, 87, 3912–3921

[50] J. Fu, O. V. Przhonska, L. A. Padilha, D. J. Hagan, E. W. Van Stryland, K, D. Belfield, M. V. Bondar, Y, L. Slominsky and A. D. Kachkovski *Chem. Phys.,* 2006, 321, 257–268

[51] K. D. Belfield, M. V. Bondar, J. M. Hales, A. R. Morales, O. V. Przhonska and K. J. Schafer, *J. Fluoresc.,* 2005, 15, 3–11

[52] R. S. Mulliken, *J. Am. Chem. Soc.,* 1952, 74, 801–822

[53] A. Painelli. *Chem. Phys. Lett.,* 1998, 285, 352–358

[54] A. Painelli. *Chem. Phys.,* 1999, 245, 185–197

[55] B. Boldrini, E. Cavalli, A. Painelli and F. Terenziani, *J. Phys. Chem. A,* 2002, 106, 6286–6294

[56] L. Grisanti, F. Terenziani, C. Sissa, M. Cavazzini, F. Rizzo, S. Orlandi and A. Painelli, *J. Phys. Chem. B,* 2011, 115, 11420–11430

[57] C. Sissa, A. Painelli, M. Blanchard-Desce and F. Terenziani, *J. Phys. Chem. B*, 2011, 115, 7009–7020

[58] S. Sanyal, A. Painelli, S. K. Pati, F. Terenziani and C. Sissa, *Phys. Chem. Chem. Phys.,* 2016, 18, 28198–28208

[59] J. R. Lakowicz, B. Kierdaszuk, P. Callis, H. Malak and I. Gryczynski *Biophys. Chem.,* 1995, 56, 263–271

[60] J. R. Lakowicz, I. Gryczynski, E. Danielsen and Joan Frisoli, *Chem. Phys. Lett.,* 1992, 194, 282–287

[61] P. R. Monson and W. M. McClain, *J. Chem. Phys.,* 1970, 53, 29–37

[62] P. R. Callis in *Topics in Fluorescence Spectroscopy. Volume 5: nonlinear and two-photon-induced fluorescence,* ed. J. R. Lakowicz, Kluwer Academic Publishers, 2002, pp 1–42

[63] P. R. Callis, *J. Chem. Phys.,* 1993, 99, 27-37

[64] P. R. Callis in *Topics in Fluorescence Spectroscopy. Volume 5: nonlinear and two-photon-induced fluorescence,* ed. J. R. Lakowicz, Kluwer Academic Publishers, 2002, pp. 1–42

[65] W. M. McClain, *J. Chem. Phys.,* 1972, 57, 2264–2272

[66] D.W. Piston and M. A. Rizzo, *Methods Cell Biol.,* 2008, 85, 415–430

[67] H. Kasai, H. S. Nalwa, H. Oikawa, S. Okada, H. Matsuda, N. Minami, A. Kakuta, K. Ono, A. Mukoh and H. Nakanishi, *Jpn. J. Appl. Phys.*, 1992, 31, L1132–L1134.

[68] J. B. Birks, *Photophysics of Aromatic Molecules,* Wiley, 1970

[69] Y, Hong, J. W. Y. Lamab and B. Z. Tang, *Chem. Soc. Rev.,* 2011, 40, 5361–5388

[70] K. Amro, J. Daniel, G. Clermont, T. Bsaibess, M. Pucheault, E. Genin, M. Vaultier and M. Blanchard-Desce, *Tetrahedron,* 2014, 70, 1903–1909

[71] V. Parthasarathy, S. Fery-Forgues, E. Campioli, G. Recher, F. Terenziani and M. Blanchard-Desce, *Small,* 2011, 7, 3219–3229

[72] C. Mastrodonato, P. Pagano, J. Daniel, M. Vaultier and M. Blanchard-Desce, *Molecules,* 2016, 21, 1227

[73] S. Soper, H. L. Nutter, R. A. Keller, L. M. Daviss and E. B. Shera *Photochem. Photobiol*, 1993, 51, 972–911

[74] N. Grimaldi, F. Andrade, N. Segovia, L. Ferrer-Tasies, S. Sala, J. Veciana and N. Ventosa, *Chem. Soc. Rev.,* 2016, 45, 6520–6545

[75] M. Cano-Sarabia, N. Ventosa, S. Sala, C. Patiño, R. Arranz and J. Veciana, *Langmuir*, 2008, 24, 2433–2437

[76] L. Ferrer-Tasies, E. Moreno-Calvo, M. Cano-Sarabia, M. Aguilella-Arzo, A. Angelova, S. Lesieur, S. Ricart, J. Faraudo, N. Ventosa and Jaume Veciana, *Langmuir*, 2013, 29, 6519–6528

[77] A. Ardizzone, S. Kurhuzenkau, S. Illa, J. Faraudo, M. Bondar, D. Hagan, E. W. Van Stryland, A. Painelli, C. Sissa, N. Feiner, L. Albertazzi, J. Veciana and N. Ventosa, *Adv. Mater., submitted*

[78] A. Song, J. Zhang, M. Zhang, T. Shen and J. Tang, *Colloids Surf. A: Physicochem. Eng. Asp.,* 2000, 167, 253–262

[79] S. Biswas, S. C. Bhattacharya, P. K. Sen and S. P. Moulik, *J. Photochem. Photobiol. A: Chem.,* 1999, 123, 121–128

[80] J. Hadjianestis and J. Nikokavouras, *J. Photochem. Photobiol. A: Chem.,* 1993, 69, 337–343

[81] Y.-C. Chen, K.-B. Han, H. Mizukami, A. Wojcik and A. Ostafin, *Nanotechnology,* 2010, 21, 455701

[82] M. N. Chretien, B. Shen, H. Garcia, A. M. English and J. C. Scaiano, *Photochem. Photobiol.,* 2004, 80, 434–437

[83] X. Wang, S. Yao, H-Y. Ahn, Y. Zhang, M. V. Bondar, J. A. Torres and K. D. Belfield, *Biomed. Opt. Express,* 2010, 1, 453–462

[84] L. Song, E. J. Hennink, T. Young and H. J. Tanke, *Biophys. J.,* 1995, 68, 2588–2600

[85] J. Mckenna, G. T. Prusky and I. Q. Whishaw, *J. Comp. Neur.,* 2000, 419, 286–296

[86] C. Gardiner and Rebecca Dragovic in *Extracellular vesicles in health and disease,* ed. P. Harrison, C. Gardiner, I. L. Sargent, CRC Press, 2014, 261–283

[87] J. Fu, L. A. Padilha, D. J. Hagan, E.W. Van Stryland, O.V. Przhonska, M. V. Bondar, Y. L. Slominsky and A. D. Kachkovski, *J. Opt. Soc. Am. B*, 2007, 24, 67–76

[88] L. A. Padilha, S. Webster, O. V. Przhonska, H. Hu, D. Peceli, T. R. Ensley, M. V. Bondar, A. O. Gerasov, Yu. P. Kovtun, M. P. Shandura, A. D. Kachkovski, D. J. Hagan and E. W. Van Stryland, *J. Phys. Chem. A,* 2010, 114, 6493–6501

[89] M. Levitus and S. Ranjit, *Q. Rev. Biophys.,* 2011, 44, 123–151.

[90] J. Kang, O. Kaczmarek, J. Liebscher and L. Dahne, *Int. J. Pol. Sci.,* 2010, 2010, 264781

[91] I. Texier, M. Goutayer, A. Da Silva, L. Guyon and N. Djaker, *J. Biomed. Opt.,* 2009, 14, 054005

[92] W. West and S. Pearce S, *J. Phys Chem*., 1965, 69, 1894–1903

[93] Y. Kawabe and S. Kato, *Dyes Pigm.,* 2012, 95, 614–618

[94] W. Yang, P. S. Chan, M. S. Chan, K. F. Li, P. K. Lo, N. K. Mak, K. W. Cheah and M. S. Wong, *Chem. Commun.,* 2013, 49, 3428–3430

[95] Y. Zheng, M. Zheng, S. Chen, Z. Zhao and X. Duan, *J. Mater. Chem. B,* 2014, 2, 2301–2310

[96] L. Guo and M. S. Wong, *Adv. Mater.,* 2014, 26, 5400–5428

[97] L. A. Padilha, S. Webster, O. V. Przhonska, H. Hu, D. Peceli, T. R. Ensley, M. V. Bondar, A. O. Gerasov, Yu. P. Kovtun, M. P. Shandura, A. D. Kachkovski, D. J. Hagan and E. W. Van Stryland, *J. Phys. Chem. A*, 2010, 114, 6493–6501

[98] R. S. Lepkowicz, O. V. Przhonska, J. M. Hales, J. Fu, D. J. Hagan, E. W. Van Stryland, M.V. Bondar, Yu. L. Slominsky and A. D. Kachkovski, *Chem. Phys.,* 2004, 305, 259–270

[99] F. Terenziani, O. V. Przhonska, S. Webster, L. A. Padilha, Y. L. Slominsky, I. G. Davydenko, A. O. Gerasov, Yu. P. Kovtun, M. P. Shandura, A. D. Kachkovski, D. J. Hagan, E. W. Van Stryland and A. Painelli, *J. Phys. Chem. Lett.,* 2010, 1, 1800–1804

[100] H. Hu, O.V. Przhonska, F. Terenziani, A. Painelli, D. Fishman, T. R. Ensley, M. Reichert, S. Webster, J. L. Bricks, A. D. Kachkovski, D. J. Hagan and E. W. Van Stryland, *Phys. Chem. Chem. Phys.,* 2013, 15, 7666–7678

[101] C. Sissa, P. M. Jahani, Z. G. Soos and A. Painelli, *ChemPhysChem.,* 2012, 13, 2795–2800

[102] H.-Y. Ahn, S. Yao, X. Wang and K. D. Belfield, *ACS Appl. Mater. Interfaces,* 2012, 4, 2847−2854

[103] G. W. Byers, S. Gross and P. M. Henrichs, *Photochem. Photobiol.,* 1976, 23, 37−43

[104] X. Chen, X. Peng, A. Cui, B. Wang, L. Wang and R. Zhang, *J. Photochem. Photobiol. A: Chem.,* 2006, 181, 79−85

[105] D. Wüstner, *Chem. Phys. Lipids,* 2007, 146, 1–25

[106] G. Gimpl and K. Gehrig-Burger, *Biosci. Rep.,* 2007, 27, 335–358

[107] K. A. Solanko, M. Modzel, L. M. Solanko and Daniel Wüstner, *Lipid Insights*, 2015, 8, 95–114

[108] M. Amaro, H. A. L. Filipe, J. P. P. Ramalho, M. Hof and L. M. S. Loura, *Phys. Chem. Chem. Phys.,* 2016, 18, 7042-7054

[109] S. Mukherjee and A. Chattopadhyay, *Biochem*., 1996, 35, 1311–1322

[110] R. Rukmini, S. S. Rawat, S. C. Biswas and A. Chattopadhyay, *Biophys. J.,* 2001, 81, 2122–2134

[111] S. Haldar and A. Chattopadhyay in *Fluorescent Methods to Study Biological Membranes,* ed. Y. Mély and G. Duportail, Springer, 2012, pp. 37–50

[112] T. J. Pucadyil, S. Mukherjee and A. Chattopadhyay, *J. Phys. Chem. B,* 2007, 111, 1975–1983

[113] S. Lin and W. S. Struve, *Photochem. Photobiol.,* 1991, 54, 361–365

[114] L. M. S. Loura and M. Prieto, *Biophys. J.,* 1997, 72, 2226–2236

[115] D. Hoekstra, *Biochem.,* 1982, 21, 1055–1061

[116] S. Fery-Forgues, J.-P. Fayet and A. Lopez, *J. Photochem. Photobiol. A Chem.,* 1993, 70, 229–243.

[117] B. W. van der Meer in *FRET –Förster resonance energy transfer from theory to applications*, ed. I. Medintz and N. Hildebrandt, Wiley, 2014, pp. 23–62

[118] L. Stryer and R. P. Haugland, *Proc. Natl. Acad. Sci. USA*, 1967, 58, 719–726

[119] B. Tang, L. Cao, K. Xu, L. Zhuo, J. Ge, Q. Li and L. Yu, *Chem. Eur. J.,* 2008, 14, 3637–3644

[120] A. E. Albers, V. S. Okreglak and C. J. Chang, *J. Am. Chem. Soc.,* 2006, 128, 9640–9641

[121] Y. Chen, J. D. Mills and A. Periasamy, *Differentiation*, 2003, 71, 528–541

[122] X. He, Y. Wang, K. Wang, M.Chen and S. Chen, *Anal. Chem.,* 2012, 84, 9056–9064

[123] J. Chen, A. Tsai, A. Petrov and J. D. Puglisi, *J. Am. Chem. Soc.,* 2012, 134, 5734–5737

[124] R. S. Knox, *J. Biomed. Opt.,* 2012, 17, 011003

[125] A. Wagh, S. Y. Qian and B. Law, *Bioconjugate Chem.,* 2012, 23, 981–992

[126] T.O. McDonald, P. Martin, J. P. Patterson, D. Smith, M. Giardiello, M. Marcello, V. See, R. K. O'Reilly, A. Owen and S. Rannard, *Adv. Funct. Mater.,* 2012, 22, 2469–2478.

[127] S. Yao, H.-Y. Ahn, X. Wang, J. Fu, E. W. Van Stryland, D. J. Hagan and K. D. Belfield, *J. Org. Chem.* 2010, 75, 3965–3974

[128] C. D. Andrade, C. O. Yanez, M. A. Qaddoura, X. Wang, C. L. Arnett, S. A. Coombs, J. Yu, R. Bassiouni, M. V. Bondar and K. D. Belfield, *J. Fluoresc.,* 2011, 21, 1223–1230

[129] K. J. Schafer-Hales, K. D. Belfield, S. Yao, P. K. Frederiksen, J. M. Hales and P. E. Kolattukudy, *J. Biomed. Opt.,* 2005, 10, 051402

[130] S. Yao and K. D. Belfield, *Eur. J. Org. Chem.,* 2012, 2012, 3199–3217

[131] M. J. Ruedas-Rama, J. D. Walters, A. Orte, E. A. H. Hall, *Anal. Chim. Acta,* 2012, 751, 1–23

[132] X. Wang, D. M. Nguyen, C. O. Yanez, L. Rodriguez, H.-Y. Ahn, M. V. Bondar and K. D. Belfield, *J. Am. Chem. Soc.,* 2010, 132, 12237–12239

[133] E. Abbe, *Archiv. f. mikrosk. Anatomie,* 1873, 9, 413–468

[134] E. F. Fornasiero and F. Opazo in *Fluorescence microscopy super-resolution and other novel techniques,* ed. A. Cornea, P. M. Conn, Elsiever, 2014, pp. 133–152

[135] M. J Rust, M. Bates and X. Zhuang, *Nat. Metho*ds*,* 2006, 3, 793–796

[136] M. Bates, T. R. Blosser and X. Zhuang*, Phys. Rev. Lett.,* 2005, 94, 108101

[137] T. Ha and P. Tinnefeld, *Annu. Rev. Phys. Chem.*, 2012. 63, 595–617

[138] J. Hohlbein, K. Gryte, M. Heilemann and A. N. Kapanidis, *Phys. Biol.,* 2010, 7, 031001

[139] G.Yang, L. Liu, Q. Yang, F. Lv and S. Wang, *Adv. Funct. Mater.,* 2012, 22, 736–743

[140] B. Huang, S. A Jones, B. Brandenburg and X. Zhuang, *Nat. Methods,* 2008, 5, 1047–1052

[141] S. Yao and K. D. Belfield. *J. Org. Chem.,* 2005, 70, 5126–5132

LIST OF PUBLICATIONS AND PATENTS

1 S. A. Kurhuzenkau, A. W. Woodward, S. Yao, K. D. Belfield, Y. O. Shaydyuk, C. Sissa, M. V. Bondar and A. Painelli *Phys.Chem.Chem.Phys*., 2016, 18, 12839

2 A. Ardizzone, S. Kurhuzenkau, S. Illa, J. Faraudo, M. Bondar, D. Hagan, E. W. Van Stryland, A. Painelli, C. Sissa, N. Feiner, L. Albertazzi, J. Veciana and N. Ventosa *Adv.Mater. submitted*

3 European patent application №EP16382392.5 "Use of Stable and versatile vesicles for imaging applications". N. Ventosa, J. Veciana, A. Ardizzone, S. Sala, A. Painelli, C. Sissa, S. Kurhuzenkau

4 S. A. Kurhuzenkau, S. Yao, K. D. Belfield, E. W. Van Stryland, D. J. Hagan, C. Sissa, M. V. Bondar and A. Painelli. "Two-photon absorption and stimulated emission depletion in a symmetric fluorene derivative". *In preparation*